Alma Mater Studiorum · University of Bologna

School of Science
Department of Physics and Astronomy
Master Degree in Physics

Experimental protocol for the determination of elastic properties at ambient and high pressure by picosecond acoustics technique

Supervisor:
Prof. Federico Boscherini

Co-supervisor:
Dr. Daniele Antonangeli

Submitted by:
Sofia Balugani

Academic Year 2020/2021

Ringraziamenti

Vorrei ringraziare le persone che mi hanno supportato nei modi più disparati durante questi anni di Università.

Grazie a Daniele, il mio supervisor a Parigi, che mi ha ospitato nel suo gruppo di ricerca, MP3, dandomi l'opportunità di scoprire l'affascinante acustica picosecondo . Grazie anche per il tempo dedicato, soprattutto per l'attenzione data ad ogni singolo dettaglio della stesura della tesi. Ho imparato molte cose preziose che mi serviranno lungo il mio cammino di vita.

Grazie anche a Frédéric e a Michel per aver condiviso con me la loro esperienza e le loro conoscenze.

Un grazie speciale va a Silvia e Nicki, due persone molto speciali che mi hanno seguita ed aiutata durante i mesi di internship. Difficile descrivere quanto io vi sia grata per l'aiuto a 360 gradi che mi avete offerto spontaneamente: da consigli di vita e insegnamenti scientifici al buonumore che mi avete trasmesso ogni giorno. Grazie per il cioccolato mangiato insieme quando pensavo di aver rotto i diamanti (non lo erano alla fine) e tutte le altre volte in cui ce n'è stato bisogno. Grazie a Nicki per il "righty tighty, lefty loosy", ora so come ricordarmi in quale senso vanno girati i rubinetti. Grazie a Silvia per aver insistito testardamente (tu sai a cosa mi riferisco).

Un ringraziamento va al mio relatore di Bologna, Prof. Federico Boscherini, per la disponibilità, il supporto e l'interessamento che mi ha sempre mostrato.

Grazie a tutte le persone che ho incontrato a Parigi. Nonostante il periodo difficile dato dal covid, la mia esperienza è stata speciale grazie a voi. Grazie ad Anwita per le sedute di yoga e per tutto il resto e grazie a Dylan per avermi fatto scoprire il Lou Perac (che però in Italia non si trova), ma non solo.

Grazie a tutti i miei amici per esserci sempre stati. In particolare, grazie ad Anna, Bongi, Sindi e Panni per il vostro entusiasmo, per le chiamate e per farmi sempre sorridere, insomma grazie per essere quello che siete. Senza di voi, sarebbe stato tutto molto più difficile.

Un ringraziamento speciale va ai miei genitori, Massimo e Ludovica. Elencare tutti i modi in cui mi hanno avete aiutato prenderebbe tutta la pagina di questi ringraziamenti, e quindi un semplice grazie, non solo per il contributo che avete dato a questa tesi, ma per tutti questi anni, ascoltandomi ripetere esami e presentazioni nonostante non fosse il vostro campo. Grazie per aver creduto in me ogni singolo istante soprattutto quando io non riuscivo a farlo.

Infine, vorrei ringraziare Chicco. Presente al 100% nella mia vita, che ha condiviso con me questo percorso universitario e di vita dall'inizio alla fine e che non si è mai fatto scoraggiare (e anche tu sai di cosa parlo). Grazie per aver ripetuto insieme prima degli esami, collega. Grazie per avermi fatta sfogare e per avermi consigliato, amico. Grazie per avermi trasmesso affetto e comprensione, compagno.

Contents

Introduction

Several physical properties of condensed matter related to lattice dynamics and collective motions - such as the sound velocity, the elastic constants and the interatomic force constants - are investigated through the study of the elastic waves propagating in a medium. Furthermore, examining the effects of pressure on the propagation of acoustic waves in a material allows to characterize its elasticity, mechanical stability, strength, and to better understand phase transition mechanisms. Elasticity under extreme conditions of pressure and temperature also has a crucial importance in constraining models of the Earth and planetary interiors. In fact, one of the main obstacles in determining the planets' chemical composition is constituted by the limitation in direct sampling and by the lack of direct investigation methods [1]. Seismology, which studies the travel times of elastic waves generated by earthquake and by the planet free oscillations, arguably is the most reliable probe allowing to constrain the properties of planetary interiors. Even when limiting to radially averaged models, seismic observations provide one-dimensional profile of the compressional velocity, V_P, shear velocity, V_S, and density with depth across the entire Earth [2]. Great efforts were invested by the Apollo program to deploy a seismic array on the Moon [3] and first seismological observations are now available for Mars as well [4]; [5]. However, seismological models alone do not allow to relates geophysical observations to compositional and structural models and require deciphering [6]. The determination of the elastic properties of the candidate materials comprising planetary interiors via experimental measurements is thus of fundamental importance, because such measurements provide the guidance to interpret coherently the seismological observations and the link to derive consistent model of the composition and structure of planets [6], [7]. Compressional (or longitudinal) and shear (or transverse) waves' velocities directly depend on the elastic properties, i.e. on the bulk and shear moduli, of the medium in which they propagate. So, observed depth dependence and discontinuities in the propagation of the sound velocity across a planet directly reflect pressure and temperature effects, or phase transitions, in the constituent materials. Despite the fact that reference seismic model for the Earth is available since mid '80s [2], elastic properties of geo-materials at relevant pressure and temperature conditions are not fully established yet. This is a direct consequence of fact that all the experimental methods used to investigate elasticity under extreme conditions suffer of limitations, be these the highest attainable pressure, the nature of the investigated materials, or the limited instrumental access.

Thus, this work consists in establishing an experimental protocol for the determination of single crystals' elastic constants, C_{ij}, of materials at ambient pressure and high pressure by picosecond acoustics. Picosecond acoustics is an experimental pump-probe technique that allows to directly probe the acoustic waves propagating within a sample. The concept is similar to the pulse-echo ultrasonic technique (travel time determination) with the advantage of optical methods (no contact and no bonding effects). Furthermore, thanks to the possibility of combining the diamond anvil cell (DAC) technology to picosecond acoustics, sound velocity and elastic properties can be obtained at the high-pressure conditions relevant for planetary interiors. Finally, picosecond acoustics is

a promising experimental method because it has no specific limitations on the nature of the materials that can be investigated and it is a laboratory-based and non-destructive experimental technique.
As test cases, two materials were studied in this work: magnesium oxide, MgO, and ruthenium, Ru. Both were studied at ambient temperature and pressure. Ru was also studied up to 10 GPa. MgO, an optical transparent insulator, is investigated because it is an end-member mineral composing planetary mantles and forms a solid solution with FeO; single crystal of high quality are commercially available and can serve as a test case to determine an experimental protocol that allows the investigation of transparent samples. Ru, an opaque metal, is studied because of its analogy with Iron: they are isoelectronic, but the advantage on studying Ru is that at ambient conditions shows hexagonal symmetry while Fe shows bcc phase, making difficult to perform studies on the hcp single crystal of Iron, phase that is stable only at high-pressure.
Beside this introduction, this thesis is divided into three chapters followed by short conclusions. Chapter 1 consists of a brief treatment of the fundamental principles of elasticity, the Christoffel equation, the elastic properties of single crystals and aggregates, and a short description of the Birch-Murnaghan's equation of state. An overview of the existing techniques employed to probe elastic properties is then provided, with specific emphasis on the limitations driving the choice of developing picosecond acoustics. Chapter 2 presents the experimental, analytical and computational methods used in this work. In particular, picosecond acoustics and diamond anvil cells are described in some detail. The section dedicated to computational methods describes the programs that allow to extract information on the sound velocities and on the elastic constants of the sample from the acoustic waves measurements. In Chapter 3 all the results obtained are presented and discussed.

Chapter 1

Elasticity at high pressure

This chapter presents three topics: the first part (from section 1.1 to section 1.3) concerns theoretical background necessary to understand the basic physical principles underlying the experiments; the second part (section 1.4) is dedicated to a brief review of the existing experimental techniques, highlighting their current limitations, and presenting how picosecond acoustics can be used to overcome such limitations; the third part (section 1.5) summarizes the properties of the materials investigated in this thesis work, including some hints about their symmetry group, their elastic tensors and the main reasons motivating their study.

1.1 Acoustic phonons

Phonons are the quanta describing the lattice vibrations inside a material. Acoustic phonons correspond to in phase collective vibrations, whose frequencies vanish for small k with a slope proportional to sound velocity. The goal pursued in this thesis work consists in the study of material's elastic properties, which depends on acoustic phonons. In appendix A, mathematical derivation of phonon frequencies for the simple case of linear chains are presented.

1.2 Fundamental concepts of elasticity

The mathematical treatment presented in [8] will be here summarized to present the fundamental concepts of elasticity.
Theory of elasticity relates the stress tensor, σ_{ij}, which expresses the internal forces that neighbouring particles of a continuous material exert on each other, and the strain tensor, ϵ_{kl}, which is the deformation in terms of relative displacement of particles in the body. A solid is defined as "elastic solid" when the initial state is recovered once the all mechanical forces that were acting on it are switched off. For the majority of materials it has been demonstrated that the elastic behavior is well approximated under the hypothesis of small deformation developed up to the second order of Taylor expansion:

$$\sigma_{ij}(\epsilon_{kl}) = \sigma_{ij}(0) + \left(\frac{\partial \sigma_{ij}}{\partial \epsilon_{kl}}\right)_{\epsilon_{kl}=0} \epsilon_{kl} + \frac{1}{2}\left(\frac{\partial^2 \sigma_{ij}}{\partial \epsilon_{kl}\partial \epsilon_{mn}}\right)_{\epsilon_{kl},\epsilon_{mn}=0} \epsilon_{kl}\epsilon_{mn} \tag{1.1}$$

In most cases, experimental results are well described by truncation at first-order term of the Taylor expansion.
Assuming that $\sigma_{ij}(0)$=0, Equation 1.1 becomes the generalized Hooke's law, that defines for an elastic solid a linear relation between stresses σ_{ij} and strains ϵ_{kl}:

$$\sigma_{ij} = C_{ijkl}\epsilon_{kl} \tag{1.2}$$

where:

$$C_{ijkl} = \left(\frac{\partial \sigma_{ij}}{\partial \epsilon_{kl}}\right)_{\epsilon_{kl}=0} \tag{1.3}$$

C_{ijkl} is a tensor of rank 4 with 3^4= 81 components and is called stiffness tensor (or elastic tensor). Equation 1.2 corresponds to the most general linear relation between stress and strain, first formulated in one-dimensional case by Hooke. Since tensors σ_{ij} and ϵ_{kl} are symmetric (see [8]), the elastic components defined by the stiffness tensor are unchanged when either the first two or the last two indices are interchanged, so that:

$$C_{ijkl} = C_{jikl} \quad \text{and} \quad C_{ijkl} = C_{ijlk} \tag{1.4}$$

In terms of displacement, $\vec{u}$, Hooke's law (eq. 1.2) becomes:

$$\sigma_{ij} = \frac{1}{2} C_{ijkl} \frac{\partial u_k}{\partial x_l} + \frac{1}{2} C_{ijkl} \frac{\partial u_l}{\partial x_k} \tag{1.5}$$

and by considering the symmetry of stiffness tensor given by Equation 1.4, it becomes:

$$\sigma_{ij} = C_{ijkl} \frac{\partial u_l}{\partial x_k} \tag{1.6}$$

The symmetry relation expressed by Equation 1.4 allows to reduce the number of independent elastic constants from 81 to 36. Indeed, a pair of unordered indices (i, j) can give only six independent variables. By performing the indices' reduction presented below:

$$\begin{array}{ccc} (11) \leftrightarrow 1 & (22) \leftrightarrow 2 & (33) \leftrightarrow 3 \\ (23) = (32) \leftrightarrow 4 & (31) = (13) \leftrightarrow 5 & (12) = (21) \leftrightarrow 6 \end{array} \tag{1.7}$$

It is possible to rewrite the elastic tensor C_{ijkl} as a 6 x 6 matrix. Thanks to this, the independent elastic constants (also called elastic moduli) can be written with just two indices (α, β), where α is related to (i,j) and β to (k, l).

$$C_{\alpha\beta} = \begin{pmatrix} C_{11} & C_{12} & C_{13} & C_{14} & C_{15} & C_{16} \\ C_{21} & C_{22} & C_{23} & C_{24} & C_{25} & C_{26} \\ C_{31} & C_{32} & C_{33} & C_{34} & C_{35} & C_{36} \\ C_{41} & C_{42} & C_{43} & C_{44} & C_{45} & C_{46} \\ C_{51} & C_{52} & C_{53} & C_{54} & C_{55} & C_{56} \\ C_{61} & C_{62} & C_{63} & C_{64} & C_{65} & C_{66} \end{pmatrix} \tag{1.8}$$

Another tensor, the compliance tensor S_{ijkl} can be defined since it is related to stiffness tensor through:

$$S_{\alpha\beta} = (C_{\alpha\beta})^{-1} \tag{1.9}$$

In the generalized case, Hooke's law can be written equivalently in terms of stiffness tensor $C_{\alpha\beta}$ and in terms of compliance tensor $S_{\alpha\beta}$ as follows :

$$\begin{array}{c} \sigma_\alpha = C_{\alpha\beta}\varepsilon_\beta \\ \varepsilon_\alpha = S_{\alpha\beta}\sigma_\beta \end{array} \tag{1.10}$$

During this work, we studied two materials, magnesium oxide, MgO, and ruthenium, Ru, which respectively have cubic and hexagonal crystal symmetry. Below the elastic tensors in the case of cubic and hexagonal symmetries are reported. It can be proven that elastic tensor in the case of cubic crystal symmetry is written as follows:

$$C_{\alpha\beta} = \begin{pmatrix} C_{11} & C_{12} & C_{12} & 0 & 0 & 0 \\ C_{12} & C_{11} & C_{12} & 0 & 0 & 0 \\ C_{12} & C_{12} & C_{11} & 0 & 0 & 0 \\ 0 & 0 & 0 & C_{44} & 0 & 0 \\ 0 & 0 & 0 & 0 & C_{44} & 0 \\ 0 & 0 & 0 & 0 & 0 & C_{44} \end{pmatrix} \tag{1.11}$$

with three independent elements: C_{11}, C_{12} and C_{44}. More details about cubic symmetric single crystals are reported in [9].
While, the elastic tensor in the case of hexagonal crystal symmetry is simplified as follows:

$$C_{\alpha\beta} = \begin{pmatrix} C_{11} & C_{12} & C_{13} & 0 & 0 & 0 \\ C_{12} & C_{11} & C_{13} & 0 & 0 & 0 \\ C_{13} & C_{13} & C_{33} & 0 & 0 & 0 \\ 0 & 0 & 0 & C_{44} & 0 & 0 \\ 0 & 0 & 0 & 0 & C_{44} & 0 \\ 0 & 0 & 0 & 0 & 0 & C_{66} \end{pmatrix} \tag{1.12}$$

in which C_{66} is equal to $\frac{C_{11}-C_{12}}{2}$. So the independent elements are five: C_{11}, C_{12}, C_{13}, C_{33} and $C44$.

1.3 Single crystal elastic moduli and aggregate elastic properties

When action and/or reaction are tensorial quantities and are linearly related, such as stress and strain (see section 1.2), the material property that links the exerted action with the associated reaction also has a tensorial character. The physical evidence of anisotropy is the difference in the reaction to the same action when the latter is exerted along a different direction in the material. In practice, elastic properties of single crystals are always anisotropic, although, more or less, depending on crystal symmetry.
For all symmetries, except for monoclinic and triclinic, we can assume that:

$$\delta V/V \approx \epsilon_1 + \epsilon_2 + \epsilon_3 \tag{1.13}$$

where ϵ_i are the diagonal components of strain tensor. Eq. 1.13 implies that the volume variation (indicated through the ratio $\delta V/V$) as a consequence of high pressure can be written as the sum of the strains in the three independent crystallographic directions. The bulk modulus, K, is defined as:

$$K = -V\delta P/\delta V = -\delta P/(\epsilon_1 + \epsilon_2 + \epsilon_3) = (S_{11} + S_{22} + S_{33} + S_{12} + S_{13} + S_{23})^{-1} \tag{1.14}$$

where P is the pressure.
For a macroscopic non-single crystal sample, the aggregate properties are the volume average of the constituents single-crystalline grains properties. Aggregates of non-interacting grains can exhibit or not anisotropy, depending on the random or not random distribution of orientation (texture).

1.3.1 Christoffel equation

Christoffel equation sets the formal basis on which many results of elasticity are interpreted and analyzed. In fact, it provides the link between sound velocities and elastic constants. Christoffel equation takes the form of an eigenvalue problem:

$$\left|\Gamma_{il} - \rho V^2 \delta_{il}\right| = 0 \tag{1.15}$$

where Γ_{il} is the Christoffel tensor, ρ the density and V indicates the phase velocity.
The mathematical derivation is reported in appendix B.
In general, for a given direction of propagation $\vec{n}$, phase velocities are roots of the secular problem set by the Christoffel equation. To each velocity corresponds an eigenvector

which defines the direction of matter displacement. Descending from symmetry of stiffness tensor, Christoffel tensor is symmetric too. This means that its eigenvalues are real and its eigenvectors are orthogonal. Furthermore, it is possible to demonstrate that the eigenvalues are positive [8]. Finally, it can be derived a general result which concludes that three plane waves with orthogonal polarizations can propagate in the same direction with different velocities. The displacement vector $\vec{u}$ is not in general parallel or perpendicular to the direction of propagation $\vec{n}$. The wave with polarization closest to $\vec{n}$ is called quasi-longitudinal wave, while the waves with polarization closest to be $\perp$ to $\vec{n}$ are called quasi-transverse. Thus, all solid bodies are characterized by the possibility to carry three waves that propagate at different velocities: longitudinal waves and two different transverse waves.
As described later in Chapter 2, in picosecond acoustics experiment, the pump laser can be focused on a spot of dimension variable with respect to sample's dimensions. For highly focused configurations, elastic waves can be considered as generated from a point source, while in case of defocused beam from an extended source. In the fist case the resulting wave can be considered spherical, while in the second the wave front resulting from the diffracting spherical waves approaches a plane wave.
As said before, Christoffel equation is a powerful tool to determine elastic constants from phase sound velocity and viceversa. On the other hand, picosecond acoustics detects the intensity change (the change in reflectivity), which is an energy per area, and thus carries information on energy sound velocity, $\vec{V^e}$, and not directly on the phase sound velocity $\vec{V}$. In the following lines, the relation between the two will be briefly described.
The energy sound velocity $\vec{V^e}$ is by definition equal to Poynting vector divided by the energy per unit volume, so that:

$$V_i^{\mathrm{e}} = \frac{C_{ijkl} u_j^{\mathsf{T}} u_l^{\mathsf{T}} n_k}{\rho V} \quad \text{for} \quad u_i^{\mathsf{T}2} = 1 \tag{1.16}$$

Let us consider the scalar product:

$$\vec{V}^{\mathrm{e}} \cdot \vec{n} = V_i^{\mathrm{e}} n_i = \frac{C_{ijkl} u_j^{\mathsf{T}} u^{\mathsf{T}} u_l n_i n_k}{\rho u_i^{\mathsf{T}2} V} \tag{1.17}$$

it can be proven that:

$$\vec{V}^{\mathrm{e}} \cdot \vec{n} = V \tag{1.18}$$

which means that the projection of energy velocity on the direction of propagation gives the phase velocity. Energy velocity, expressed in Equation 1.16, tells which is the direction of energy transport, i.e. the direction of acoustic ray. When this ray is perpendicular to wave fronts, so parallel to $\vec{n}$, wave mode is called "pure" (where polarization is either longitudinal or transverse). In general, energy flux and group velocity directions are perpendicular to wave fronts in the case of isotropic media while in the case of anisotropic media they are perpendicular only for certain crystallographic directions.
In appendix B, derivation of Christoffel tensor for a given symmetry group and a given direction of propagation in derived. Choosing the direction for which Christoffel tensor is in its simplest form for a given symmetry, can give a great advantage in the calculations. In general, depending on the symmetry group, to get the full elastic tensor C_{ijkl}, more than one direction of propagation is needed.
In Table 1.1 formulas to get velocity through elastic moduli for cubic symmetric crystals and selected propagation directions are listed.

Propagation direction	Polarization	Velocity
[001]	[001] (L)	$\sqrt{\frac{C_{11}}{\rho}}$
[100]	plane (100) (T)	$\sqrt{\frac{C_{44}}{\rho}}$
[110]	[110] (L)	$\sqrt{\frac{C_{11}+C_{12}+2C_{44}}{\rho}}$
[110]	$[1\bar{1}0]$ (T)	$\sqrt{\frac{C_{11}-C_{12}}{2\rho}}$
[110]	[001] (T)	$\sqrt{\frac{C_{44}}{\rho}}$

Table 1.1: Velocity dependence of the three waves (one longitudinal and the two transverses) to elastic moduli in the case of cubic symmetry for selected direction of propagation [8].

In Table 1.2 velocities dependence on elastic moduli in the case of hexagonal crystal sample are listed:

Propagation direction	Polarization	Velocity
[001]	[001] (L)	$\sqrt{\frac{C_{33}}{\rho}}$
[001]	plane (001) (T)	$\sqrt{\frac{C_{44}}{\rho}}$
plane (001)	[001] (L)	$\sqrt{\frac{C_{11}}{\rho}}$
plane (001)	plane (001) (T)	$\sqrt{\frac{C_{11}-C_{12}}{2\rho}}$
plane (001)	[001] (T)	$\sqrt{\frac{C_{44}}{\rho}}$

Table 1.2: Velocity dependence of the three waves (one longitudinal and the two transverses) to elastic moduli in the case of hexagonal symmetry for selected direction of propagation [8].

1.3.2 Aggregate elastic moduli

Most Earth's materials present heterogeneous character, often at different scales. Rocks are aggregates of several different anisotropic minerals that frequently have widely varying properties [10]. Samples of the same rock may exhibit different elastic behavior and represent heterogeneity on a scale larger than the grain size. For this reason, study the mechanical properties of aggregates is primarily important in geophysics.
Voigt and Reuss were the first to work on elastic properties of polycrystals and together with Hill, they elaborated what is called the Voigt-Reuss-Hill average rule, which still today is largely used to determine the elastic moduli of aggregates starting from single crystalline properties [10]. In the most general case, in order to determine the properties of the aggregate is not sufficient to make a simple directional average, since grain interactions have to be taken into account. Also, aggregates of non interacting crystalline grains can exhibit anisotropy arising from the non random distribution of orientations [11]. In this context, Voigt average and Reuss average can be both used to derive the bulk modulus, K, and the shear modulus, G, of aggregates. Voigt average assumes uniform strain accross grains and constitutes the lowest upper bound to the aggregate properties. Reuss average assumes uniform stress across grains and constitutes the highest lower bound. The mean value of the two is the widely used Voigt-Reuss-Hill average[11].
Voigt averages states that:

$$\begin{aligned} K_V &= \frac{1}{9}\left(C_{11}+C_{22}+C_{33}\right)+\frac{2}{9}\left(C_{23}+C_{13}+C_{12}\right) \\ G_V &= \frac{1}{15}\left(C_{11}+C_{22}+C_{33}\right)-\frac{1}{15}\left(C_{23}+C_{13}+C_{12}\right)+\frac{1}{5}\left(C_{44}+C_{55}+C_{66}\right) \end{aligned} \tag{1.19}$$

While within the Reuss average:

$$\begin{aligned}\frac{1}{K_R} &= (S_{11}+S_{22}+S_{33})+2\,(S_{23}+S_{13}+S_{12})\\ \frac{1}{G_R} &= \frac{4}{15}\,(S_{11}+S_{22}+S_{33})-\frac{4}{15}\,(S_{23}+S_{13}+S_{12})+\frac{3}{15}\,(S_{44}+S_{55}+S_{66})\end{aligned} \tag{1.20}$$

Where $C_{\alpha\beta}$ are the components of stiffness tensor and $S_{\alpha\beta}$ terms are the ones of compliance tensor. Needless to say, increasing the symmetry of the crystalline structure, expression of K and G greatly simplifies.
Once the density, ρ, is known, aggregate compressional velocity, V_P, and shear velocity, V_S, can be derived from the bulk and shear moduli, as follows:

$$\begin{aligned}V_P^2 &= \frac{1}{\rho}\left(K+\frac{4}{3}G\right)\\ V_S^2 &= \frac{G}{\rho}\end{aligned} \tag{1.21}$$

1.3.3 Birch-Murnaghan equation of state

Equations of state provide the link between volume V and thermodynamic variables such as pressure P and temperature T. These are fundamental for acquiring thermodynamic data that, in turn, are required, for example, for the calculation of equilibrium phase diagrams. Equations of state provide insights into the interatomic interactions within the material.
One of the most largely used finite-strain equation of state to describe the P-V compressional curve of solid materials is the Birch-Murnaghan equation of state. Birch-Murnaghan equation of state approximated at the third-order is reported below:

$$P(V)=\frac{3K_0}{2}\left[\left(\frac{V_0}{V}\right)^{\frac{7}{3}}-\left(\frac{V_0}{V}\right)^{\frac{5}{3}}\right]\left\{1+\frac{3}{4}\,(K_0'-4)\left[\left(\frac{V_0}{V}\right)^{\frac{2}{3}}-1\right]\right\} \tag{1.22}$$

where P is the pressure, V the volume at a given pressure P, K_0 is the isothermal bulk modulus at ambient conditions and the K_0' is the first-order pressure derivative of bulk modulus at ambient conditions. Noteworthy the isothermal bulk modulus entering into the equation is thermodyanmically defined as $K=-V\left(\frac{\partial P}{\partial V}\right)_T$, which is different from the adiabatic bulk modulus calculated from elastic constants C_{ijkl}, see previous section. Isothermal bulk modulus K_T and adiabatic bulk modulus K_S are related by the thermal expansion α and the Grüneisen parameter γ:

$$K_S=(1+\alpha\gamma T)K_T$$

1.4 Experimental techniques

In this section some of the major experimental techniques that are more commonly used for the investigation of the materials' elastic constants are briefly presented, paying attention to the aspects which limit their applications for studies under extreme thermodynamic conditions. Development of picosecond acoustics offers the promise to overcome many of these limitations.

1.4.1 Ultrasonic interferometry

Ultrasonic interferometry is the most commonly used experimental technique for the study of materials' elastic constants. The general working principle implies the use of

both megahertz tone burst, transmitted via a piezoelectric transducer, and a delay line (buffer rod), (see Figure 1.1). The propagating waves are partially reflected at each interface. Each echo (i.e. acoustic waves reflected n times by sample's interfaces) is recorded by the transducer with a time delay, t, due to the waves travelling roundtrip inside the sample, and with a phase shift caused by bonding material between buffer rod and the sample (θ). When the phase shift between roundtrip travel and the bond is an integer multiple n of π, the buffer rod echo and sample echo will appear to be in phase (when n is even) or out of phase (when n is odd). In this way is possible to derive the travel time [12].
Known the travel time, Δt, and the sample thickness is possible to derive the sound velocity. Since transducers works at MHz frequencies, required sample dimensions have to be of the order of mm, fact that represents a big disadvantage for application at high pressure. In particular, diamond anvil cells (see section 2.2) cannot be used to reach very high pressure, since these high-pressure devices require sample's dimensions of the order of hundreds of μm at maximum. As such ultrasonic interferometry measurements are typically performed in large volume presses, leading to max pressures of the order of 30 GPa [12].

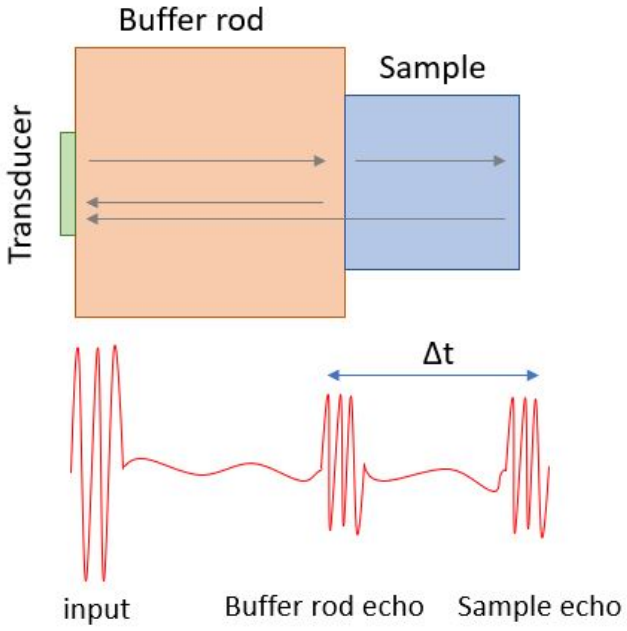

Figure 1.1: Schematic diagram for ultrasonic interferometric measurements.

1.4.2 Brillouin spectroscopy

Brillouin spectroscopy is an optical technique that allows determining acoustic velocities and their directional dependence in materials subject to a wide range of environmental conditions, including measurements in diamond anvil cells, see Figure 1.2. The light is scattered by thermally excited acoustic waves in an homogeneous medium. More precisely, Brillouin scattering consists in the inelastic scattering of photons by spontaneous thermal fluctuations/excitations in a material. Phonons contribute to fluctuations of the dielectric tensor of the material that are responsible for the scattering of light in directions different from that of the incident light propagation[13]. Although Brillouin spectroscopy is one of the most established technique for determination of elastic tensor and sound velocities, it can be used for only optically transparent materials. This aspect constitutes a great limitation on the study of Earth's deep interior, being opaque both

the Fe-bearing major minerals comprising the mantle, both the metallic Fe-alloy forming the core.

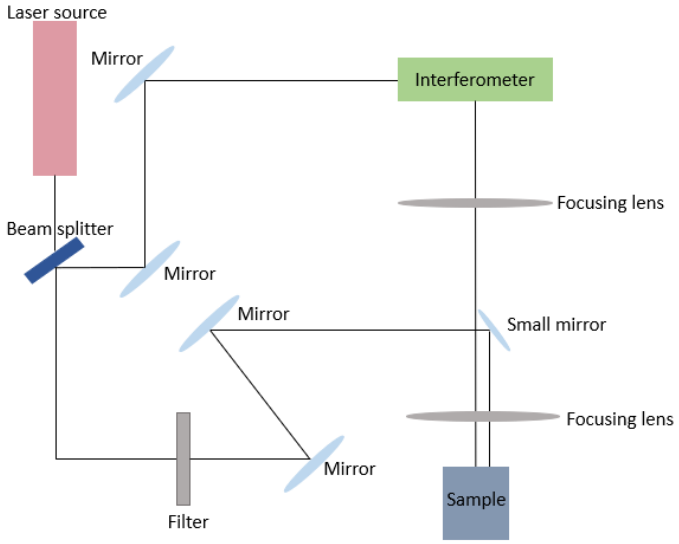

Figure 1.2: Schematic representation of a Brillouin spectrometer.

1.4.3 Other experimental techniques based on scattering process

All the experimental techniques based on scattering of incident particle by matter can be described by the same scheme presented in Figure 1.3. An incident beam with energy E_i and momentum $\boldsymbol{k_i}$, whether composed by photons, neutrons or electrons, is scattered by the lattice phonons of the crystal. After the scattering process, the emitted particle will emerge with different energy, E_f and momentum $\boldsymbol{k_i}$. The scattering angle 2θ and energy difference $E_f - E_i$ carry information on the inelastic process within the sample.

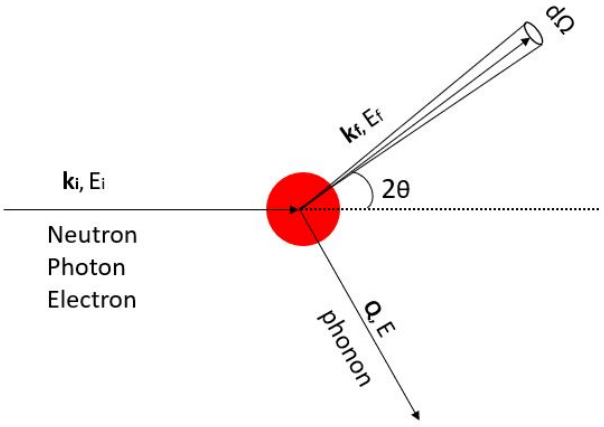

Figure 1.3: Schematic of a scattering process: an incoming particle is scattered (by a phonon). The emitted particle carries the information about the energy exchanged during the scattering process.

Inelastic neutron scattering (INS)

Inelastic neutron scattering is an experimental technique which exploits neutron beams as incident beam for the scattering process. One can view the energy lost (or gained) by a neutron while interacting with a crystal as being due to the emission (or absorption)

of phonons, and by measuring the emergent angles, 2θ and energies E_f of the scattered neutrons one can extract direct information about the phonon spectrum [14]. Neutron scattering cross section depends from sample to sample, but the neutron flux are generally relatively low, and focusing schemes not very efficient. This practically limits applications of INS at high pressure to large volume presses such as the Paris-Edinburgh press, with upper limit to about 10 GPa [15].

Inelastic X-ray scattering (IXS)

Inelastic X-ray scattering is an experimental technique that employs X-rays as probing beam. It can be applied to any material and, similarly to INS, probes the momentum-resolved phonon dispersions. An incoming photon with energy E_i and momentum $\boldsymbol{k_i}$, is scattered by a phonon of the lattice into an outcoming photon with energy E_f and a momentum $\boldsymbol{k_f}$. Excited phonon has an energy $E = E_f - E_i$ and a momentum $\boldsymbol{Q} = \boldsymbol{k_f} - \boldsymbol{k_i}$ (see Figure 1.3). Thanks to the high flux of third generation synchtrotron sources and efficient focusing schemes, IXS can be used in combination with diamond anvil cell [16]. Furthermore IXS can be used both on transparent and opaque samples, but it necessitates the third-generation synchrotron source, which makes difficult to repeat the experiments and to perform systematic studies. Furthermore, the very high energy resolution needed to resolve energy differences of the order of 10s of meV (energy of phonons) using KeV photons, makes IXS collection time very long (several hours) effectively posing problems when extreme thermodynamic conditions are difficult to maintain stable for long time.

Nuclear resonant inelastic X-ray scattering (NRIXS)

Inelastic nuclear resonance X-ray scattering is a phonon-probing technique, that in contrast to other relevant methods like IXS and INS, does not deal with phonon dispersion relations but, complementary to that, gives direct access to the phonon density of states (DOS)[17]. NRIXS is based on the Mössbauer effect for which a nucleus can emit or absorb a X-ray without loss of energy to a nuclear recoil. The absence of recoil is guaranteed by the crystal lattice. It exploits nuclear resonant isotopes as a source of X-rays: the most suitable is ^{57} Fe, that decay to the ground state, emitting a photon with a precise wavelength of 14.4 keV in the case ^{57}Fe. The sample to be investigated has to contain in its composition a Mössbauer isotope resonating at the energy of the X-ray source. The X-ray photon is absorbed by the material. In NRIXS the signal is only generated from particular nuclei with a complete isotope selectivity, and materials surrounding the sample that do not contain resonant nuclei produce no unwanted background, permitting detailed studies of iron-containing materials in a diamond anvil cell [18].This sets an important constraint in the material's choice: only samples that contain Mössbauer isotopes can be measured. Another disadvantage for the study of elasticity, is that from the phonon density of state only the Debye velocity is measured, and that derivation of compressional velocity, V_P, and shear velocity, V_S, needs the input of sample equation of state. Finally, as in the case of IXS, third-generation synchrotron radiation sources are needed for the measurements, which imposes limitations on the amount of time available to measure.

1.4.4 Picosecond acoustics

The above described limitations in the maximum attainable pressure or the choice of the materials or simply to allow more systematic investigations clearly call for other laboratory-based experimental techniques capable of routinely providing the same information and allowing the investigation of any materials. Picosecond acoustics is an optical pump-probe technique mainly used to carry out measurements of the mechanical

and thermal properties of thin-film materials, which has been recently adapted to make possible measurements of acoustic echoes in diamond anvil cell. The pulse of a fs laser is focused either directly on a metallic sample or on a transducer. When absorbed, it generates a sudden and small temperature increase (few K). The corresponding thermal stress generated by thermal expansion relaxes lunching a longitudinal strain field which propagates across the sample. Its arrival at the opposite surface is detected by the probe beam, measuring the relative variation of the optical reflectivity, (see Figure 1.4). When implemented together with a diamond anvil cell and a laser heating set-up, picosecond acoustics experiment allows to determine the elastic properties of the investigated samples at desired pressure and temperature.
As detailed in the next Chapter, travel time measurements or phonon imaging technique can be used to extract elastic constants and refine the other parameters such as sample's density and thickness. Picosecond acoustics is a powerful and promising experimental technique, which, without any loss of information, overcomes most of the constraints imposed by previously described techniques described.

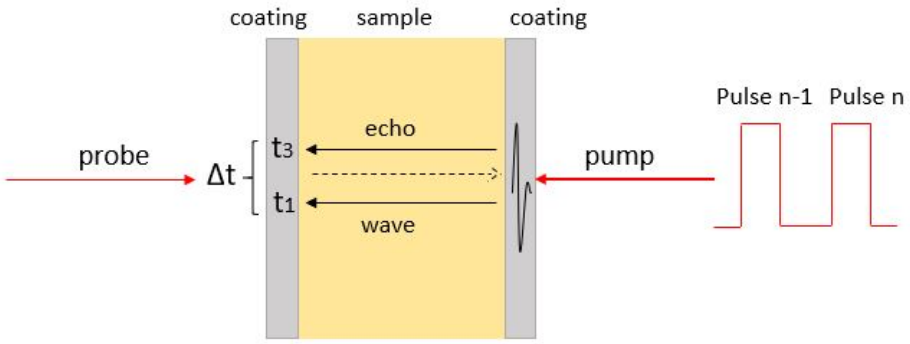

Figure 1.4: Schematic of measuring process in picosecond acoustics technique implemented in the "temporal mode". Travel times difference, Δt, between waves reflected by the sample's interfaces, is measured. A coating of sample's surfaces is sometimes necessary when the material is absorbing at the working laser wavelength to avoid the laser beams to cross the sample.

1.5 Presentation of investigated materials

Materials that have been investigated during this internship were: magnesium oxide (MgO) and ruthenium (Ru). They are respectively an insulator and a metal. The first is transparent, while the second is opaque. First material is cubic, while the second is hexagonal.
In the next sections some of the properties of the two materials directly relevant for this study, will be briefly presented together with a brief description of their geophysical interest to better understand compositions and properties of telluric (or terrestrial) planetary interiors.

1.5.1 Magnesium oxide (MgO)

MgO is an archetypal end-member forming planetary mantles. It forms a solid solution with FeO, (Mg, Fe)O, which is the second most abundant mineral of Earth's lower mantle. Elasticity of MgO has been largely studied by experimental techniques such as Brillouin spectroscopy [19]and through computations including Density Functional Theory (DFT) [20]. Being well known, MgO is routinely used to assess the accuracy of

new experimental techniques and often used as a calibrant. High quality single crystal samples are commercially available and having easy cleavage along [100] direction, sample preparation and orientation are relatively easy.
In Figure 1.5 it is shown the MgO cubic crystal structure: Mg^{2+} atoms (denoted in red, left side figure) occupy the octahedral sites and O^{2-} atoms (in yellow, left side figure) occupy other octahedral sites as well. The lattice parameter of MgO at ambient conditions is 4.212 Å and the density is 3.58 g/cm^3.

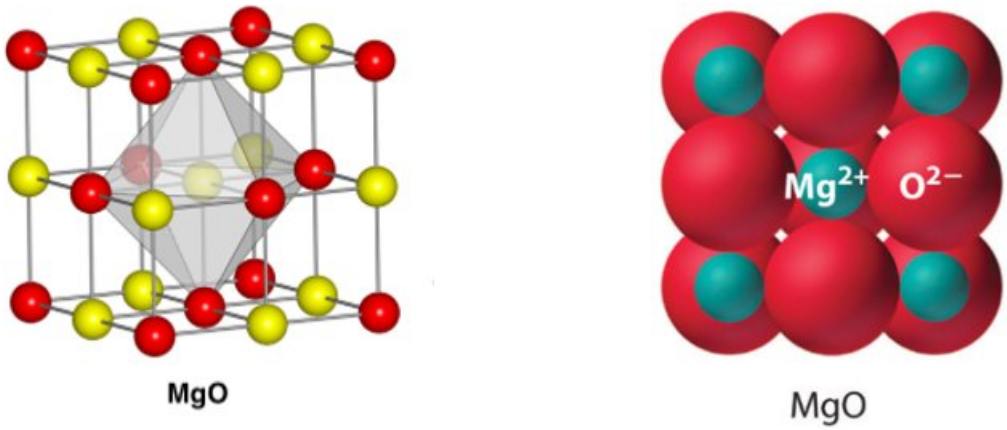

Figure 1.5: Two different representations of the crystalline structure of MgO: the one on the left highlights the cubic unit cell, whose lattice parameter is 4.212 Å; the figure on the right helps in visualizing the proportions between Mg^{2+} and O^{2-} atoms. Image on the left taken from [21], image on the right from [22].

At ambient conditions, elastic tensor of MgO, taken from [23], is presented below:

$$C_{\alpha\beta} = \begin{pmatrix} 297.7 & 95.3 & 95.3 & 0 & 0 & 0 \\ 95.3 & 297.7 & 95.3 & 0 & 0 & 0 \\ 95.3 & 95.3 & 297.7 & 0 & 0 & 0 \\ 0 & 0 & 0 & 154.5 & 0 & 0 \\ 0 & 0 & 0 & 0 & 154.5 & 0 \\ 0 & 0 & 0 & 0 & 0 & 154.5 \end{pmatrix} \tag{1.23}$$

1.5.2 Ruthenium, Ru

Ruthenium, Ru, is a 4d transition metal that belongs to the platinum (Pt) group of the periodic table [24]. From a geophysical point of view the importance of studying ruthenium is in its analogy with iron, indeed they are isoelectronic. Iron, Fe, is one of the major constituents of telluric planets' cores [25]. At ambient conditions the stable crystal structure of Fe is the body centered cubic (bcc), but the relevant crystal structure at the pressure and temperature conditions of the Earth's core is the hexagonal close packed (hcp), see Appendix C [26]. The volume change across the bcc-hcp phase transition does not allow to retain single crystal at high pressure. As such, working on analogue materials, such as Ru which is stable in the hcp structure at ambient conditions, offer an interesting opportunity. In particular, as illustrated in Figure 1.6, Ru retains the HCP structure up to 2000 K and at least 90 GPa.

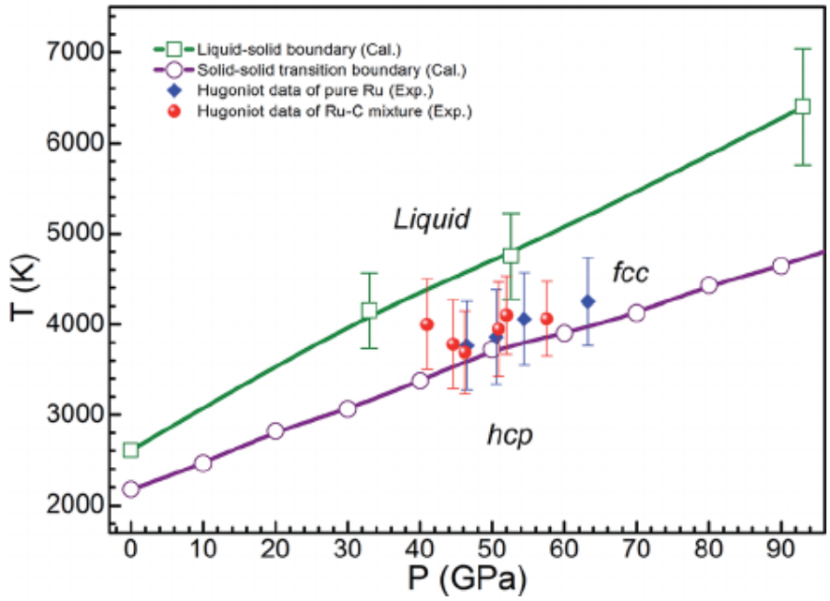

Figure 1.6: P-T phase diagram of ruthenium. The hcp structure of Ru is stable below 2000 K and until 90 GPa. Image taken from [27].

However, information on the elasticity of Ru at high-pressure and high-temperature are still limited to axial compressibility measured at ambient temperature by X-ray diffraction [24]. Further important information is the elastic anisotropy, in particular the C_{33}/C_{11} ratio, and how this evolves with pressure. Indeed, geophysical observations argue for a elastic anisotropy of the solid Earth's inner core, with seismic waves travelling 3-4% faster along polar path than in equatorial plane. Such feature is generally explained invoking elastic anisotropy of hcp iron, which however have not been measured yet. Measuring elastic anisotropy of hcp Ru can shed light on this topic.
In Figure 1.7 unit cell in hcp structure is illustrated: a and c are the two parameters characterizing the hexagonal unit cell, , the first corresponding to the size of the basal hexagonal plane, the second to the height. At ambient conditions in Ru a measures 2.705 Å and c measures 4.281 Å [24]. At high pressure, it is interesting to study not only the behaviors of a and of c separately, but also how their ratio c/a varies. In fact, the ideal value of c/a, corresponding to maximum packing, is equal to 1.633 ($\sqrt{24}/3$). At ambient conditions c/a for Ru measures 1.583 ([24]), but we expect this value to become close to the ideal one when pressure increases.

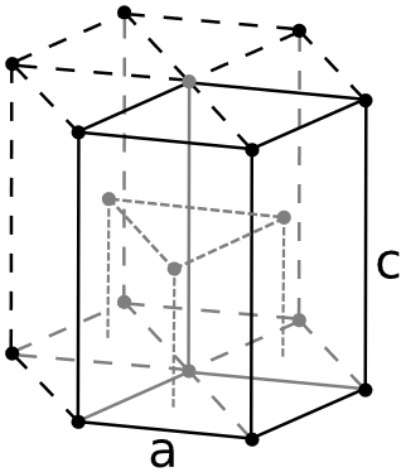

Figure 1.7: Hexagonal symmetry structure where c corresponds to the height while a to the side of the hexagon. c/a ratio is an important parameter when studying high pressure behavior of ruthenium [28].

At ambient conditions, elastic tensor of Ru, expressed in GPa, appears as reported in [29]:

$$C_{\alpha\beta} = \begin{pmatrix} 563 & 188 & 168 & 0 & 0 & 0 \\ 188 & 563 & 168 & 0 & 0 & 0 \\ 168 & 168 & 624 & 0 & 0 & 0 \\ 0 & 0 & 0 & 181 & 0 & 0 \\ 0 & 0 & 0 & 0 & 181 & 0 \\ 0 & 0 & 0 & 0 & 0 & 187.5 \end{pmatrix} \tag{1.24}$$

In a hexagonal crystal every planes passing through the principal axes, [001], are elastically equivalent.

Chapter 2

Methods: experimental techniques, analytical and computational tools

This Chapter will treat the experimental, the analytical and the numerical techniques used during this work: picosecond acoustics, and its use in combination with diamond anvil cell, the analytical methods used for the data analysis and the inversion program for the extraction of elastic constants. More precisely, section 2.1 is dedicated to the description of picosecond acoustics set-up. In section 2.2 diamond anvil cells, preparation and operation are presented. Section 2.3 deals with the sample preparation. Section, 2.4, focuses on the analytical methods for the data analysis for the extraction of the inputs for the inversion program, whose principles are described in the last section, 2.5.

2.1 Picosecond acoustics technique

Picosecond acoustics belongs to the class of pump-probe experimental techniques that employ two laser beams (pump and probe) to excite the sample and detect optical responses of ultra rapid acoustic phenomena. It exploits light pulses to generate acoustic waves. The general idea consists in detecting the different echos (reflections of the acoustic waves at sample's interfaces) to extract materials' sound velocities both at ambient and extreme conditions. Sound velocities measurements as a function of pressure carry information on how the mechanical properties' change when a material experiences an increased compression. In particular, concerning geophysical application, it is possible to compare these measurements with the seismological data, allowing for the inference on planets' inner constituents.
Figure 2.1 shows a picture of the experimental setup, in which the most important components are indicated:

1. Laser source;
2. Polarizing beam splitter. It splits the laser coming out from the laser box into two beams: pump and probe;
3. Delay line. It produces a time delay between probe and pump beams;
4. Acoustic-optic modulator (AOM). It modulates pump beams with squared pulses of 1 MHz each to enhance signal to noise ratio by Lock-in techniques;
5. Pump objective;
6. Probe objective;

7. Michelson inteferometer.

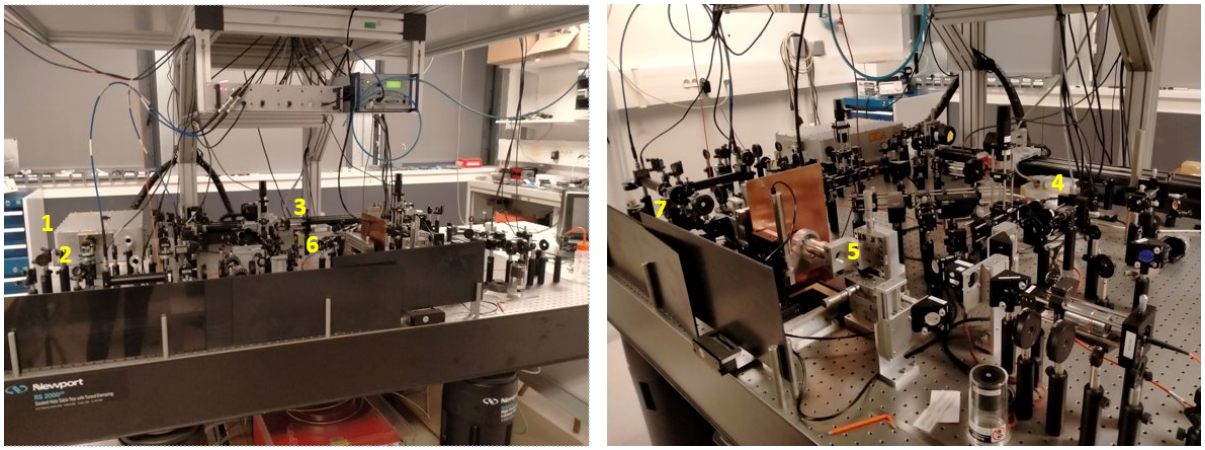

Figure 2.1: Picture of the set up seen from two different perspectives. The principal components are indicated by numbers: 1. Laser source 2. Beam splitter, which divides pump and probe beams 3. Delay line, which delays probe beam with respect to pump, 4. AOM (acoustic optic modulator), imposing a time structure exploited by the Lock-in system to gain in signal to noise ratio, 5. Pump objective 6. Probe objective, 7. Michelson interferometer, needed for measuring the imaginary part of the change in sample reflectivity.

2.1.1 Signal generation

Qualitatively, the signal generation occurs as follow (see Figure 2.2): a pulsed laser beam, called the pump beam, hits sample surface (or a coupler deposited on the sample surface) in one spot, causing the material to increase locally its temperature, creating a thermal gradient. The so-generated thermal stress relaxes through a strain (acoustic waves) that propagates across the sample. At the probe-side surface, the arrival of the train of waves is detected by probe beam and is partially transmitted and partially reflected back to the pump-side surface, where, again it is partially reflected. Depending on sample attenuation and acoustic mismatch at interfaces, the first arrival or multiple echoes are detected.

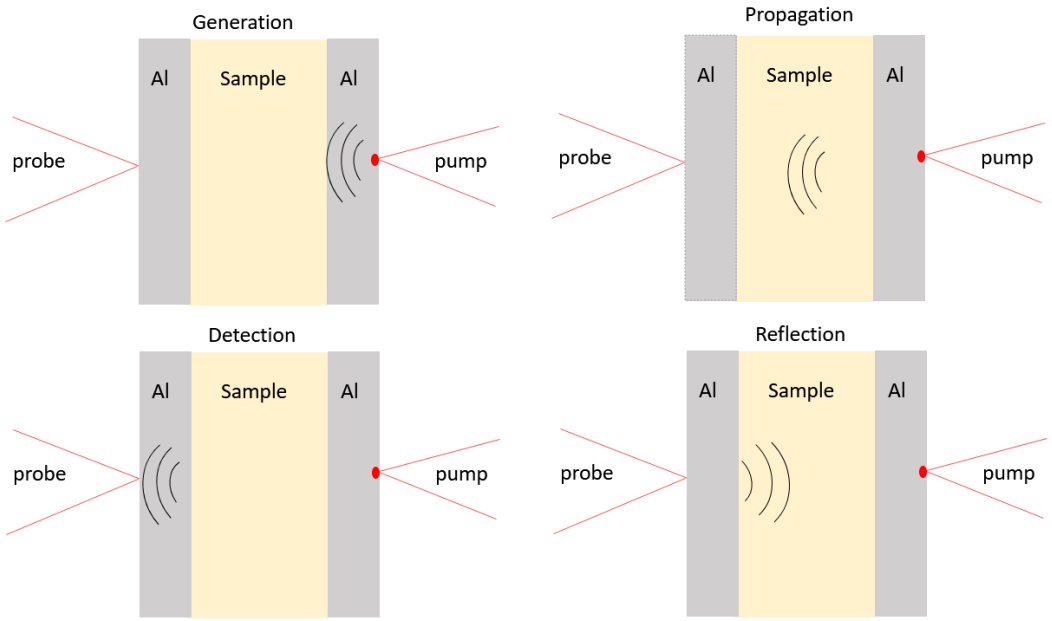

Figure 2.2: Working principle for signal generation and detection for a sample for which an Al coating (coupler) is necessary to improve coupling with the laser.
First (top left) the pump, focused on the surface, generates the acoustic waves; then, they propagate through the sample (top right), and arrive to the other surface where probe detects the signal (bottom left); and finally they are partially reflected back, creating the echo (bottom right) inside the sample.

The amplitude of the elastic waves decreases during propagation because of inelastic and dissipating effects, the attenuation is generally less the harder is medium [8]. A detailed mathematical treatment about signal generation in picosecond acoustics is presented in [30].

2.1.2 Signal detection

In picosecond acoustics, the probe beam detects the change of reflectivity that occurs at the sample surface when acoustic waves arrive. Qualitatively, both acoustic and thermal effects alter the optical reflectivity in two ways: the photo-elastic effect, which affects the real part of the optical reflectivity, and the surface displacement, mostly visible by measuring the imaginary part of the optical reflectivity. Indeed, remembering that:

$$R = \left|\frac{1-n}{1+n}\right|^2 \tag{2.1}$$

a change in the refractive index, n, causes reflectivity, R, to change.
The mathematical treatment describing this phenomenon is reported in Appendix D. Here the main result, expressing the sample's reflectivity change, $\frac{\Delta r(t)}{r}$, is shown:

$$\frac{\Delta r(t)}{r} = \mathrm{i}k_0 \left\{ 2u_0(t) + \frac{4n}{1-n^2} \int_0^{+\infty} \mathrm{d}z \left[\frac{\partial n}{\partial T}\Delta T(z,t) + \frac{\partial n}{\partial \eta}\Delta\eta(z,t) \right] e^{2\mathrm{i}k_0 n z} \right\} \tag{2.2}$$

The change in reflectivity is a complex number that has several terms: $u_0(t)$ describes the surface displacement caused by the acoustic wave's propagation, $\frac{\partial n}{\partial T}\Delta T(z,t)$ corresponds to the temperature increase caused by pump, while $\frac{\partial n}{\partial \eta}\Delta\eta(z,t)$ describes the effect of a deformation η on the optical properties of a material,where $\frac{\partial n}{\partial z}$ is the photo-elastic coupling coefficient [31].
Equation 2.2 can be rewrite in a simpler form as follows:

$$\frac{\Delta r(t)}{r_0} = \rho(t) + j\phi(t) \tag{2.3}$$

where $\rho(t)$ is the real part and $\phi(t)$ is the imaginary part.
Picosecond acoustics measures either the real part, $\rho(t)$, or the imaginary part, $\phi(t)$, of the change in reflectivity through two different set-up configurations, reflectometry mode for the real part and interferometry mode for the imaginary part. These two modes will be treated in details in this Chapter. Whether is preferable to detect the signal in one configuration or in the other depends on which of the terms in Equation 2.2 dominate. The theoretical prediction of which are the dominant terms for the studied materials is beyond the scope of this thesis. For each sample we will use the mode that will grant us the best detection of the signal.
One important aspect that needs to be stressed concerns the quality of the sample's surface. Since all the set-up is based on reflection processes, sample's surface should be mirror quality. More details about this aspect are presented later in this chapter in the section dedicated to the sample preparation. The detailed mathematical treatment about signal detection in picosecond acoustics is provided by [30].

2.1.3 Main components of picosecond acoustics set-up

Laser

The laser is a Ti:Sapphire type working at a wavelength of 800 nm (frequency of 80 MHz = 12.55 ns) with a pulse width of 100 fs. The Ti:Sapphire laser is split by a 90:10 polarized beam splitter (PBS) into two different laser beams, pump (90) and probe (10), where the first is devoted to the excitation and the second to the collection. High intensity pump beam is required to induce the thermal stress necessary for the generation of acoustic waves. Pump and probe will be described in detail separately in the next lines.

Pump beam

Pump beam is an high-power laser beam aimed at the excitation of acoustic waves inside the sample. Once out from the PBS, it goes into the AOM (acoustic-optical modulator) that modulates it with a frequency of 1MHz. Taking into account that the change in reflectivity is small and so, difficult to be detected, pump beam is modulated in frequency, in order to allow Lock-In rejection of the noise and improve on the signal to noise ratio. The pulsed behaviour of the pump is the key of generation, in fact it acts like an hammer which produces a big hit on a sample spot in a very short time interval. Thus, the pump beam is focused on a spot of few microns in diameter ($2 \quad \mu m$), causing a rapid and localized increase of temperature. The beam also necessitates to be highly focused, to guarantee the generation of spherical acoustic waves.

Probe beam

Probe beam is much less intense than pump and is devoted to the detection of the signal. It goes into a optical delay line, which introduces a time delay in the probe beam with respect to pump beam, allowing the detection of the signal at different time instants, as it will be explained in the section dedicated to the delay line. However, even at the minimal difference in the path, due to set-up construction features, pump and probe beams are not perfectly coincident, and pump beam hits the material at a time $t_0 \neq 0$ ns in the reference system of probe beam. Time t_0 can be evaluated thanks to a simple reasoning based on the equality of all the Δt, as:

$$t_1 - t_0 = t_2 - t_1 = t_3 - t_2 = \Delta t \;\rightarrow\quad t_3 - t_1 = 2 \times (t_1 - t_0) \rightarrow\quad t_0 = t_1 - \frac{t_3 - t_1}{2} \quad (2.4)$$

The offset time, t_0, is then derived substituting in the previous section the arrival times collected from ruthenium ambient pressure measurements, obtaining for the configuration used in this thesis work:

$$t_0 = t_1 - \frac{t_3 - t_1}{2} = 0.308\ ns$$

Pump and probe objectives

Long working distance (20 mm focal length) 20x objectives are used to focus both pump and probe beams down to a spot of about 2 μm in diameter. This high spatial resolution is crucial to provide a point source for acoustic waves generation and as well for the detection, enabling the possibility to probe a signal from a material's portion of diameter of 2μm, property fundamental for temporal mode measurements, as it will be explained later in this chapter. However, the high spatial resolution leads to the necessity of performing a scan of the sample surface to acquire a 2D image in imaging mode.

Delay line

Probe beam is temporally delayed with respect to pump beam by means of the delay line so to capture the propagation of the acoustic waves at an arbitrary time after its generation [31]. This is practically achieved by increasing the optical path of the probe beam. The delay line is composed by three back reflectors, see Figure 2.3: two are movable and they are placed in front of a third fixed one. Incident beam is totally reflected by a mirror to the first movable back reflector. Here, it is reflected to the opposite fixed back reflector and then to the second movable one. Movable mirrors travel up to a maximum distance of $\sim$ 1 m moving with velocity, v, adjustable between 1 mm/s and 100 mm/s. The probe beam performs inside the delay line an optical path of minimum $\sim$ 0.1 m and maximum $\sim$ 4 m, that are the minimum and the maximum positions of the movable back reflectors. This allows to introduce a temporal delay to the probe beam with respect to the pump beam from a minimum of 0.1 ns to a maximum of 13.3 ns.

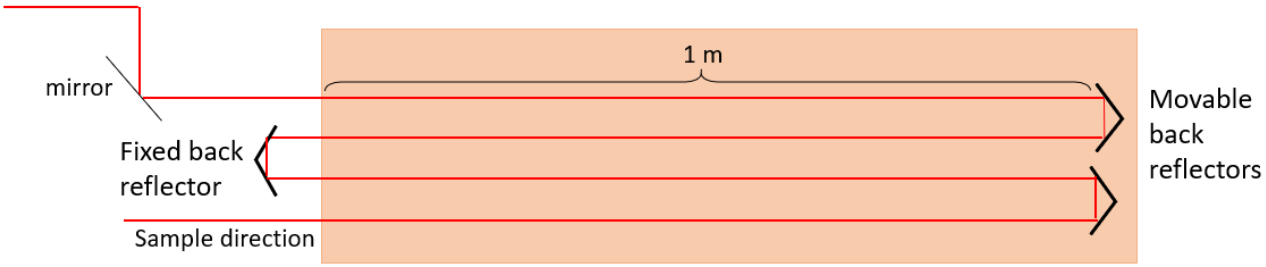

Figure 2.3: The delay line is a displacing optical system that introduces a time delay on probe beam with respect to pump by increasing the optical path of the probe beam by a controlled distance, up to 1 m. Mirrors move with velocity, v, adjustable between 1 mm/s and 100 mm/s.

Fixing the position of the movable back reflectors to a selected position, x, along the delay line (see Figure 2.4), the corresponding temporal delay, t_{delay}, is obtained as follows:

$$t_{delay} = \frac{4(x + t_0 c)}{c}$$

where c is the light velocity and 4 corresponds to the total number of the reflections of probe beam inside the delay line. Before t_0, the probe beam arrives earlier than the pump beam and no time delay in the probe beam with respect to the pump is introduced.

Figure 2.4: Position of the movable back reflectors along the delay line.

AOM (acoustic-optic modulator)

Pump beam passes through an acoustic-optical modulator which modulates it with a given frequency (F) of 1MHz in a way to allow a Lock-In amplifier to enhance the acoustic signal from external noises. A train of waves is generated inside the AOM, producing a change of refractive index and creating a network of refractive indices that diffracts the incoming beam imposing to a characteristic modulation (see Figure 2.5).

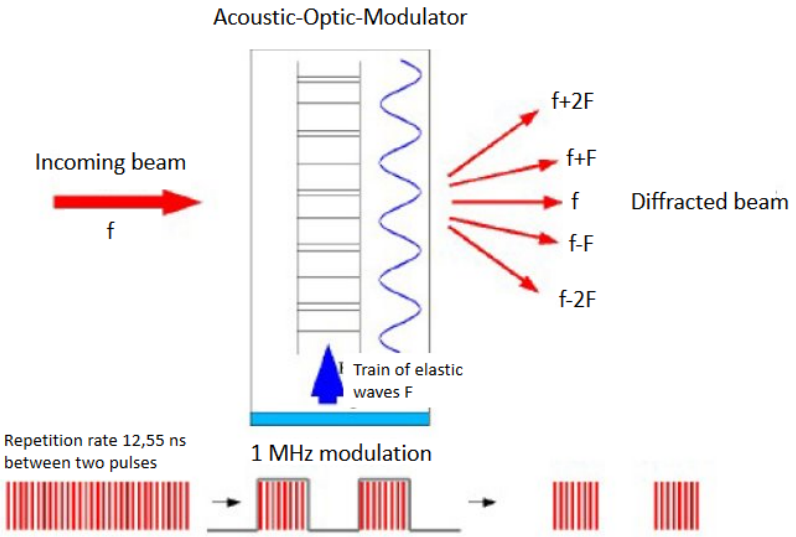

Figure 2.5: Pump diffraction by train of elastic waves generated by the modulator. While propagating, the acoustic wave modifies the refractive index of the medium that leads to the diffraction of pump beam, that change its frequency as f $\pm$ nF, where f is the initial pump frequency[31].

2.1.4 Operational modes

As already pointed out in section 2.1.2, there are two operational modes in picosecond acoustics depending on the detection mode: reflectometry mode, to measure $\rho(t)$, and interferometry mode, to measure $\phi(t)$, see Equation 2.3.
Here both modes will be explained in more detail. Besides the possibility of working in interferometry or in reflectometry modes, experiments can be run either in temporal, imaging and movie modes. These operations modes will be presented later on.

Reflectometry mode

The set up in reflectometry mode is schematically presented in Figure 2.6. Briefly, the probe beam is focused on the sample surface opposite to the one where the acoustic wave is generated. The intensity of the reflected is measured through a photodiode. Thus, variation in the reflectivity due to the arrival of an acoustic wave can be directly measured.

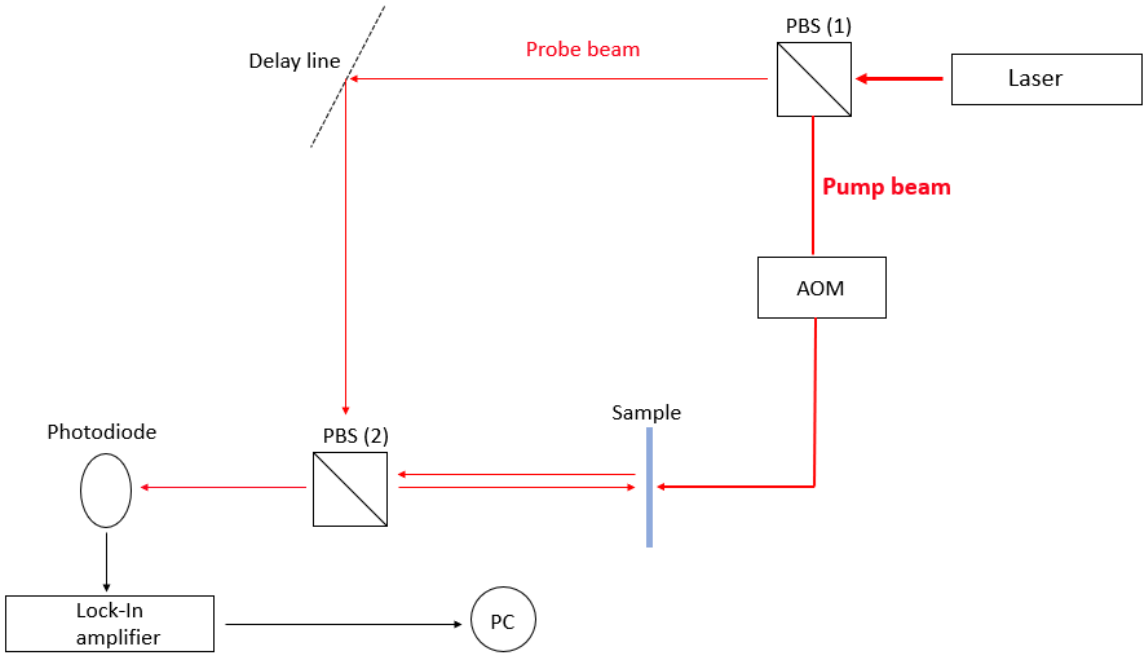

Figure 2.6: In the reflectometry mode, the intensity of the probe beam reflected by the sample surface, is measured by a single photodiode.

Interferometry mode

Interferometry mode exploits a Michelson interferometer. Before impinging on sample surface, probe beam is split by an additional 50:50 PBS into two separate beams: probe 1 and probe 2. Probe 1 is reflected directly by the sample surface, while probe 2 is reflected by a mirror, whose position is set to provide interference fringes. Thus, these two reflected beams will serve as inputs for the Michelson interferometer. After their respective reflections, the two beams enter the two photodiodes, A and B, which convert them in electrical signals. When an elastic wave produces a change in the imaginary part of sample reflectivity, it is possible to record it by analysing the interference pattern changes.

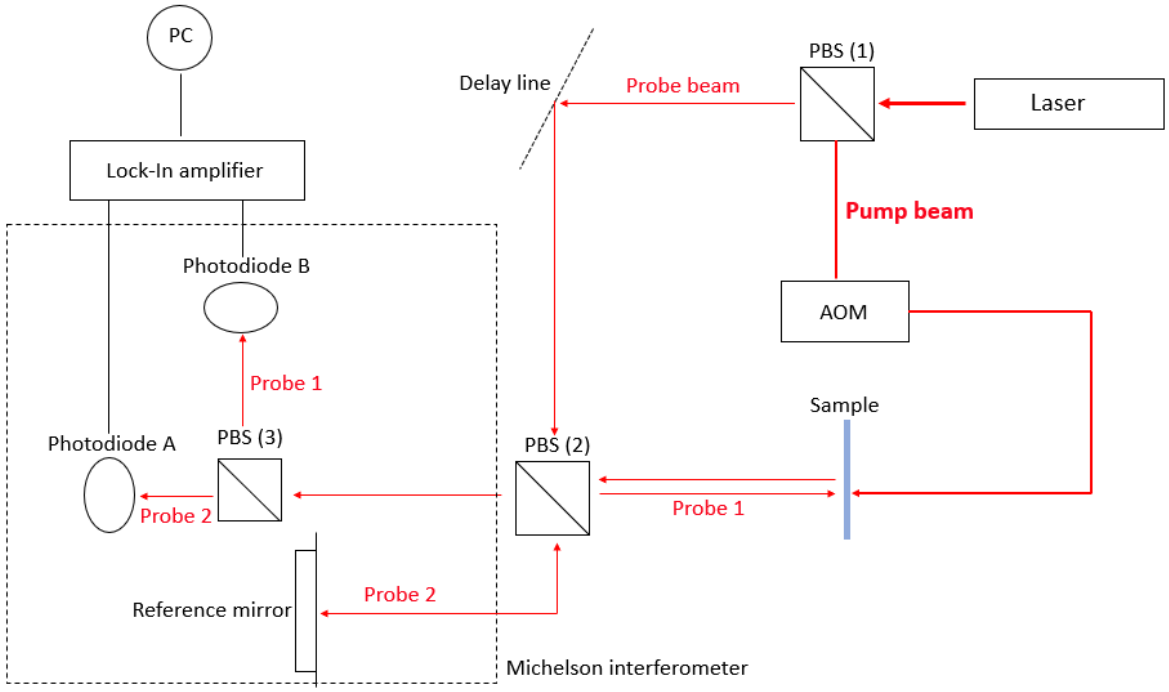

Figure 2.7: In the interferometry mode, a Michelson interferometer is exploited to measure the imaginary part of $\Delta r/r_0$. Probe beam, before being focused on the sample, is split into two beams with equal intensities: one goes into the interferometer, being reflected by a mirror, while the other goes directly on the sample. After the respective reflections, the two beams enter two different photodiode and their interference pattern is used to deduce the change in reflectivity.

Temporal mode

In temporal mode, pump and probe beams are collinear and the objectives are kept fix during the measurements. This set-up is conceived to detect particle displacements normal to the sample surface, that are generally produced by longitudinal waves[1]. Thus, data collected from a temporal measurement will provide information about longitudinal waves, including multiple echos (waves produced by previous or subsequent laser pulses that are reflected by the sample's interfaces). Because of the periodicity of the laser pulses, occurring with a repetition rate $T = 12.55\ ns$, all the acoustic waves, including the echos generated by previous laser pulses, can be detected in a unique temporal window of 13.3 ns, that is the maximum time delay provided by the delay line. Thus, the non-scaled arrival time, $\bar{t}_n$, of an acoustic wave is derived from the detected one, t_n, as:

$$\bar{t}_n = t_n - t_0 + kT \tag{2.5}$$

where k is the number of the laser pulse.
In Figure 2.8 a typical plot of measurements in temporal mode is shown. The arrival of longitudinal waves produces a sharp intensity variations (sort of peaks) like the ones visible around 7 ns, 8.5 ns, 9.9 ns and 10.9 ns.

[1]The transverse waves can have a component that leads to a particle displacements normal to the surface allowing their detection.

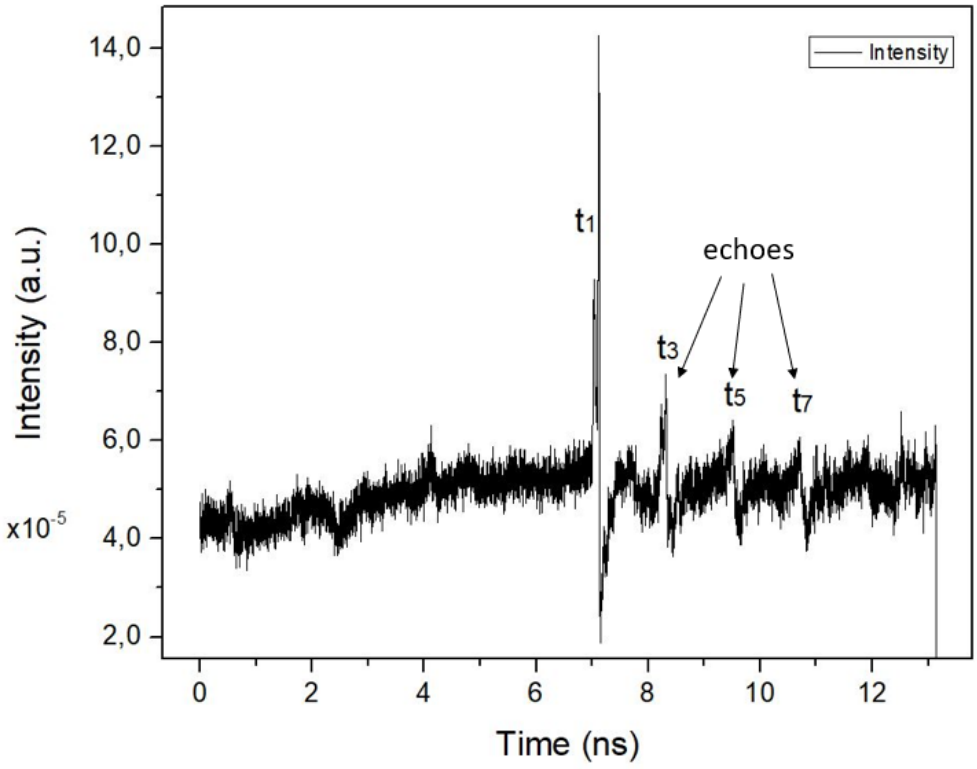

Figure 2.8: Reflectivity as a function of time acquired on Ru sample (48 μm thick) with [001] direction along the beam path. Around 7 ns an intense peak occurs, t_1: it corresponds to the arrival of the longitudinal wave. Between 8 and 9 ns, at t_3, another wave, less intense arrives: it is the echo of acoustic wave that have been generated by previous laser pulse. Other two echoes of acoustic waves that were generated by, respectively, two and three previous laser pulses, are detected between 9 and 10 ns, at t_5, and between 10 and 11 ns, at t_7.

Imaging mode

In this operational mode, a 2D image of the sample surface is obtained. The probe objective is mounted on a piezoelectric stage, whose controlled motion enables the possibility to scan, at a fixed delay time, the sample surface and thus reconstruct a 2D image over an area of 100 μm x 100 μm. This mode can work either in DC mode (without using the Lock-In amplifier), producing an actual picture of the surface, or in Lock-In mode, using the Lock-In amplifier, whose cutoff frequency is set to cut most of the noise coming from sample surface defects and from external perturbation (ambient light, etc.). The DC image is generally used to check sample surface quality and homogeneity, as well as to refine the laser focus. An example of DC mode image is presented in Figure 2.9, where the black spots are surface defects.

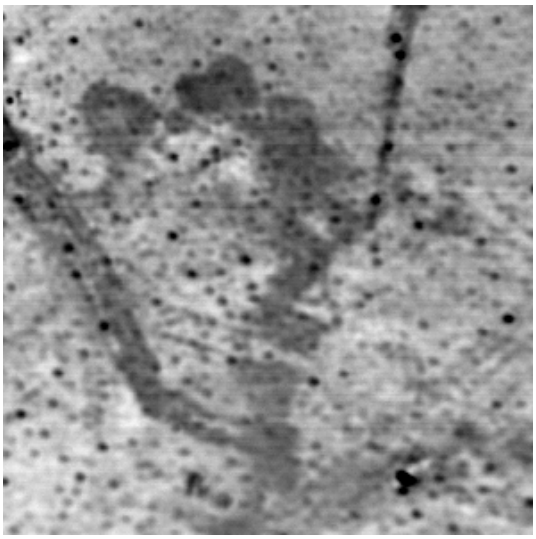

Figure 2.9: $100 \times 100\ \mu m$ DC image of the surface of MgO single crystal (001).

The imaging mode with the Lock-In on produces as well a 2D image of sample, as represented in 2.10, but the frequency cutoff is such to optimize the visualization of the acoustic waves (circles in Figure 2.10) at the sample's surface, and is used to collect data.

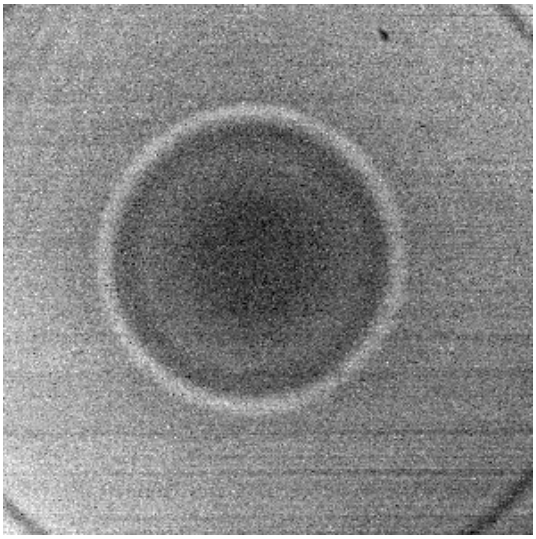

Figure 2.10: $100 \times 100\ \mu m$ image showing the acoustic waves on Ru single crystal oriented with surface normal along (001).

Movie mode

The movie mode is an operational mode similar to imaging mode, but in which the delay line moves in between each 2D image by a step decided by the experimenter and collects data over a chosen time lapse. In this mode collected data are saved as a set of images, each corresponding to a different position of the delay line, and hence different time delay between pump and probe. A subset of such data is represented in Figure 2.11.

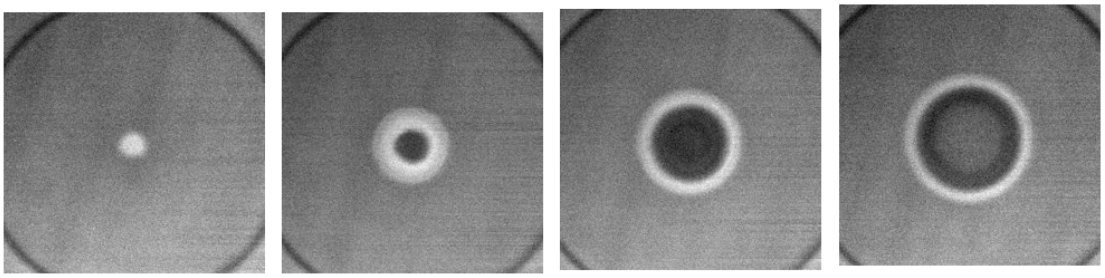

Figure 2.11: Acoustic waves propagating inside ruthenium (68 μm thick), recorded in movie mode from 9.750 ns to 10.500 ns, with the delay line moving with a step of 0.250 ns from one image to the following.

2.2 Diamond anvil cell for high pressure generation

Diamond anvil cell (DAC) is a unique apparatus capable of generating static pressure (P) in excess of hundreds of GPa and allowing a large variety of in situ measurements. Since its invention in 1959, the DAC has evolved to become the most powerful tool among all static high-P research apparatuses. All DACs have the common key component of two opposed diamond anvils that generate P and provide transparent windows for optical and x-ray access. The principle of the DAC design is simple: two opposing diamond anvils with small culets point to each other, and the sample is squeezed between these two (see Figure 2.12). A single-crystal diamond is the chosen anvil material because of its unique properties, including its unmatched extreme hardness to support high P, chemical inertness, transparency to infrared, visible, and ultraviolet radiations (< 5 eV) for optical spectroscopy, transparency to X-ray (> 10 keV) for X-ray diffraction, spectroscopy and imaging, and compatibility for electrical and magnetic transport measurements [32].

Figure 2.12: Picture of the open DAC which has been used for the experiments.

Figure 2.13 shows a picture of diamond culet seen through a microscope.

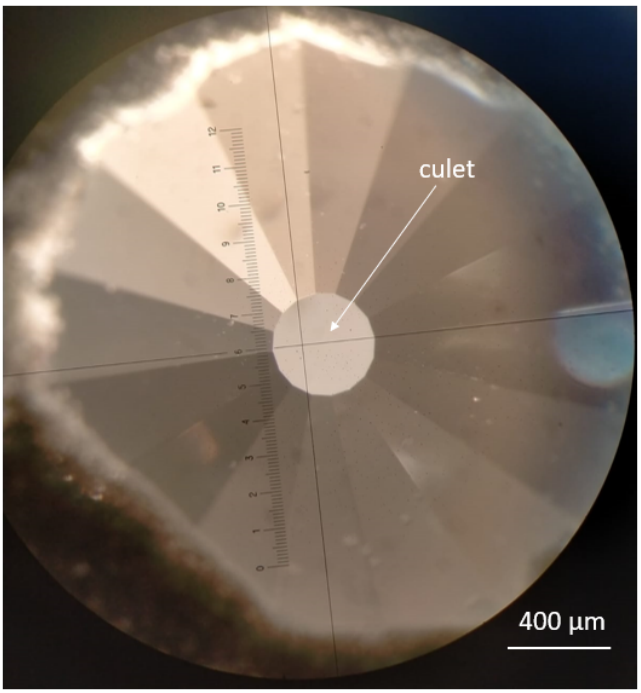

Figure 2.13: Image of diamond culet seen through the microscope. Diamond culets are required to be flat and perfectly parallel in order to generate uniform pressure. The alignment of the diamonds' culets is done by looking at the interference fringes through the microscope: when there are none the two diamonds are parallel. Diameter of culets is selected according to the target pressure and other experimental constraints remembering that $P = \frac{F}{A}$ and so higher pressures require diamonds cut with smaller culets.

2.2.1 Gasket and gasket indentation

The gasket is a thin metallic foil of $\sim$ 200 μm of thickness, which is placed between the two diamonds and acts as sample chamber. A desirable material to be employed as gasket is Rhenium because is a hard material that supports high pressures without excessive deformations. First step in preparing a DAC is the gasket indentation: the gasket is placed between the two diamonds and squeezed by applying a force to the cell so to increase the pressure and let the diamonds' culets leave a permanent imprint on the gasket and reducing the initial gasket thickness to the desired one. The so-produced gasket is then drilled at its center (e.g. by a laser) so to serve as the sample chamber. Gasket thickness during indentation is estimated based on previous experiences, either by monitoring the pressure on the membrane used for compression or by measuring the pressure by an optical gauge (see next section). Figure 2.16 shows a picture of a gasket after the indentation.

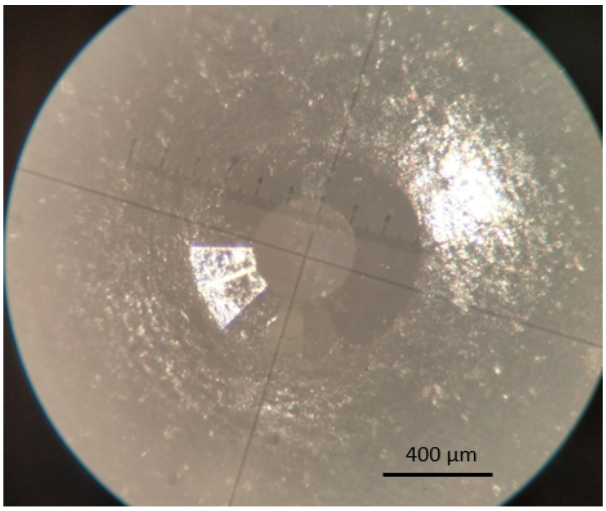

Figure 2.14: Image of indentation of a Rhenium gasket foil taken at microscope. Gasket indentation is performed by diamonds culets (diameter 400 μm) which squeeze the gasket without the sample till it reaches the desired thickness (65 μm in the present case).

2.2.2 Ruby fluorescence shift as P calibrant

The force applied to a DAC is transmitted to the anvil culets and generates a P distribution which can be probed and mapped by internal calibrants. Limiting to experimentation at ambient temperature, ruby is the most largely used optical gauge, because its very intense and characteristic fluorescence signal. Fluorescence signal is sensitive to P changes and has been calibrated and tested using many pressure transmitting media [32].

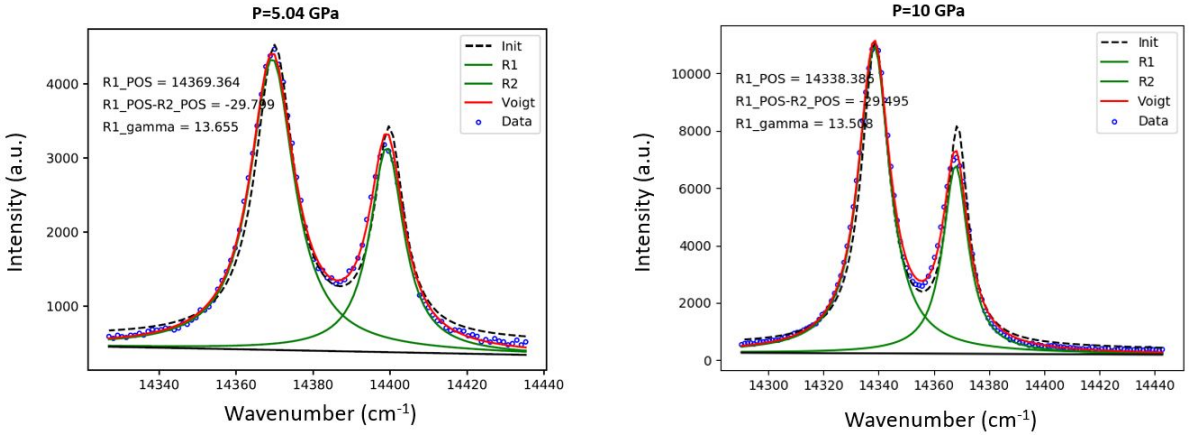

Figure 2.15: Ruby fluorescence collected at two different pressures: on the left pressure is 5.04 GPa and on the right 10 GPa. Position of R_1 peak, the first and most intense of the two ruby fluorescence peaks, is calibrated against pressure: on the left $R:1$ position corresponds to a wavelength of 696.5 nm, while on the right R_1 peak wavelength is at 697.3 nm.

The pressure is derived from the measured wavelength of the R_1 fluorescence line according to the relation provided by [33]:

$$P_R = \frac{A}{B}\left[\left(\frac{\lambda}{\lambda_0}\right)^B - 1\right] \tag{2.6}$$

where A= 1904 GPa, B=9.5 GPa, λ_0 is the uncompressed ruby wavelength and corresponds to 694.3 nm, and λ indicates the ruby fluorescence wavelength at a given pressure. The transparency of diamonds to laser and ruby fluorescence wavelengths guarantees the possibility to perform fluorescence spectroscopy measurements at high pressure. Examples are reported in Figure 2.15.

2.2.3 Sample chamber

The sample chamber contains the sample. Once the indentation is done, through a laser beam is possible to cut within the gasket a cavity centered within the imprint left by the diamonds, creating in this way the sample chamber. Thanks to the previous indentation, two rims running around diamond culets have been created. Since rhenium is an hard material, the scope of the two rims is to exercise an opposition to the horizontal stress occurring parallel to the plane of the gasket and thus, avoiding the sample chamber to be totally squeezed.

2.2.4 Pressure transmitting medium

The vast majority of high pressure experiments are aimed to be carried out under hydrostatic conditions, as under uni-axial deformation not every sample's portion experiences the same experimental conditions. The practical realization consists of immersing the sample in a fluid pressure transmitting medium (PTM) which is supposed to support no shear. However, the melting line of fluids increases with pressure and solidification inevitably occurs at some pressure value. Beyond this value, the pressure across the experimental volume is generally inhomogeneous and differential (mostly uni-axial) stress and shear stresses appear [34]. PTM are selected based on their inertness to the sample, compatibility with the experiment, operational convenience, and the degree of quasihydrostaticity in the experimental P-T range. For example, a 4:1 methanol/ethanol mixture and silicon oil are fluid P media for experiments below 10 GPa but harden at higher P[32]. In high-pressure measurements performed during this internship, we used methanol/ethanol 4:1 mixture. It was shown by numerous groups that the glass transition is at 4 GPa and the loss of the quasi-hydrostaticity occurs at 10.5 GPa [34].
Figure 2.16 schematically show a DAC sample chamber containing the sample and a pressure marker embedded in a PTM.

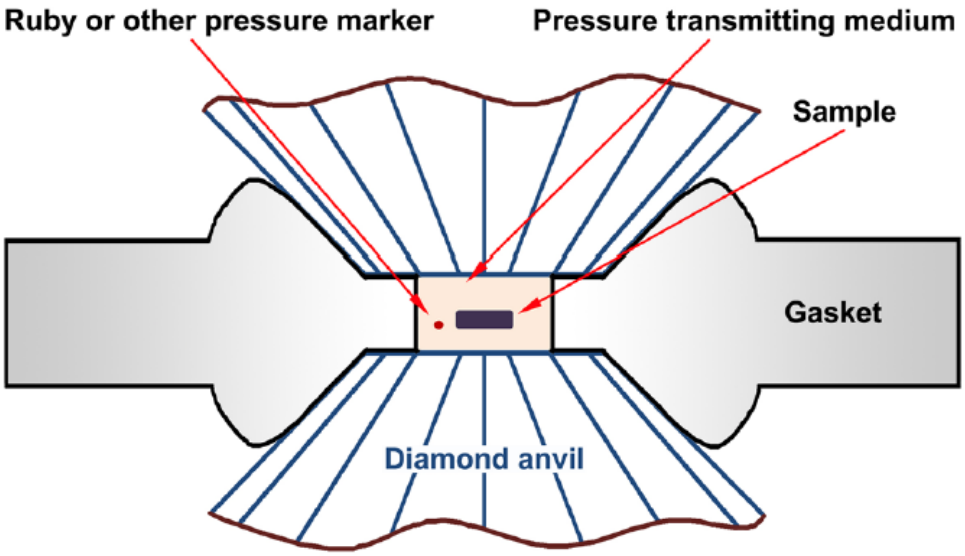

Figure 2.16: The principal components of the DAC are shown: two opposed diamond culets squeeze the sample that is contained inside the sample chamber. Sample chamber is created starting from a rhenium foil, called gasket. Inside the sample chamber, beyond the sample, a ruby, working as a pressure calibrator, and a pressure transmitting medium, are contained as well[32].

2.2.5 Implementation of DAC in picosecond acoustics

Implementing an experimental protocol to allow picosecond acoustic measurements on single crystals compressed in diamond anvil cell is one of the objectives of this thesis work. This configuration enables the possibility to measure elastic constants and sound velocities at high pressures. In Figure 2.17 the complete set up is presented. The set-up is the same as the one already presented in the beginning of the chapter, with the addition of the DAC containing the sample. High- pressure measurements on Iron using picosecond acoustics technique combined with DAC up to $\sim$ 150 GPa are is presented by [35]. We stress however, that these measurements are limited to temporal detection on polycrystalline samples. Measurements on single crystals are so far limited to cubic samples and $\sim$ 8 GPa [36].

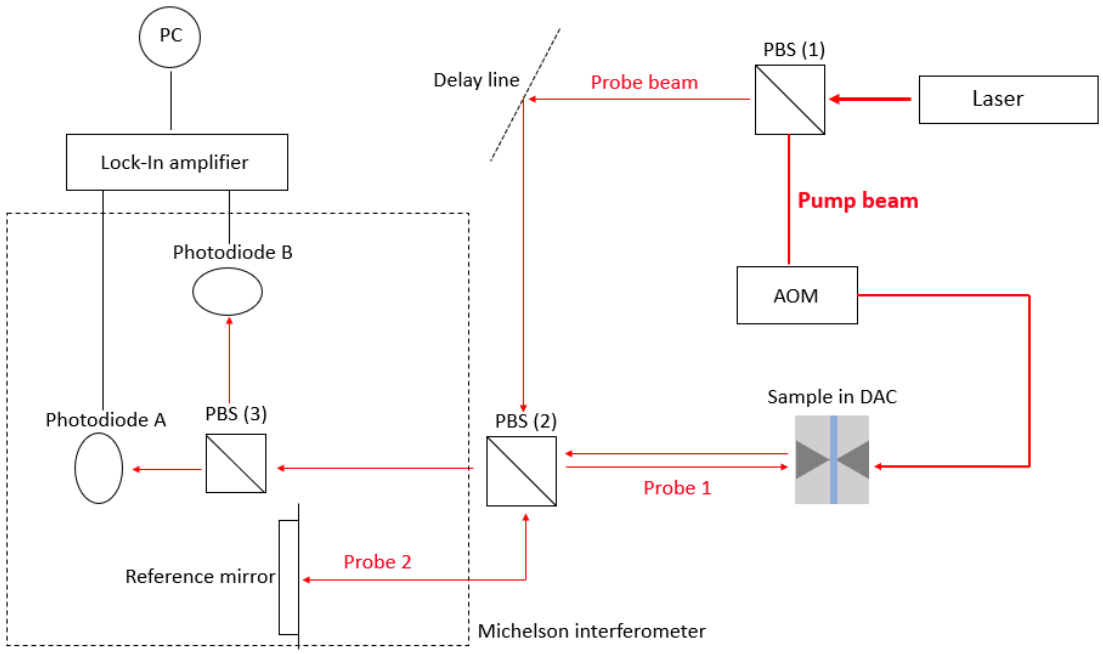

Figure 2.17: Schematic diagram of picosecond acoustics set up in combination with the DAC in the interferometry configuration.

2.3 Sample preparation

Both picosecond acoustics and DAC impose constraints on given characteristics of the sample. Firstly, since signal generation and detection are based on reflection processes, sample surfaces need to be of high quality. Secondly, the sample needs to be optically opaque to infrared wavelength otherwise the generation does not occur. If the studied sample is not opaque a coating is necessary. Moreover, in order to be suitable for DAC, sample should have thickness of the order of tens of μm and a diameter of hundreds μm, or less. In the next paragraphs the various steps in sample preparation are separately described.

2.3.1 Sample orientation

Orienting the sample along one precise crystallographic direction is an important step to be done before proceeding with the sample polishing (process leading to high quality surface and desired thickness) because it determines which elastic constants can be derived from the inversion of the Christoffel equation. The most commonly used methods for single crystal orientation are X-Ray diffraction and the orientation by apparent crystallography for big samples. Specific to this work, the samples used were bought already oriented along a precise direction. For cubic symmetry single crystals, like MgO, the direction [001] gives access to all the independent elastic constants, while for hexagonal symmetry single crystals, like Ru, two directions, for example [001] and [010], are needed to obtain the all independent components of the elastic tensor.

2.3.2 Sample thickness and high quality surfaces

To obtain both the desired thickness and the needed surface quality, a mechanical polishing machine was used. By using a rotating disk on which is glued a paper with diamond grains of selected dimensions, one can perform both rough polishing for thinning (coarse diamonds grains) and fine polishing for final surface quality (0.5 μm diamond grains).

2.3.3 Surface coating

The studied samples necessitate to absorb the infrared wavelength to allow the generation and the detection of acoustic waves. The penetration length, δ_P, of the laser inside the sample depends strongly on its optical properties and for each new sample it has to be established if a coating acting as laser coupler is necessary or not. The coating generally consists of a deposition of thin layer, of tens to hundreds of nm, of a material, typically a metal, which absorbs in the infrared, for example Aluminum.
The Lambert-Beer law describes the attenuation of a radiation passing through a material, as follows:

$$I_1 = I_0 e^{-\alpha l} \tag{2.7}$$

where α is the absorbance coefficient, I_0 the incident radiation intensity and I_1 the radiation intensity once out from the material.
The penetration depth is defined for $I_1 = 0.37 I_0$, when Equation 2.7, becomes:

$$\delta_p = \frac{1}{\alpha} \tag{2.8}$$

It is empirically observed that when $\delta_P > 20\ nm$ a coating is necessary.
Other than absorption, there are different parameters on the basis of which the coating material can be chosen: acoustic impedance, optical reflectivity of the coating material, chemical affinity between sample and coating material. The acoustic impedance difference between the coating and the sample should be small to maximize the transmission of the acoustic energy; coating's reflectivity is required to be high to guarantee laser reflections and chemical affinity is recommended to deposit an homogeneous coating layer [31].

2.4 Analytical methods

This section presents the analytical methods used for the data analysis of temporal and imaging data.

2.4.1 Temporal data

The temporal data provides the acoustic waves' arrival times. Exploiting the periodicity of the laser repetition rate, all the acoustic waves, including their echoes, are acquired in an unique temporal window, whose range is determined by the delay line and goes from 0.1 ns (minimum pump-probe delay time) to 13.3 ns (maximum pump-probe delay time). The difference between two successive arrival times, t_n and t_{n-2}, is the travel time:

$$\Delta t = t_n - t_{n-2} \tag{2.9}$$

A simple relation relates travel time Δt, sample thickness l and sound velocity V:

$$l = \frac{V \times \Delta t}{2} \tag{2.10}$$

where the division for 2 is motivated by the fact that the acoustic waves cross the sample twice between two successive arrival times, being the detection only at probe sample surface, as shown in Figure 2.18.
An exception to Equation 2.10 is when t_0 and t_1 are the arrival times considered: in this case the acoustic waves cross the sample only one time. The correct equation for this case is:

$$l = V \times \Delta t \quad \text{where} \quad \Delta t = t_1 - t_0 \tag{2.11}$$

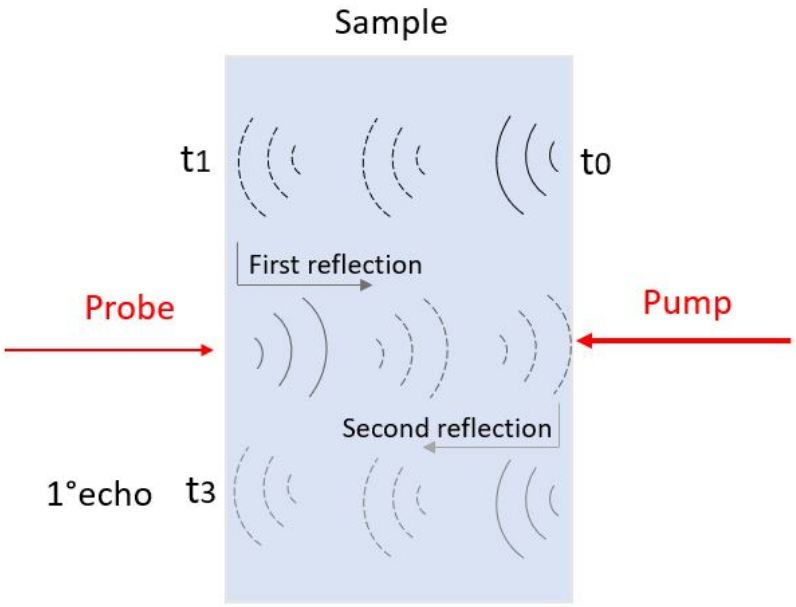

Figure 2.18: Arrival times of the acoustic waves and of the first echo at probe sample surface. The image has a clarifying purpose and is not a realistic representation because the inner reflections at the interfaces occur at the same sample position.

2.4.2 Imaging data

The data acquired in imaging mode are 2D images of the acoustic waves arriving at the sample surface. The function describing the variation of the acoustic wave's radius with respect to the delay time is provided by a simple mathematical derivation using the geometrical construction illustrated in Figure 2.19:

$$R(t) = \sqrt{x^2(t) - l^2} \rightarrow$$

$$R(t) = \sqrt{(V_\phi^2(t - t_0 + kT)^2 - V_{[001]}^2(t' - t_0 + kT)^2} \tag{2.12}$$

where V_ϕ is the acoustic wave velocity at a given angle ϕ; t is the acoustic wave's arrival time at a generic position of the sample's surface; t' is the acoustic wave's arrival time at the focus spot's position; t_0 is the time of the acoustic wave's generation (introduced in the section "Probe beam"); k denotes the k-th laser pulse and T is the repetition rate. The Equation 2.12 describes a parabolic relation between the acoustic wave's radius and the time.

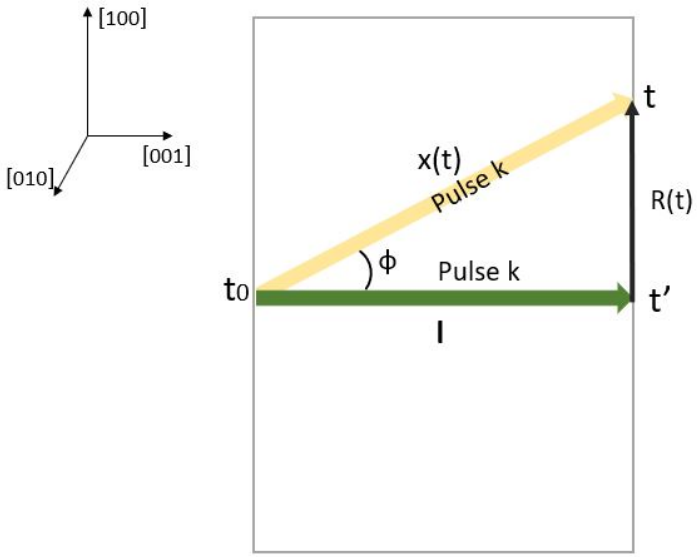

Figure 2.19: Schematics for the geometrical derivation of the form function describing the variation of acoustic wave's radius with time.

2.5 Computational methods

Picosecond acoustics experiment provides the travel times from temporal data and the radii of the acoustic waves as a function of time from the imaging data. Two software are used for the direct problem (simulate picosecond acoustic signal for samples of known elasticity and dimensions) and for the inverse program (derive elastic properties from measured picosecond acoustic signal).

2.5.1 Direct program

The direct program was developed within the group before this internship. This program is based on the Christoffel equation and performs a simulation of the "direct problem": given the elastic constants, it derives the travel times of longitudinal and transverse waves, including the echos. It requires as input the sample thickness, the density, the symmetry class and orientation of the crystal. The program is also useful to visualize the shape and the type (longitudinal or transverse) of the acoustic waves in samples. Figure 2.20 shows the user interface and Figure 2.21 the outcome of the simulation for the example case of Ru.

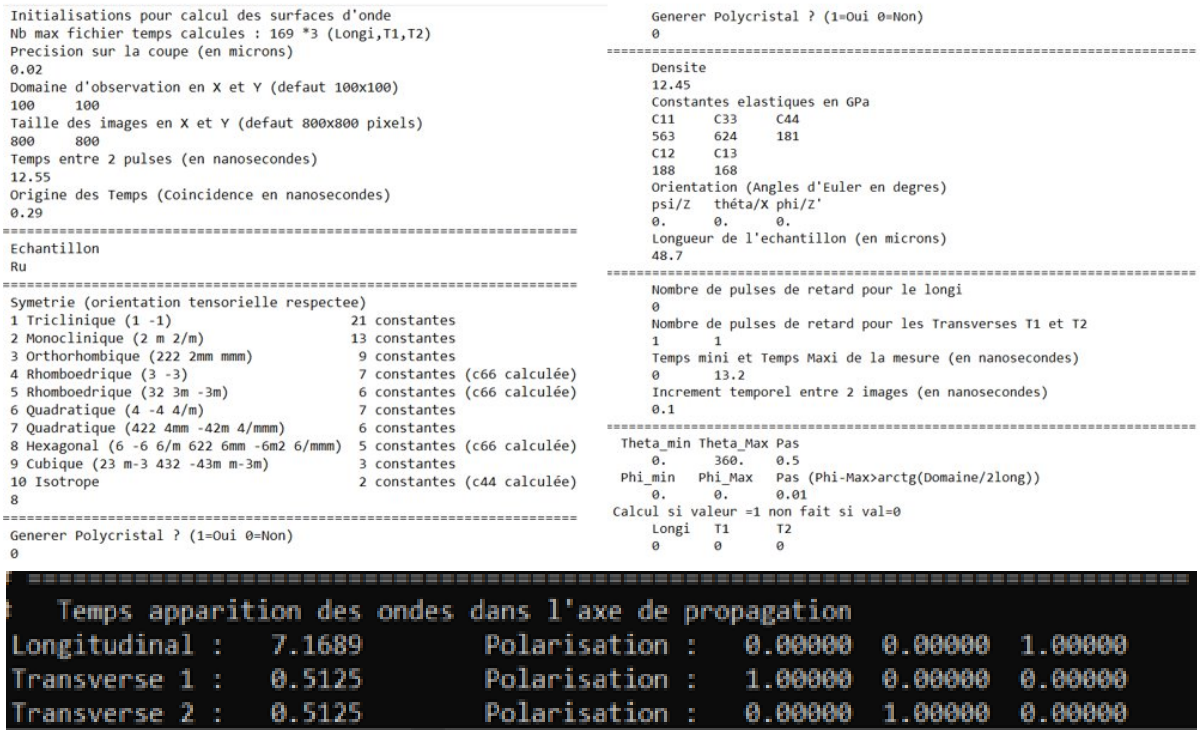

Figure 2.20: Top images: user interface from which is possible to choose the symmetry of the material that is going to be simulated, if it is a polycrystal (random orientation) or not. After the user has to insert the elastic constants and the density. Bottom image: .exe user interface showing the expected arrival times of longitudinal and transverse waves for the sample given its thickness.

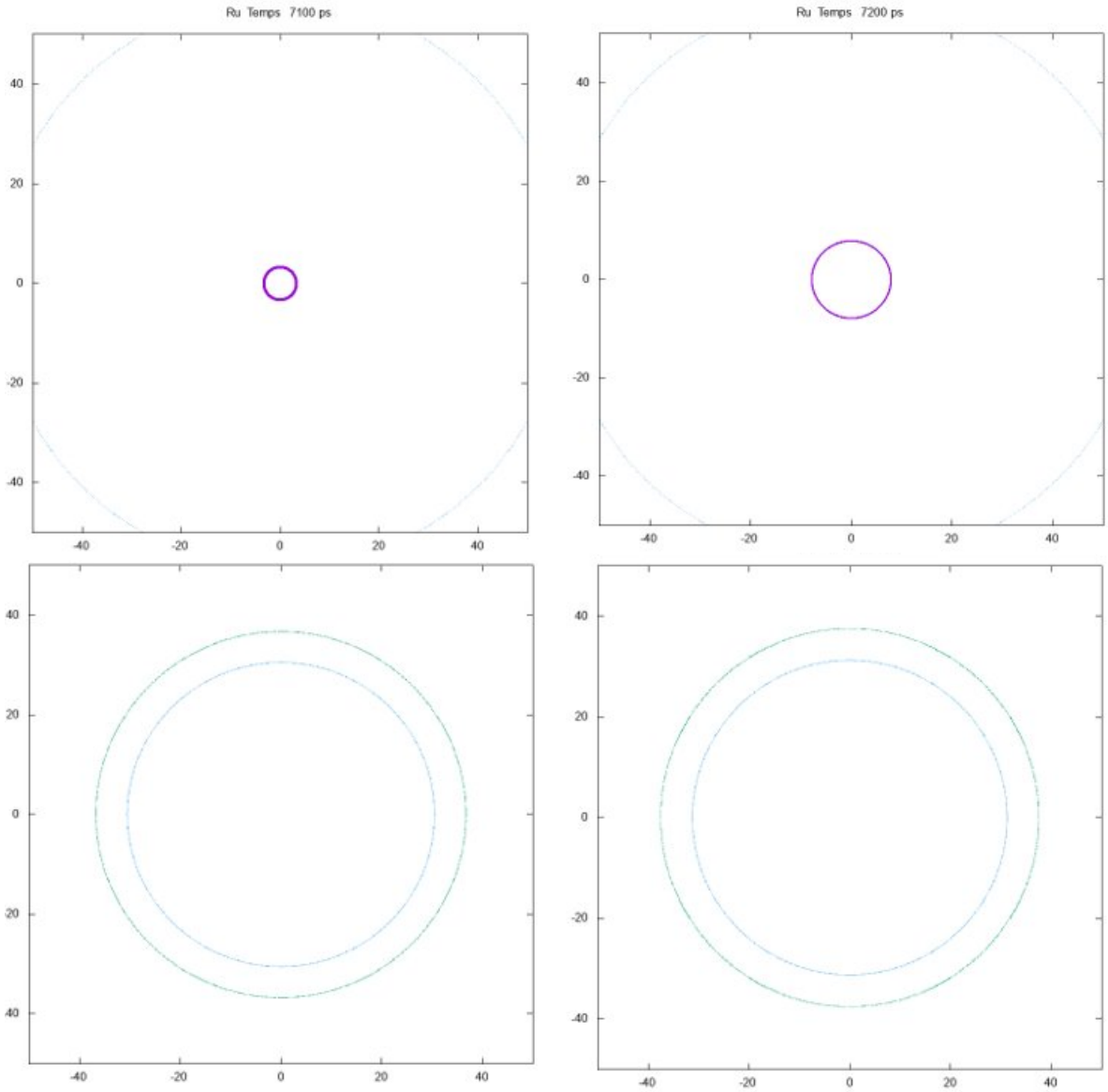

Figure 2.21: Top images: simulation through the direct program of longitudinal wave at given times in 48 μm thick Ruthenium single crystal oriented along (001). Bottom images: simulation of transverse waves in same sample.

2.5.2 Inversion program

The inversion program is another software, developed within group before this internship, which allows the extraction of the elastic constants from collected longitudinal and transverse waves. It consists basically in the inversion of Christoffel equation. As already seen in Chapter 1, this equation provides the link between the sound velocities and the elastic tensor. By inverting the equation, the elastic constants can be derived if sound velocities are known. Since for arbitrary directions not always an analytical solution to the equation exists, the program exploits iterative methods to solve it numerically.
The general idea consists of minimizing the difference between values of experimental sound velocities v^n_{exp} and the theoretical ones, v^n_{theo}, obtained from the elastic moduli. The theoretical values of sound velocities (corresponding at the same delay pump-probe used in the experiment) are calculated by simulation [31], starting from initial guess of values of C_{ij} and progressively refined. Two different iteration methods have been exploited: least square methods (LSM) and a Monte Carlo Method. The inversion program will search for the solutions which minimize the χ^2 of experimental and theoretical sound

velocities, as:

$$\chi^2 = \sum_{n=1}^{n=N} \frac{v_{theo}^n - v_{exp}^n}{\sigma_n^2} \tag{2.13}$$

in which σ_n is the error on the velocity measurements. It requires as inputs the radii of the acoustic waves as a function of time that are extracted with a LabView program as it will be explained in the next Chapter. Figure 2.22 shows the user interface: on the left the user decides whether refining the sample's thickness or the elastic constants writing the number 1, or not refining, writing the number 0; on the right image, the user inserts the type of the wave, the number of the generating laser pulse and the acoustic waves' radii as a function of time.

```
Systeme Cubique

MgO
================================================

Densite
3.58398
0
Longueur de l'échantillon (en microns)
109.38
0
Constantes elastiques en GPa
  C11    C12     C44
297.7   95.3    154.5
1       1       1
```

```
..
#       Points experimentaux a ajuster
#
#       type 0 = longi [100]    (théta =0)
#       type 1 = trans [100]    (théta =0)
#       type 2 = longi [110]    (théta =45)
#       type 3 = trans [110]    (théta =45)
#
#type   NbPulse temps   rayon   erreur
3       1       4.400   -5.334  0.327
1       1       4.400   -10.611 0.058
```

Figure 2.22: User interface of the inversion program in the case of MgO. '0' indicates to the program to not refine that parameter while '1' to refine it.

Chapter 3

Results and discussion

In this Chapter the main results obtained during this thesis are presented and discussed.

3.1 Measurements on MgO

Two pre-oriented single-crystals of MgO (001)[1](Optowise), with a nominal thickness of (100 $\pm$ 20) μm, were investigated at ambient conditions. An Al coating layer was deposited on MgO surfaces to guarantee the generation of acoustic waves, as the penetration depth δ_P is equal to :

$$\delta_{PMgO} = \frac{1}{0.00025\ nm} = 4\ \times 10^{12}\ m \tag{3.1}$$

Thus, δ_P, is much bigger than 20 nm, that is the maximum value of the penetration depth for the acoustic waves' generation.
Indeed, MgO is transparent not only in the visible range, but as well in the near infrared. One of the two samples (MgO/Al) was coated only on one side, while the other one (Al/MgO/Al) was coated on both sides. Acoustic measurements on the two samples are presented and discussed in the following paragraphs.

3.1.1 MgO/Al

This configuration allows to detect Brillouin oscillations of MgO, given by the interference between the probe beam and the propagating acoustic wave. Probe and pump beams were focused respectively on MgO/Al interface and Al/air interface, as shown in Figure 3.1.

[1]In cubic symmetry crystal the directions [100], [010] and [001] are equivalent. In picosecond acoustics set-up the z direction is conventionally assumed along the laser path, and so we will refer to MgO oriented along one of these axis as MgO (001).

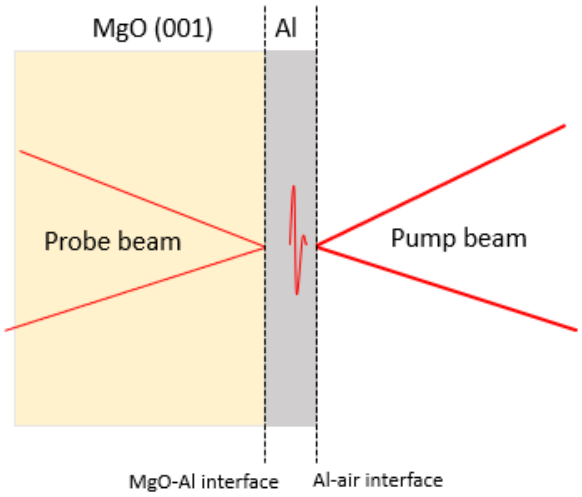

Figure 3.1: Configuration of MgO (001) coated with aluminum only at pump side surface.

Figure 3.2 shows the signal intensity as a function of pump-probe delay time acquired in temporal mode and reflectometry configuration of the picosecond acoustics set-up (see section 2.1.4 in Chapter 2). The signal can be seen as made up of two main contributions: the sharp intensity variation corresponding to the arrivals of sound wave propagating across aluminum, modulated by oscillations at constant frequency (the Brillouin signal of MgO). MgO's longitudinal sound velocity along [001] direction of propagation, $V_{L[001]}$, can be derived from Brillouin oscillations' frequency, ν, as :

$$V_{L[001]} = \frac{\nu\lambda}{2n(\lambda)} \tag{3.2}$$

where $\lambda = 800\ nm$ is the laser wavelength and $n = 1.7272$ is real part of MgO's refractive index.

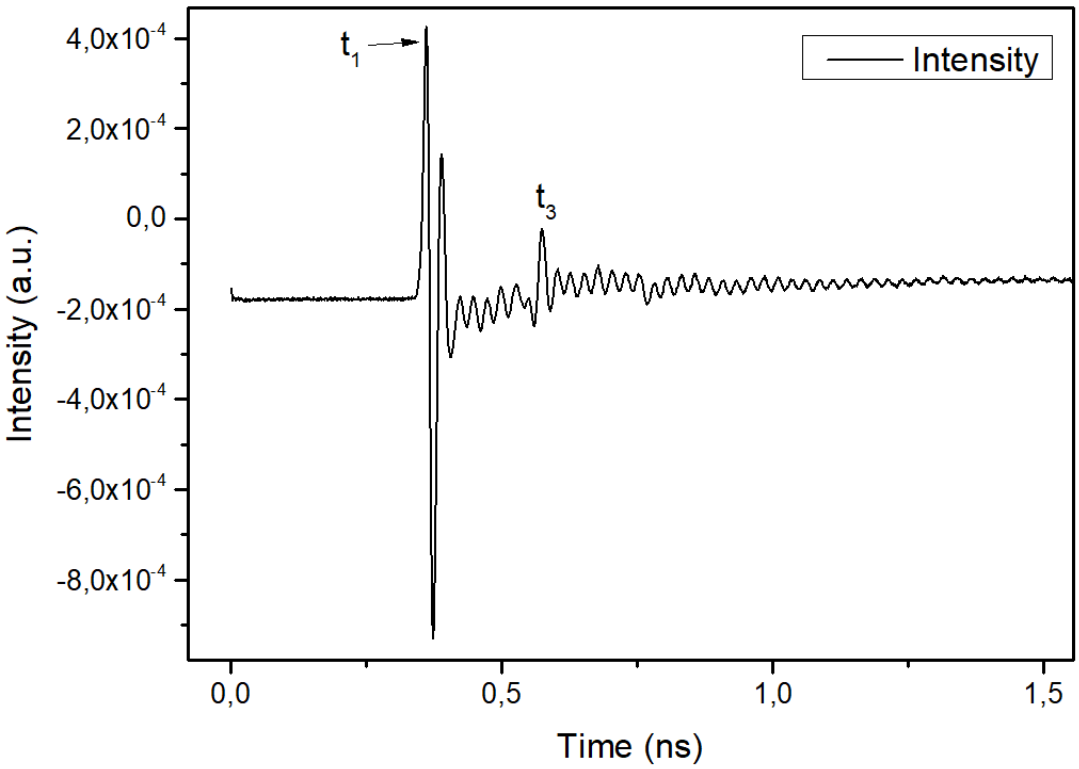

Figure 3.2: Intensity as a function of delay time in MgO (001) single crystal (2mm x 2mm and 100 μm thick). The signal is composed by the arrival acoustic waves propagating in aluminum layer modulated by Brillouin oscillations resulting from the interference between the propagating acoustic echo in MgO and the probe. Oscillation frequency depends on sound velocity and refractive index of the investigated material.

Figure 3.3 shows the signal intensity as a function of delay time after the subtraction of background baseline. This last was determined using the following code, executed in Origin Lab script window :

```
HalfPeriod=15;

 loop(i,1,2004) {

sig=col(Intensity)[i];

sig1=col(Intensity)[i-Halfperiod];

sig2=col(Intensity)[i+HalfPeriod];

col(Base)[i]=(sig+(sig1+sig2)/2)/2;

col(Signal)[i]=(sig-(sig1+sig2)/2)/2;}
```

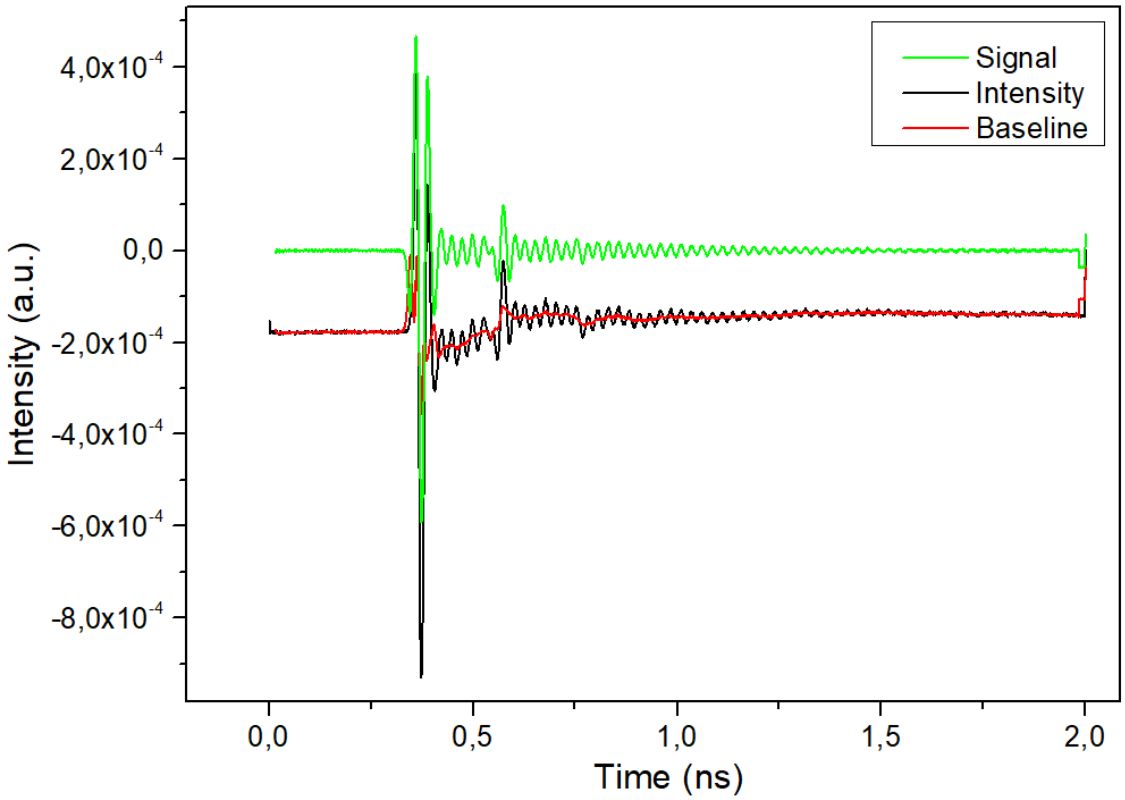

Figure 3.3: Background subtraction in Intensity versus Time temporal measurement on single coated MgO (001) single crystal.

The intensity of Brillouin oscillations shows a decrease at higher pump-probe time delay, caused by the acoustic attenuation of the sample. The data can be fit through a function Y having the form of a sinusoid modulated by a decaying exponential with decay constant 1/d, illustrated by Figure 3.4, as:

$$Y = Ae^{-t/d}sin(\nu t - b)$$

where A is the amplitude, ν the oscillations frequency, b the phase shift and d is related to the acoustic attenuation of the sample.

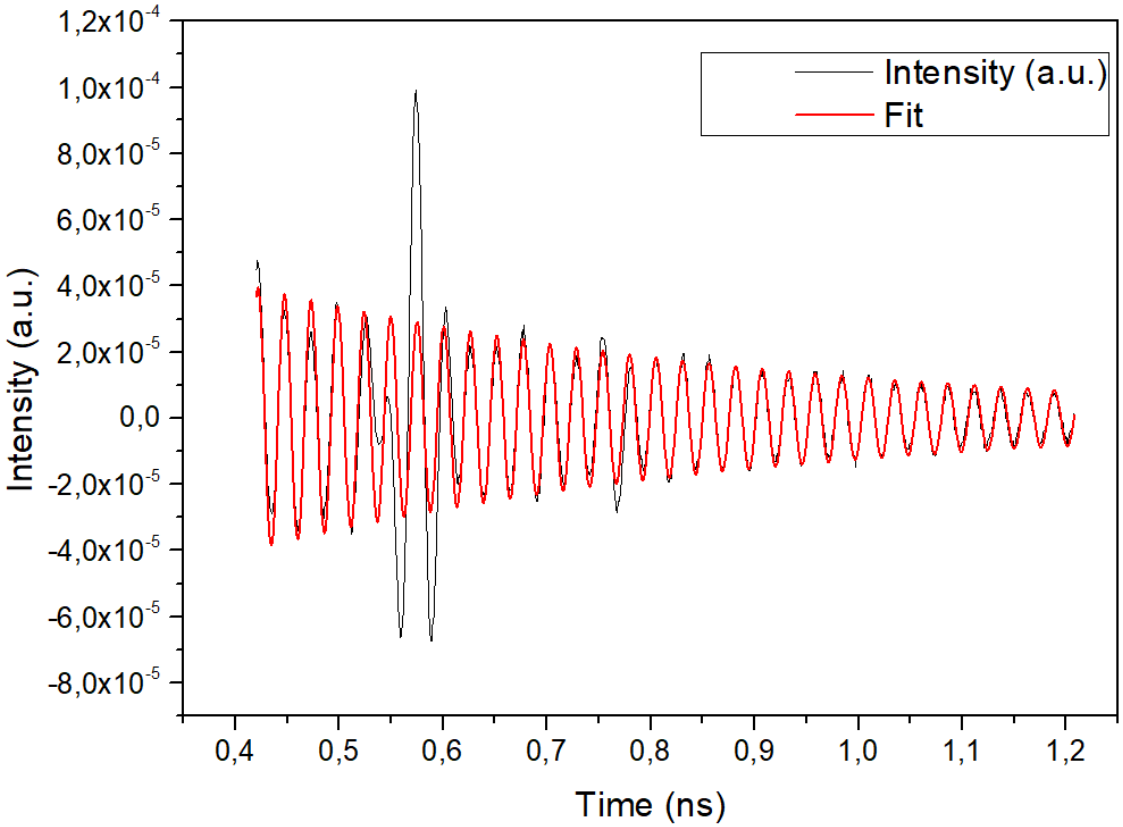

Figure 3.4: Intensity of Brillouin oscillations as a function of pump-probe time delay fit to a damped sinusoidal function Y of the form $Y = Ae^{-t/d}sin(\nu t - b)$.

The Brillouin oscillations' frequency, ν, extracted from the full-range fit is equal to $(245.9 \pm 0.2)\ GHz$. Substituting the ν value obtained from the fit, in Equation 3.2, the velocity $V_{L[100]}$ can be derived, resulting in:

$$V_{L[001]} = \frac{245.9\ GHz \times 800\ nm}{2 \times 1.7272 \times 2\pi} = (9.06 \pm\ 0.07)\ km/s$$

where the uncertainty is calculated considering only the uncertainty on the frequency ν as the other terms' uncertainties are negligible.
The homogeneity of the sample along its thickness can be tested by comparing the frequencies extracted from the fits performed over four different delay time ranges, as illustrated in Figure 3.5. The selected ranges are chosen in order to avoid the echoes due to the propagation of the acoustic wave in the Al coating layer, which carry no information about the MgO. The measured signal varies with time because the relative phase of the light scattered by the acoustic phonons and reflected by interfaces continuously changes with time due to the variation in the spatial position of the acoustic phonons. If the acoustic phonons propagate at a constant velocity in a spatially homogeneous medium, the phase difference between the interfering light fields changes linearly in time causing sinusoidal variations in the signal amplitude at a frequency precisely equal to the Brillouin frequency [37]. The frequencies associated to the selected delay time ranges, listed in Table 3.1, are within mutual uncertainties, indicating a sample's homogeneity.

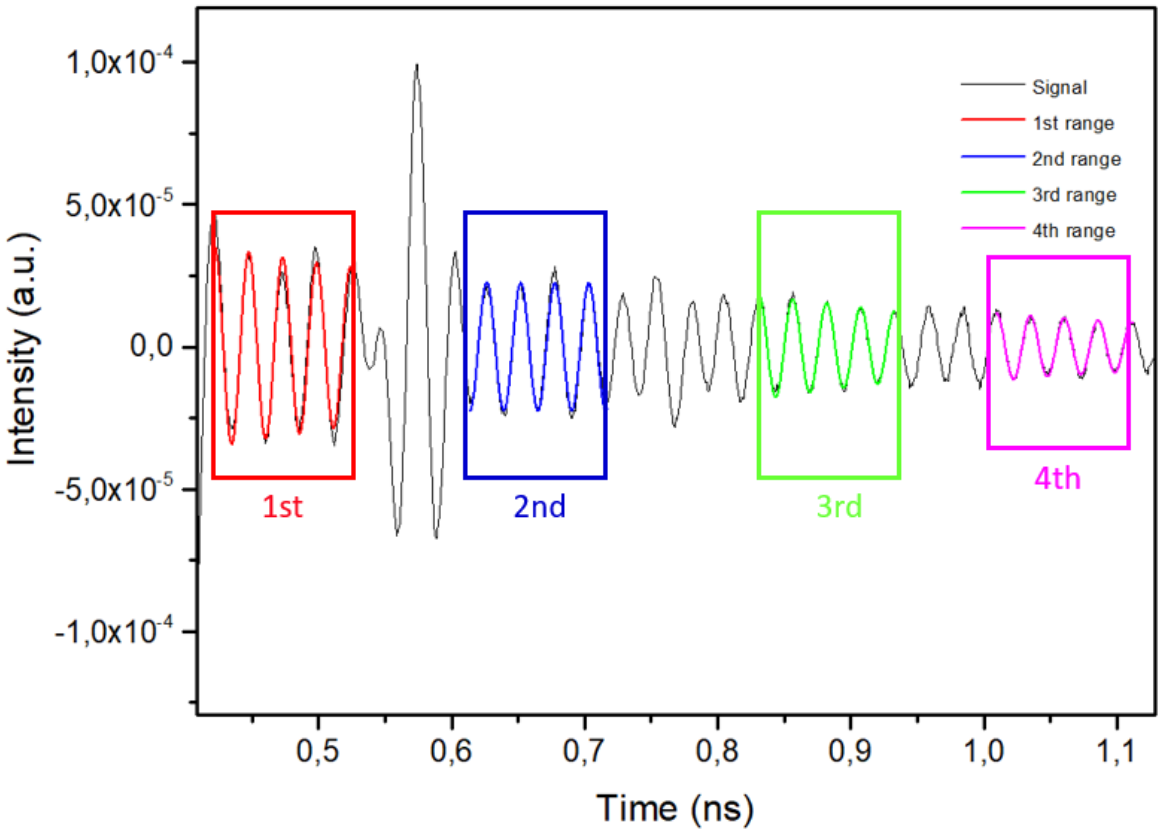

Figure 3.5: Intensity of Brillouin oscillations as a function of pump-probe time delay fit to the function $Y = Ae^{-t/d}sin(\nu t - b)$ in four different time ranges.

Table 3.1 summarizes the frequencies derived from the fits and the relative longitudinal sound velocities in direction [001], $V_{[001]}$, in the four selected ranges. The velocities have been derived from Equation 3.2.

Time range	ν (GHz)	$V_{L[100]}$ (km/s)
1st range [0.42 ns-0.52ns]	246.4 ± 0.9	9.08 ±0.03
2nd range [0.61 ns-0.76ns]	246.4 ± 0.8	9.08 ±0.03
3rd range [0.77 ns-0.90ns]	246.0 ± 0.7	9.07 ±0.03
4th range [0.92 ns-1.12 ns]	247.2 ± 1.5	9.11 ±0.06

Table 3.1: Oscillation frequencies and derived sound velocities for each selected range. The uncertainties on the frequencies directly come from the fit, while for the velocities, errors' propagation rule was used.

The frequencies' mean value $\bar{\nu} = (246.5 \pm 0.5)\ GHz$ (with statistical uncertainty at one σ) is compatible with the frequency of full-range fit, $\nu = (245.9 \pm 0.2)\ GHz$. The value of the acoustic wave velocity in the [001] direction was assumed as the average of the velocity values obtained in the four selected time ranges and the uncertainty as the standard deviation, resulting:

$$\bar{V}_{L[100]} = (9.09 \pm 0.02)\ km/s \tag{3.3}$$

This value agrees within the uncertainties with the acoustic wave velocity evaluated with the formula in Table 1.1, using C_{11} provided from Brillouin spectroscopy measurements by [23]:

$$V_{L[001]} = \sqrt{\frac{C_{11}}{\rho}} = \sqrt{\frac{297.7\ GPa}{3.584\ kg/cm^3}} = 9.11\ km/s$$

Ideally, the thickness of the coating should not be more than 200 nm so that the acoustic signal does not overlap with MgO signal. However, the physical vapor deposition machine (PVD) used to coat the MgO sample in this set of measurements, has a sensitivity of 1 μm, making it very difficult, if not impossible, to provide an homogeneous coating with the thickness thinner than the sensitivity. The obtained coated layer was thus thicker than expected, allowing the detection of the acoustic waves propagating across it. The two peaks in Figure 3.2, t_1 and t_3, are the arrival times of the acoustic waves that propagate inside the coated layer of Al. The first arrival of the acoustic wave is detected at $t_1 = 0.373\ ns$ and corresponds to the arrival of the acoustic waves at MgO/Al interface; the echo $t_3 = 0.574\ ns$ relates to the acoustic wave reflected by MgO/Al and Al/air interfaces and detected by the probe beam at MgO/Al interface after these reflections. This peak is less intense than the one at t_1 because of the acoustic attenuation inside the sample and because of the transmission/reflection processes occurring at the interfaces. The Al layer's thickness, l, can then be estimated from the measured travel time, $\Delta t = t_3 - t_1$, using as input the compressional sound velocity of Al [38], as follows:

$$l = \frac{V_{Al} \times \Delta t}{2} = \frac{6.40\ km/s \times 0.201\ ns}{2} = 643\ nm$$

3.1.2 Al/MgO/Al

A second MgO sample was coated on both surfaces as illustrated in Figure 3.6. This time, an evaporation deposition machine, having the precision of tens of nm, was used. Coating thicknesses were 200 nm at pump side and 100 nm at probe side, measured by optical profilometry. In this configuration the probe beam is focused on Al as is the pump beam: the acoustic waves generated at pump surface propagate inside MgO and are detected at probe side.

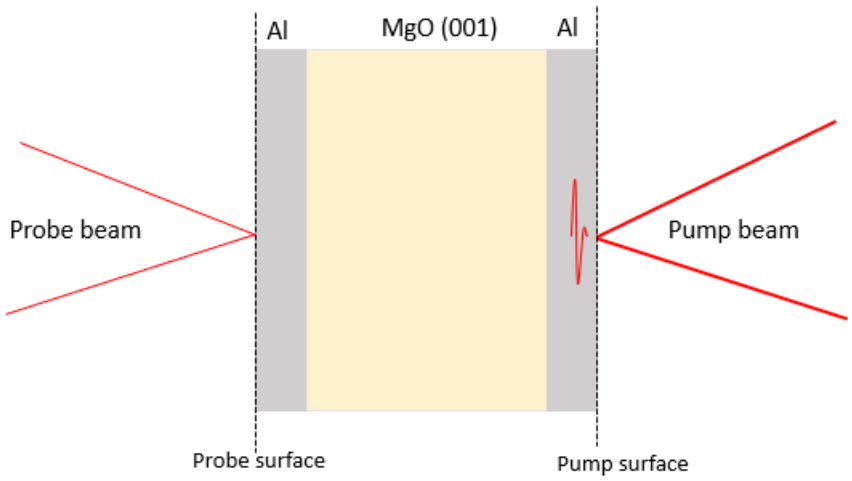

Figure 3.6: Second MgO sample with two surfaces coated with Al: pump side coating is 200 nm and probe side coating is 100 nm.

Figure 3.7 shows the signal intensity as a function of pump-probe time delay acquired in temporal mode and reflectometry configuration. The arrival time of the longitudinal wave is detected at t_{Longi}= 12.398 ns.
The MgO's nominal thickness was given with an uncertainty of 20 % that would propagate with an uncertainty of at least 20% on the sound velocity's uncertainty. Thus, MgO thickness, l, can be derived from the travel time that are measured with a much smaller uncertainty, as follows:

$$l = V_{L[001]} \times \Delta t \quad \text{with} \quad \Delta t = t_1 - t_0 \tag{3.4}$$

where $V_{L[001]}$ is the MgO longitudinal sound velocity in the direction [001] (as for instance obtained by analysis of the Brillouin oscillation, see previous section), t_1 is the arrival time of the longitudinal wave measured on probe surface and t_0 is the time of acoustic signal generation, at the pump side. Thus,

$$l = 9.09\ km/s \times 12.09\ ns = (109.9 \pm 0.2)\ \mu m$$

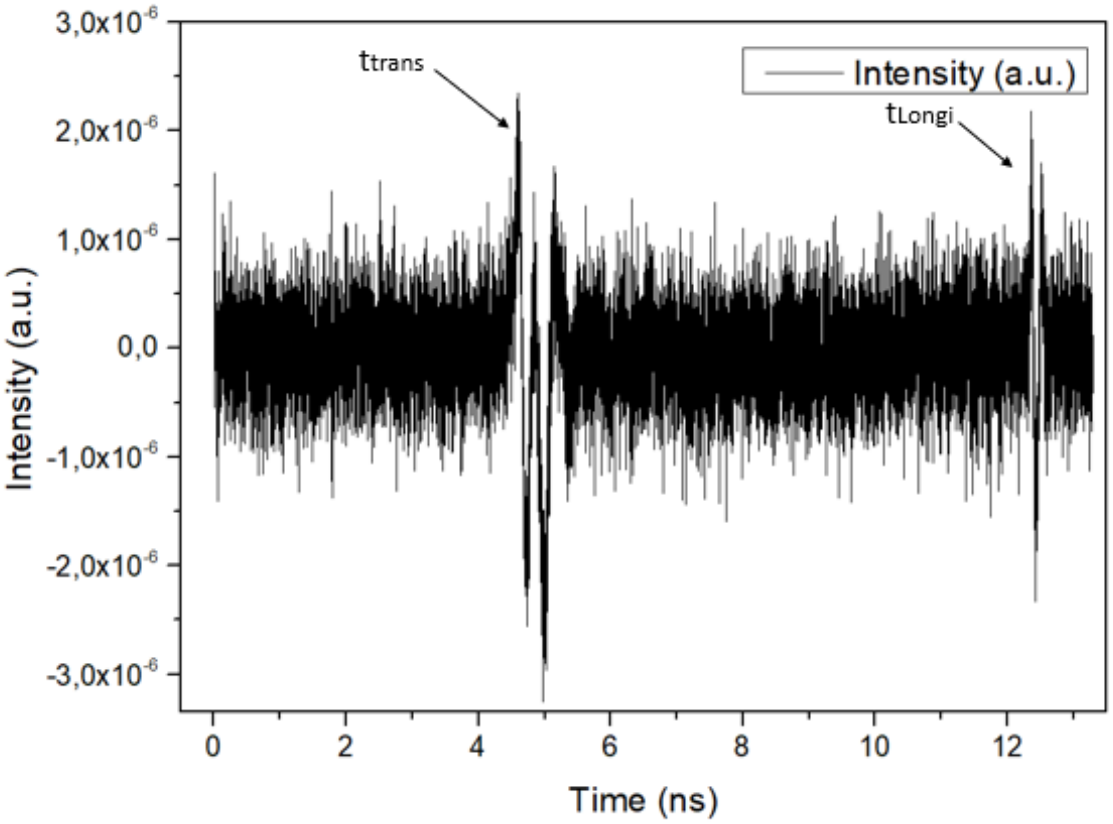

Figure 3.7: Intensity as a function of pump-probe time delay plot acquired in temporal mode and reflectometry configuration for the Al/MgO/Al sample. The peak at t_{Longi} is the arrival time of longitudinal acoustic wave of velocity, $V_{[001]}$, while the peak at t_{trans} is the time when the transverse wave, that arrived at sample surface somewhere else, reaches the focus sample spot of the probe beam.

The t_{trans} visible in the temporal mode measurement shown in Figure 3.7 corresponds to the arrival of the transverse acoustic wave at the point where the probe beam is focused. From the direct program simulation and from the imaging data, we know that this time is not the arrival time of the transverse acoustic wave at the opposite MgO sample surface and cannot be used to derive the transverse wave sound velocity.
More information can be obtained from phonon imaging, exploiting the imaging data

collection mode. As described in section 2.5.2, an inversion program can be used to derive the elastic constants and the thickness of the sample using as inputs the acoustic waves' arrival times, the type of wave (longitudinal or transverse) and the acoustic waves' "radii" as a function of time. In this context the term radius is used for both isotropic and anisotropic materials to indicate, respectively, the standard radius of a circle or the distance between the intersection point with the high-symmetry axes and the center (i.e. position corresponding to straight propagation of the acoustic wave generated on the other side of the sample). Radii are obtained from the imaging mode data using a LabView program, as illustrated in Figure 3.8. The yellow axes corresponds to the direction [100] and the red axes to the direction [110]. Information about the character of the wave and distinct shape can be confirmed by comparison with direct program's simulations. The refined elastic constants are obtained from the inversion program. The bulk and the shear moduli, are derived through Voigt-Reuss-Hill rule and the acoustic waves velocities are obtained from Equation 1.21 in section 1.3.2.

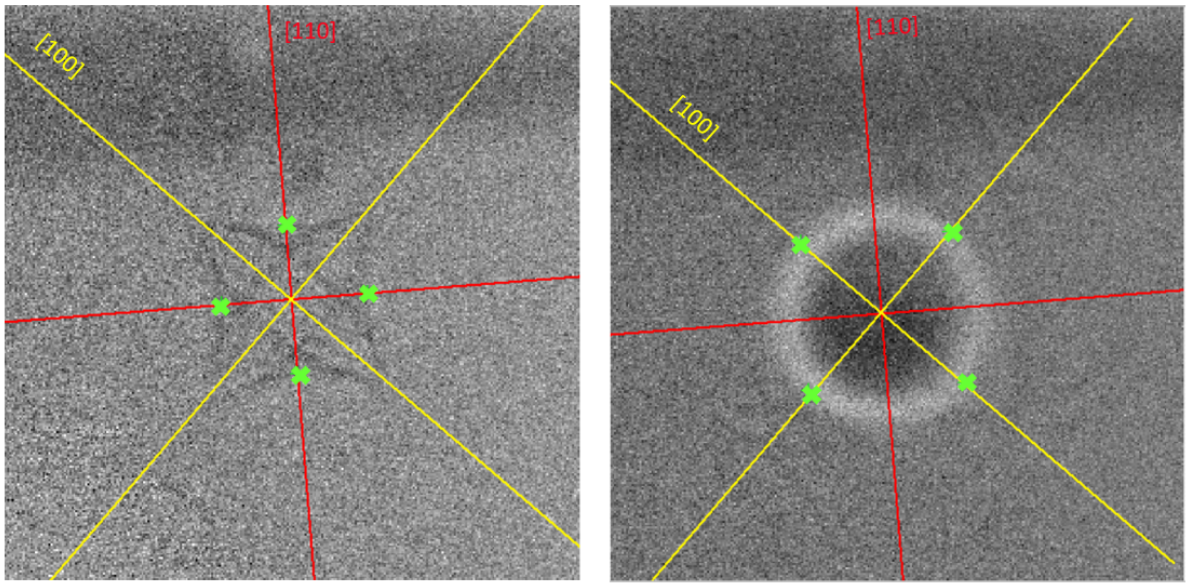

Figure 3.8: 100 $\mu m \times 100\ \mu m$ images showing the transverse (left) and longitudinal (right) waves in MgO, detected respectively at 5.3 ns and at 12.4 ns. The yellow axes show the direction [100], while the red axes show the the direction [110]. The LabView program determines the distance, i.e. the acoustic waves' radius, between the intersection points of the propagating acoustic waves with the high-symmetry axes and the center of the acoustic wave, providing the input for the inversion program.

Figure 3.9 shows the reference system used for the experiment: the acoustic waves at probe side surface are visible on the plane given by the directions [100] and [010].

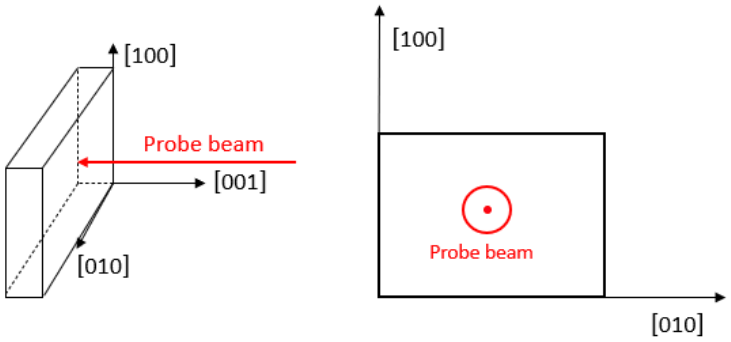

Figure 3.9: Reference system exploited for the experiment is schematically presented. The acoustic waves are visible on the plane given by the direction [100] and [010].

Figure 3.10 shows the radius of the acoustic waves, for both longitudinal or transverse waves in directions [100] and [110] as a function of time. These are used as inputs for the inversion program. From the figure we see that there are values of the radii as a function of time at instants between 0 and 1 ns and after 12 ns. From the simulation through the direct program it emerged that the arrival time of the longitudinal wave generated by the laser for 0 delay pulses is 12.38 ns. Considering the repetition rate of the laser, $T = 12.55\ ns$, and the arrival time of the simulated longitudinal wave at $t_1 = 12.38\ ns$, the acoustic waves visible in the time range between 0 and 1 ns correspond to the longitudinal acoustic waves generated by the previous laser pulse ($k = -1$). In fact, $t_{-1} = 12.38\ ns - 1 \times (12.55\ ns) = -0.17 ns$. Noteworthy, as both longitudinal and transverse waves are bulk waves, the variation of their radii as a function of time follows the relation 2.12 presented in section 2.4.2, (see Figure 3.10).

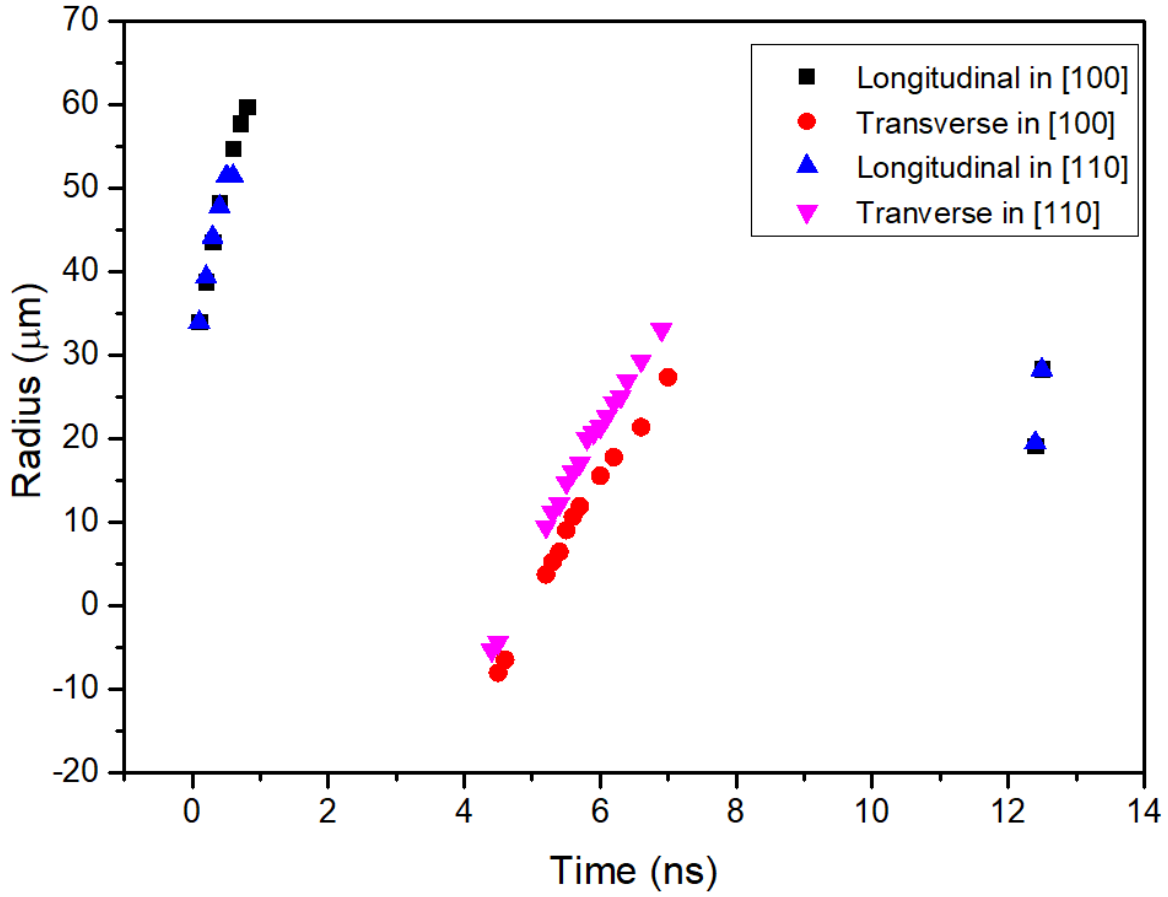

Figure 3.10: Radius as a function of time, for longitudinal and transverse waves in Al/MgO/Al along directions [100] and [110]. These observations are the inputs for the inversion program. Radii of longitudinal waves propagating along [100] and [110] direction overlaps as a consequence of crystal symmetry.

The independent elements of the elastic tensor C_{ij} resulting from the inversion are reported in Table 3.2 together with literature values from Brillouin spectroscopy measurements [23]. The redundancy of the probed directions in present measurements (2D images) with respect to single direction determination by classic Brillouin spectroscopy [23] directly reflects in the smaller uncertainties of our determinations.

	l (μm)	C_{11} (GPa)	C_{44} (GPa)	C_{12} (GPa)
This work	109.38 ± 0.04	296.96 ± 0.19	153.60 ± 0.10	98.78 ± 0.11
Sinogeikin et al.	–	297.7 ± 3	154.5 ± 1.5	95 ± 1

Table 3.2: Elastic constants of MgO obtained in this work compared to literature values [23].

The refined thickness $l = (109.38 \pm 0.04)\ \mu m$ is compatible with the one derived from travel times in the previous section.
The estimated values of the aggregate bulk and shear moduli, as well as aggregate compressional and shear velocities according to Equation 1.21 are listed in Table 3.3.

	K (Gpa)	G (Gpa)	V_P km/s	V_S km/s
This work	164.8 ± 0.1	131.33 ± 0.05	9.692 ± 0.002	5.996 ± 0.003
Sinogeikin et al.	162.767	130.398	9.691 ± 0.03	6.032 ± 0.03

Table 3.3: Bulk and shear moduli, compressional and shear velocities of MgO.

The longitudinal acoustic wave's velocity in direction [001] can be recalculated using the refined C_{11}:

$$V_{L[001]} = \sqrt{\frac{296.96\ GPa}{3.5839\ g/cm^3}} = (9.10 \pm 0.05)\ km/s$$

where the uncertainty is estimated propagating uncertainty on C_{11}.
This value is in good agreement with the one derived through Brillouin oscillations in the previous section and in good agreement with the literature.

3.2 Discussion on MgO measurements

3.2.1 MgO/Al

Picosecond acoustics measurements on MgO/Al sample allowed to extract the Brillouin oscillations frequency and the longitudinal sound velocity in direction [001], $V_{L[001]}$. The obtained value agrees within uncertainty with the literature. However, the aluminum coating was too thick (643 nm) due to the limited performances of the used PVD machine. For this reason, the acoustic waves propagating inside aluminum were also detected. While this was not a problem of the detection and analysis of the MgO Brillouin signal, this should be avoided because of potential overlap of the acoustic waves propagating within the sample and within the coating. As demonstrated in the case of MgO/Al, the sample homogeneity along its thickness can be evaluated selecting specific time ranges out from the whole probed delay time range and comparing the extracted frequencies from each interval. Tests on the homogeneity are essential when natural samples are studied, because they can present inhomogeneities. Similarly, quality of synthetic samples can be probed to discriminate on synthesis protocols. While not done in this work, to test the sample homogeneity over the other directions, the same measurements changing the focus spot position should be performed. To conclude, the developed experimental protocol can be extended to the study of all the transparent materials once their refractive index is know and changing the coating coupler if the acoustic mismatch with Al is too high.

3.2.2 Al/MgO/Al

In the Al/MgO/Al specimen the acoustic waves propagating within the sample were generated on one side of the sample and their arrival detected on the opposite side. This time the coating was deposited using the evaporation deposition machine that guarantees a precision of tens of nm, so effectively producing layers of desired thickness. However, due to an internal malfunctioning, the deposited coating resulted to be not homogeneous over the entire surface. Even if we could not generate an acoustic signal everywhere on the surface of the sample, we managed in finding a spot in which it was possible. Focusing on this spot, the data were successfully acquired and the full elastic tensor C_{ij} at ambient pressure was derived from the inversion program. Obtained results are in agreement with literature values [23]. In particular, we stress that the very high number of directions simultaneously probed by the imaging, allowed for inversion of the elastic moduli with a much higher precision than inversion from Brillouin measurements performed for one direction at the time, and consequently along a much reduced number of directions. From the elastic tensor the bulk and the shear moduli were derived by classic averaging schemes, and from them the compressional and shear velocities were also determined.
The here developed protocol involving the use of picosecond acoustics technique and of the inversion program were successfully tested to provide the material's elastic tensor at ambient pressure. However, these measurements allowed to evidence the importance of the quality and homogeneity of the coating. Accordingly, the next set of measurements

on MgO should be performed on samples with a more homogeneous and thinner coating layer. In order to extend these measurements to high-pressure, the MgO sample thickness should be decrease from 100 μm down to about 40 μm to fit the DAC constraints, while still allowing for the use of the phonon imaging technique.
Finally, some considerations have to be made concerning the selection of the operation mode. The temporal mode only provides the travel times of the acoustic waves, while to derive sound velocity sample's thickness is also necessary. For measurements at ambient pressure the sample thickness can be determined with high precision by interferometry or from travel time determination if the value of the sound velocity is known (either from literature, or, from Brillouin oscillations in case of transparent samples). For high pressure experiments, the procedure is typically different: the sound velocities must be derived from the travel times measurements making use of known equation of state to estimate sample thickness at pressure (this protocol will be used for Ru measurements). As such, pressure derivative of the velocities are derived with higher precision than absolute values. On the other hand, the information extracted from the data collected in imaging mode is more complete and allows to directly determine the thickness of the sample as well as the elastic constants through the inversion program. Imaging mode is thus preferable when possible, but necessitating bigger samples than temporal measurements, is less apt to very high pressures (P$> \sim 50$ GPa).

3.3 Measurements on Ru

The ruthenium sample was a single-crystal with orientation in (0001)[2] plane bought from Princeton Scientific Corporation, and was investigated both at ambient- and high-pressure conditions. The sample was mechanically polished to a thickness of $\sim 50\ \mu m$, as measured by a micrometer. Several disks of 150 μm of diameter were laser-cut out from the big sample to make them suitable for experimentation in the DAC. Ruthenium directly absorbs in infrared wavelength not requiring a coating of the surfaces. In fact, the penetration depth, δ_P, is:

$$\delta_P = \frac{1}{\alpha} = 16\ nm < 20\ nm$$

where 20 nm is the maximum value of penetration depth to generate the acoustic waves. Picosecond acoustic measurements in the imaging collection mode performed on hexagonal samples along the direction [001], allow to only partially obtain the elastic tensor: four independent components out of five (C_{11}, C_{33}, C_{44} and C_{13}). To obtain the missing elastic constant, C_{12}, another orientation is needed, for instance measurements along the direction [010].
The travel times are measured with high precision (order of picosecond). Sample thickness can be inverted from data collected in imaging mode, while it is an independent input for determining sound velocity from data collected in temporal mode. Depending on the precision on the direct instrumental measurement, errors on sample thickness can be of the order of several percent, generally being the largest source of uncertainties for sound velocity determination by temporal measurements. Thus, the most commonly used protocol for sound velocity measurements at high pressure by temporal mode is based on:

1. the precise determination of sample thickness at ambient conditions by using the measured travel time in combination with independent measurements or literature values of sound velocities, and

2. the use of know equation of state to estimate thickness variation at high pressure, to be used together with direct travel time determination to derive sound velocity.

3.3.1 Ru at ambient pressure

Measurements at ambient pressure were performed at first on a " big sample" (2mm x 2 mm and about 50 μm thick), then on "small sample" disks (150 μm in diameter and about 50 μm thick). In both cases, the sample thickness was derived with precision from the arrival times by analysing the temporal data and from the inversion program.
Figure 3.11 shows the intensity as a function of the pump-probe delay time in the big sample of Ru acquired in temporal mode and in interferometry configuration.

[2]The notation with four indices, [h k i l], where i=-h-k, is usually used for hexagonal symmetry crystals. From now on the simplified notation with three indices, [h k l], will be used.

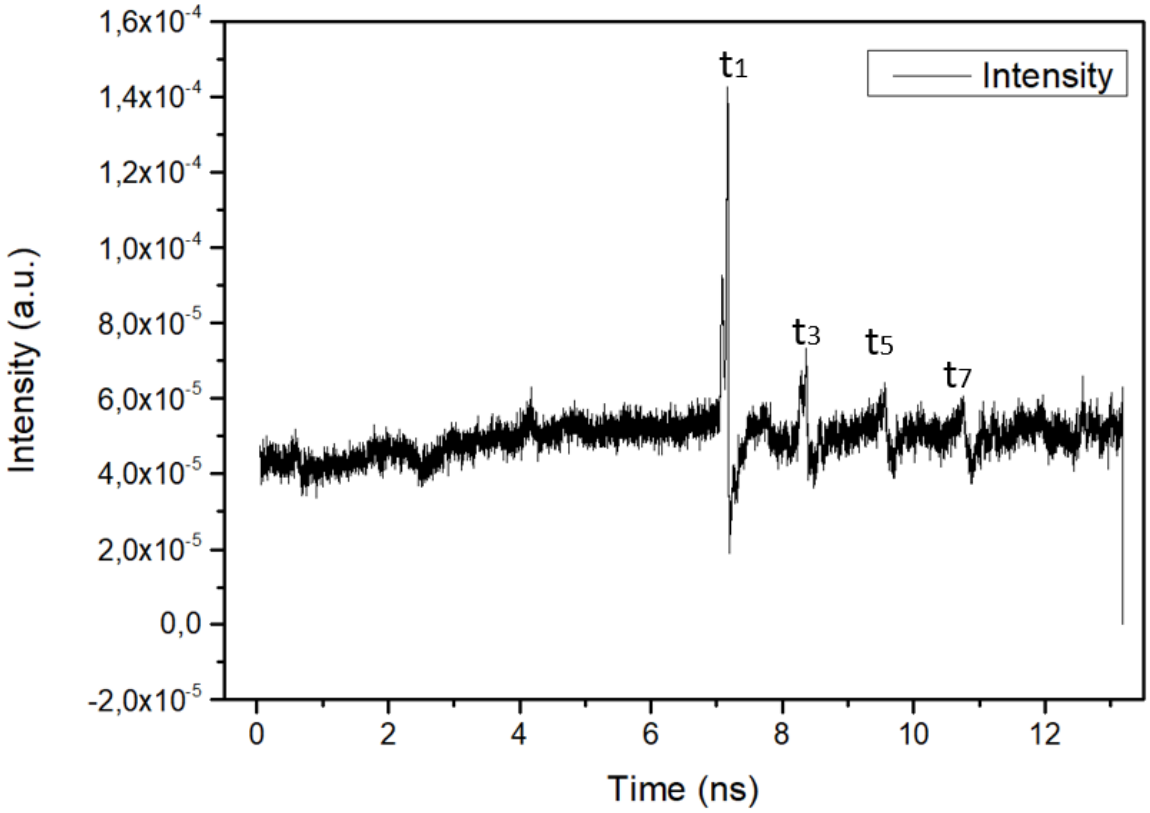

Figure 3.11: Intensity as a function of pump-probe delay time in Ru big sample (2mm x 2mm and about 50 μm thick) along [001] direction.

Due to the visualization of the acoustic waves' arrival times in an unique temporal window (allowed by the periodicity of the laser pulses), as explained in section "Temporal mode" (Chapter 2), it is not known a priori which are the laser pulses, k, that generated the visible signal peaks. Deriving the real time at which the signal was detected is fundamental to calculate the thickness. Aiming at this, each arrival time, t_n, was hypothesized as if generated by the the four previous laser pulses (see Table 3.4). The sample's thickness corresponding to each hypothesis (listed in Table 3.4) was derived from:

$$l = \frac{V_{L[001]} \times t_n}{n} \tag{3.5}$$

where

$$V_{L[001]} = \sqrt{\frac{C_{33}}{\rho}} = \sqrt{\frac{624\ GPa}{12.365\ g/cm^{-3}}} = 7.10\ km/s \tag{3.6}$$

where C_{33} is provided by [29] and ρ by [24][3].
There is only one combination of the arrival time, t_n, and of the number, k, of delay laser pulse for which the sample's thickness is the same, and it is for:

- t_1 generated by k= 0 previous laser pulse;
- t_3 generated by $k = 1$ previous laser pulse;
- t_5 generated by $k = 2$ previous laser pulse;
- t_7 generated by $k = 3$ previous laser pulse.

[3]The density is not explicitly provided by [24], which only reports the unit cell volume, V_a. Thus, density was derived according the relation $\rho = \frac{m_a}{V_a}$ where m_a and V_a are respectively the mass and the volume of the unit cell. The $m_a = (n \times M)/N_a$ where n is the coordination number for hexagonal crystals, M the molar mass and N_a the Avogadro's constant.

k	t_1 (ns)	l (μm)	t_3 (ns)	l (μm)	t_5 (ns)	l (μm)	t_7 (ns)	l (μm)
0	6.872	**48.81782**	8.072	19.11416	9.281	13.18621045	10.497	10.65277
1	19.422	137.9714	20.622	**48.83203**	21.831	31.01693356	23.047	23.389
2	31.972	227.1251	33.172	78.5499	34.381	**48.84765667**	35.597	36.12523
3	44.522	316.2787	45.722	108.2678	46.931	66.67837978	48.147	**48.86146**

Table 3.4: Arrival times of the acoustic waves and the corresponding sample's thicknesses according to different hypothesis concerning the laser pulse k which generated the acoustic waves. Bold characters were used to highlight which $k-th$ laser pulse generated the acoustic wave visible at each arrival time.

The sample's thickness is taken as the mean value of the obtained thicknesses, being:

$$l = (48.84 \pm 0.02)\ \mu m$$

where the standard deviation is assumed as the uncertainty on the sample's thickness. Figure 3.12 shows the signal intensity as a function of pump-probe delay time for the small sample acquired in temporal mode and interferometry configuration.

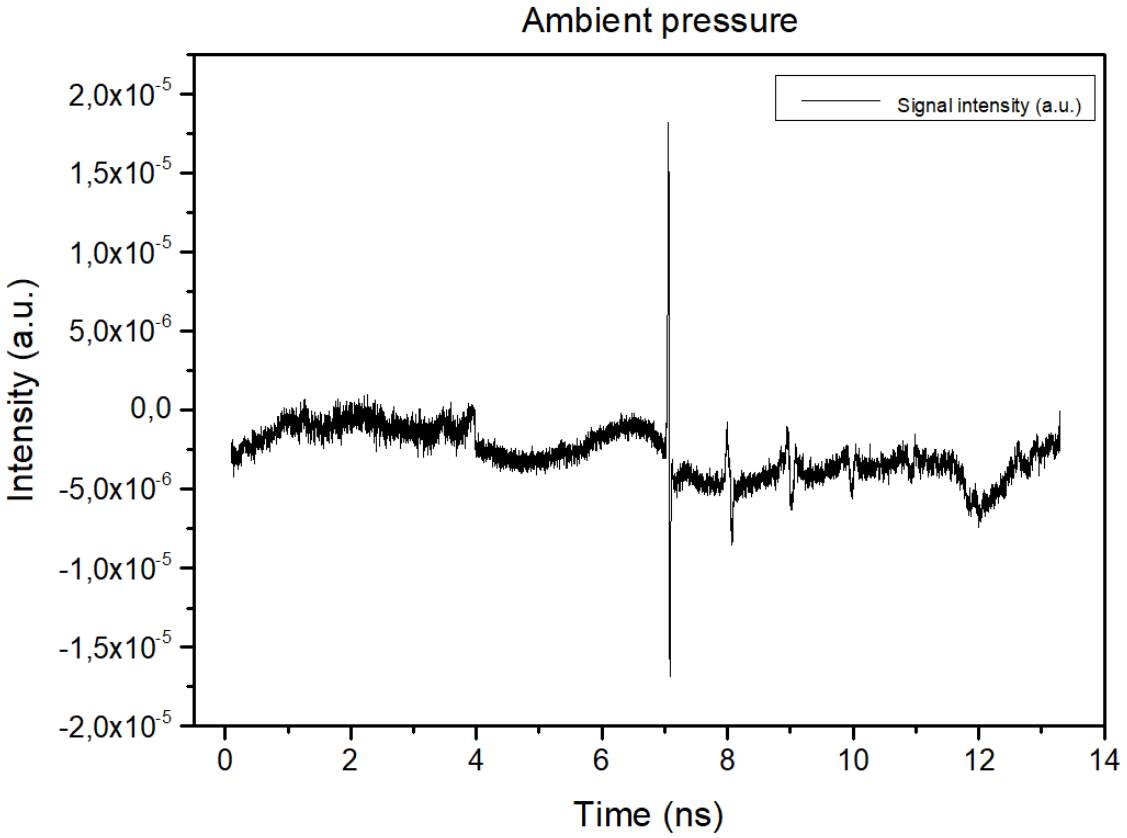

Figure 3.12: Intensity as a function of pump-probe delay time in Ru small sample (disk of 150 μm in diameter and about 50μm thick) oriented along [001] direction.

Following same protocol detailed for the bigger sample, the small's sample thickness, l, is determined to be:

$$l = \ (48.01 \pm 0.02)\ \mu m \tag{3.7}$$

The two thicknesses are slightly different, most likely because of original sample not polished perfectly parallel, resulting in variation in thickness of few microns over a mm distance. As such, disks cut out from different portion of the sample result having slightly different thickness.

The elastic constants of the big sample are derived from the inversion program using as initial inputs the sample's thickness obtained from the analysis of the temporal data and the radii of the acoustic waves as a function of time provided by the LabView program, as illustrated in Figure 3.13. Along direction [001] hexagonal single-crystals (as Ru) are isotropic, and the wave fronts are spherical, as shown in Figure 3.13.

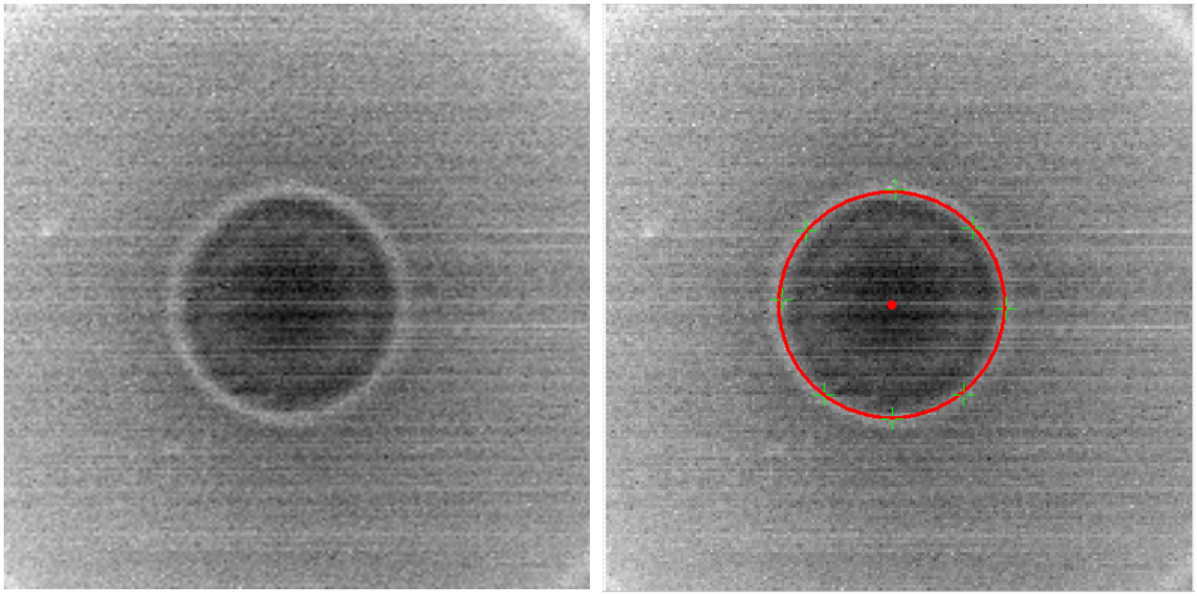

Figure 3.13: 100 $\mu m \times 100$ μm image showing the longitudinal acoustic wave in Ru-single crystal along [001] direction at a delay time of 7.9 ns. LabView program allows to determine the radius of the acoustic wave at a given time.

Figure 3.14 shows the radii of the acoustic waves as a function of time for both the big and the small samples. The form function of the acoustic waves' radii is described in section 2.4.

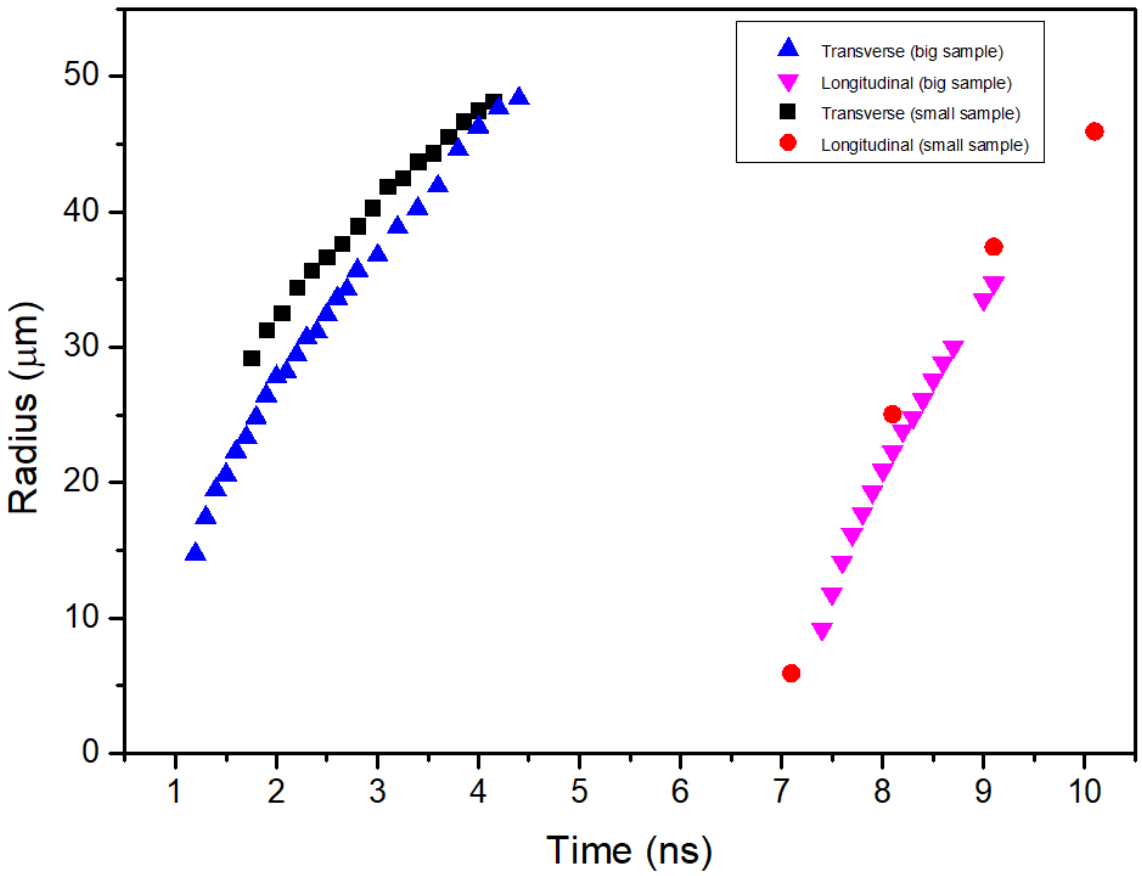

Figure 3.14: Acoustic waves' radii as a function of time for the two investigated samples. They serve as inputs to the inversion program.

Elastic constants provided by Tromans at al. [29] and the density $\rho = 12.365\ g/cm^3$ calculated starting from the volume measured in Anzellini et al. [24] were used as starting values for the inversion of measurements on the big sample. Then, measurements performed on small sample are inverted, using as initial values for the elastic constants the ones obtained as output of inversion for the big sample and as sample's thickness the value obtained from temporal data analysis. The results are summarized in Table 3.5.

Sample	l (μm)	C_{11} (Gpa)	C_{33} (GPa)	C_{44} (GPa)	C_{13} (GPa)
Big sample	49.2 $\pm$ 0.3	560 $\pm$ 5	622 $\pm$ 7	180.5 $\pm$ 0.4	181 $\pm$ 5
Small sample	47.9 $\pm$ 0.3	568 $\pm$ 7	629 $\pm$ 9	183.9 $\pm$ 0.6	169 $\pm$ 8
Mean value	–	564 $\pm$ 6	626 $\pm$ 8	182.2 $\pm$ 0.5	175 $\pm$ 7

Table 3.5: Refined samples' thicknesses and Ru elastic constants. Errors on the mean values are calculated through errors' propagation rules.

Table 3.3 lists the values obtained in this work and the literature values.

	C_{11}(GPa)	C_{33} (GPa)	C_{44} (GPa)	C_{13} (GPa)
This work	564 $\pm$ 6	626 $\pm$ 8	182.2 $\pm$ 0.5	175 $\pm$ 7
Tromans et al.	563	624	181	168

Table 3.6: Elastic constants obtained in this work compared to literature values from Tromans [29].

The elastic constants derived for the big and the small samples are within mutual uncertainties. This good agreement witness the reliability of the inversion scheme, as no differences are expected on the elastic constants, as the experimental conditions did not change. The bulk and shear moduli presented in Table 3.7 were derived using Equations 1.19 and 1.20 and the compressional and shear acoustic wave's velocities from Equation 1.21 (for C_{12} we assumed the value from [29]). They are compatible with the ones provided by Tromans et al. [29], see Table 3.7.

	K_{VRH} (GPa)	G_{VRH} (GPa)	V_P (km/s)	V_S (km/s)
This work	314 $\pm$ 4	190.9 $\pm$ 1.1	6.78 $\pm$ 0.02	3.93 $\pm$ 0.01
Tromans et al.	310.7	191.0	6.75	3.93

Table 3.7: Bulk and shear moduli derived from Voigt-Reuss-Hill average rule and compressional and shear acoustic wave's velocities. Uncertainties are calculated propagating the uncertainties associated to the elastic constant provided by the inversion program.

3.3.2 Ru at high-pressure

High-pressure test measurements on Ru single-crystal were performed inside the diamond anvil cell, up to 10 GPa. Due to technical problems with the gas loading system, it was not possible to use a noble gas as PTM, as more suited for the planned measurements. The selected PTM was then a 4:1 mixture of methanol-ethanol which solidifies at 4.5 GPa and is considered to retain pressure hydrostaticity up to 10.5 GPa [34].
In order to minimize contribution from pump diffusion in the measured signal, (enhanced in DAC measurements by the diffusion due to the presence of diamonds, and more difficult to reject by cross polarization due to depolarization effects of diamonds on laser beam) the probe side diamond was covered with a very thin layer of Tin (less then 1 μm, obtained pressing a small piece of Tin between the two diamonds), as illustrated in Figure 3.15.

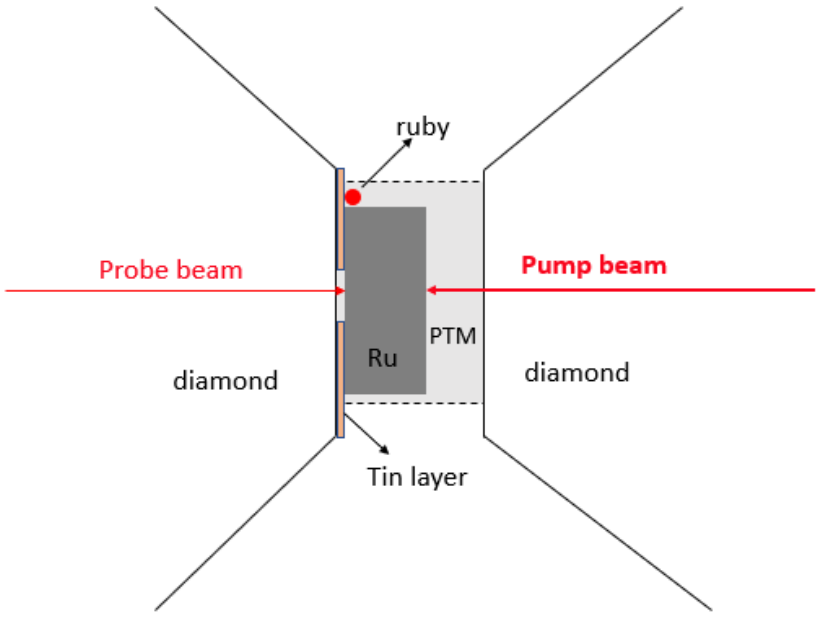

Figure 3.15: Schematics of the used configuration for high pressure measurements in Ru single crystal.

Figure 3.16 shows probe side view of the sample loaded in the DAC deposited with Tin, before compression (left) and after decompression (right).

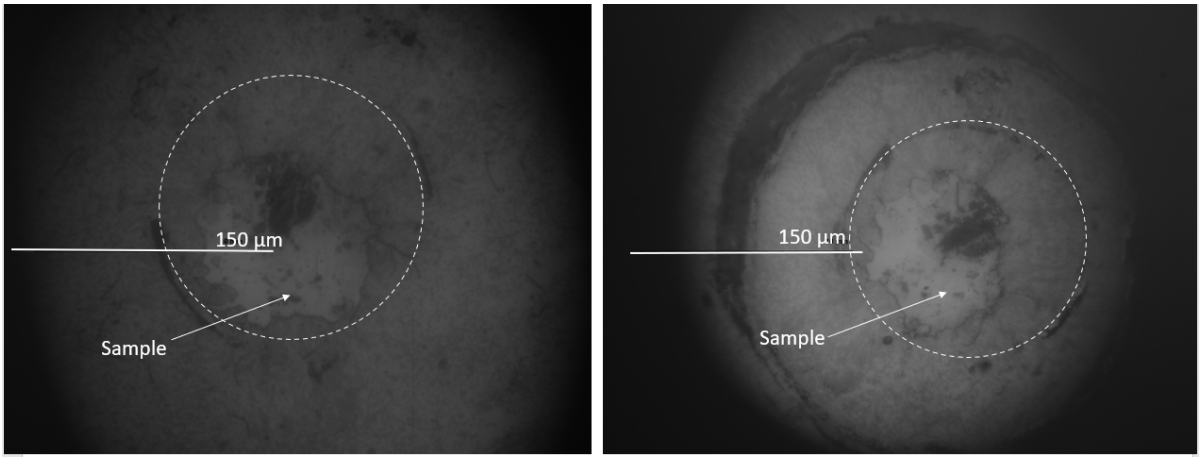

Figure 3.16: Pictures taken by the camera at probe side, showing the diamond deposited with Tin before compression (left) and after decompression (right). The dashed lines show the culet dimensions. The arrows show the Tin-free portion of the sample used for the measurements.

Figure 3.17 shows the signal intensity as a function of pump-probe delay time for increasing pressures acquired in temporal mode and interferometry configuration. Qualitatively we observe the arrival time shifting with pressure towards shorter time, compatible with the combined effect of pressure-induced increasing velocity and decreasing sample thickness. For a better visualization, Figure 3.18 shows only two temporal data corresponding to measurements at ambient pressure and at 8.27 GPa. The overall peaks' shape observed at high pressure changed with respect to measurements at ambient conditions: the signal peaks are broader and less distinguishable because of a noisy background. Moreover, the signal intensity at t_3, corresponding to an acoustic wave generated by a previous laser pulse, unexpectedly results more intense than the one at t_1.

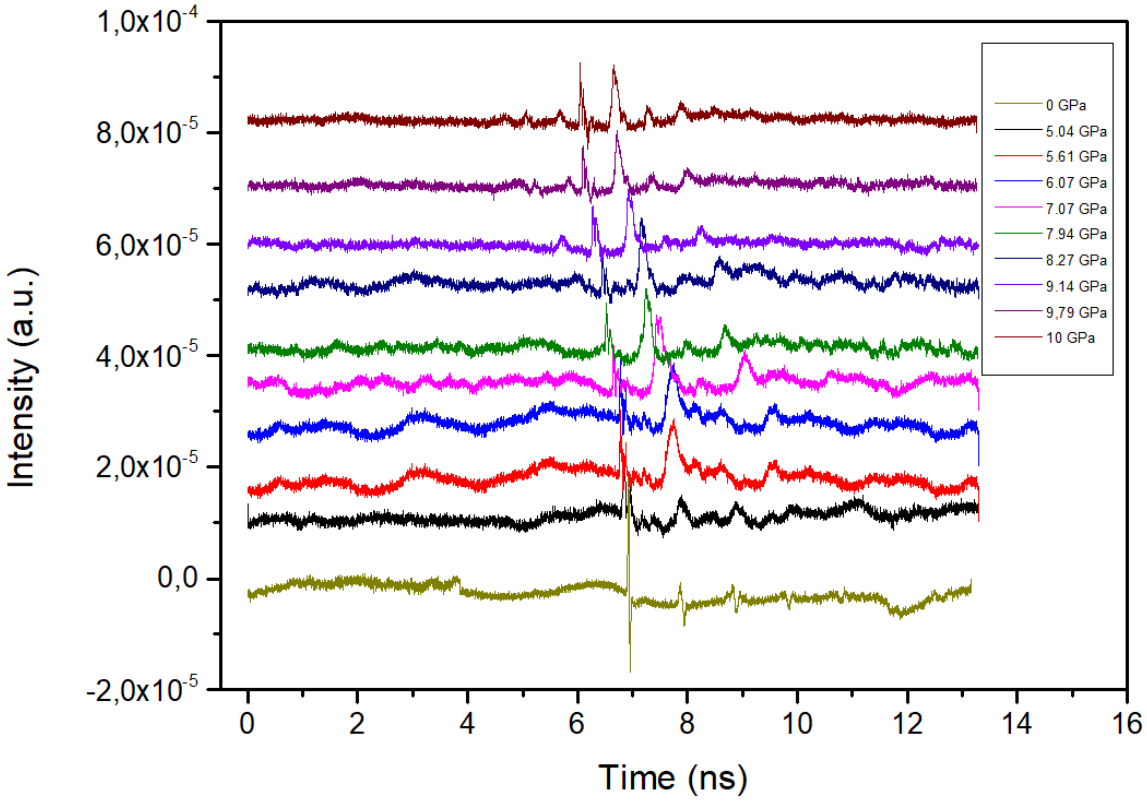

Figure 3.17: Intensity as a function of pump-probe delay time of the small sample (150 μm in diameter and about 50 μm thick) at different applied pressures. These measurements were acquired in temporal mode and interferometry configuration.

As illustrated in the zoomed zone of Figure 3.18, the peaks' shape changed: at ambient pressure the signal peak shows a positive part followed by a negative part; at 8.27 GPa the signal peak is positive and bell-shaped.

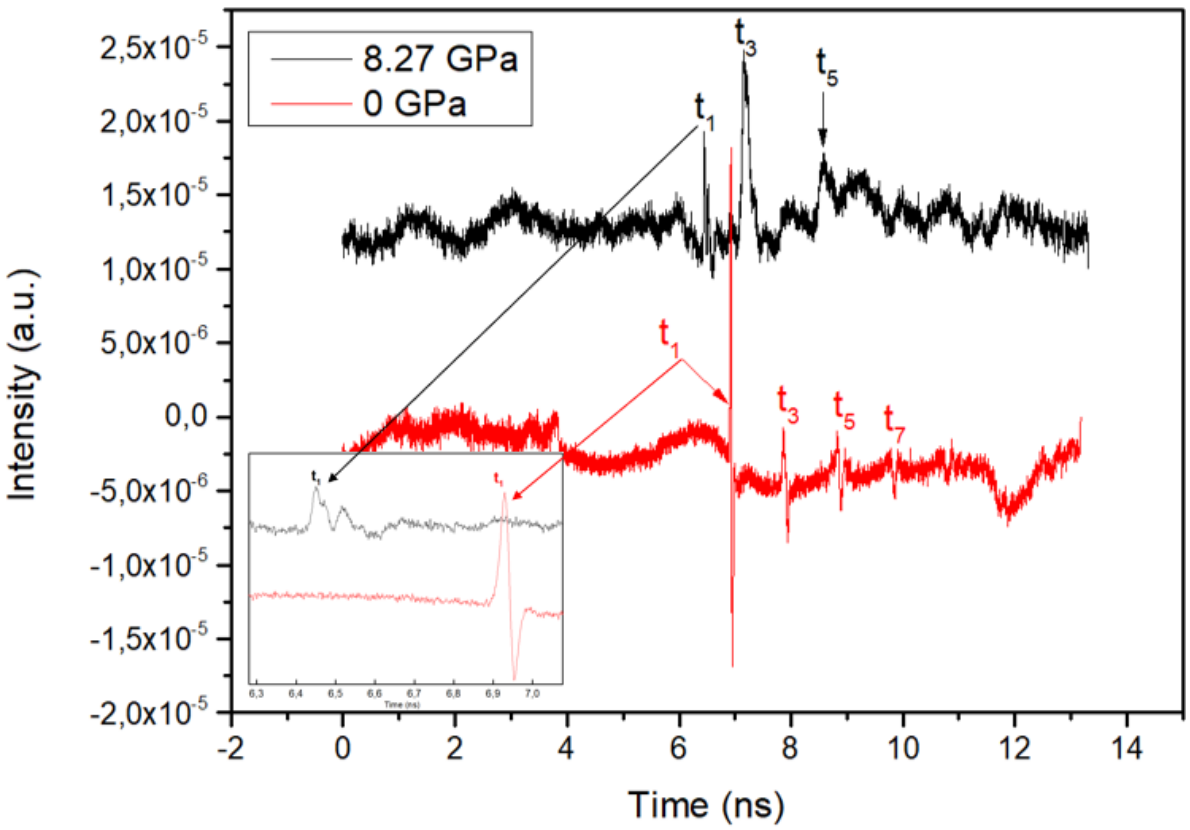

Figure 3.18: Temporal data at ambient pressure and at 8.27 GPa. The t_7 at 8.27 GPa is not well resolved due to the presence of several overlapping oscillations.

The sample thicknesses at the experimental pressures investigated in this work were derived from thickness measured at ambient conditions and making use of Ru's equation of state provided by [24]. Under the assumption of hydrostatic compression, the macroscopic compression of the sample's thickness is proportional to microscopic compression of the hexagonal unit cell along [001] direction, i.e. c axes (see Figure 1.7). Being:

$$\frac{c\,(P)}{c\,(P_0)} = \frac{l\,(P)}{l\,(P_0)} \tag{3.8}$$

where $c(P)$, $c(P_0)$ are provided by [24] and $l(P_0)$ was derived in the last section (small sample). The so obtained thicknesses evaluated at the experimental pressures are listed in Table 3.8.

P (GPa)	c (Å)	l (μm)
0	4.2809	48.01
5.04	4.2603	47.779
5.61	4.2581	47.754
6.07	4.2562	47.733
7.07	4.2523	47.689
7.94	4.2493	47.652
8.27	4.2477	47.638
9.14	4.2444	47.600
9.79	4.2419	47.573
9.99	4.2411	47.564

Table 3.8: Experimental pressures and expected sample's thicknesses derived according to the equation of state provided by [24].

Having estimated the thickness at pressure and having measured the travel times, Δt, from the temporal data, the longitudinal sound velocity in direction [001], $V_{L[001]}$, is derived using Equation 2.10 explicitly expressed for $V_{L[001]}$:

$$V_{L[001]} = \frac{2l}{\Delta t} \quad \text{where} \quad \Delta t = t_3 - t_1$$

Figure 3.19 shows $V_{[001]}$, as a function of pressure. Data collected in DAC, qualitatively show the increase in sound velocity expected with increasing pressure, but absolute values appear inconsistent with sound velocity determination at ambient pressure (P_0), being the $V_{L[001]}$ at P_0 higher than $V_{L[001]}$ at 6 GPa [39]. Possible origins for this anomaly will be discussed later on.

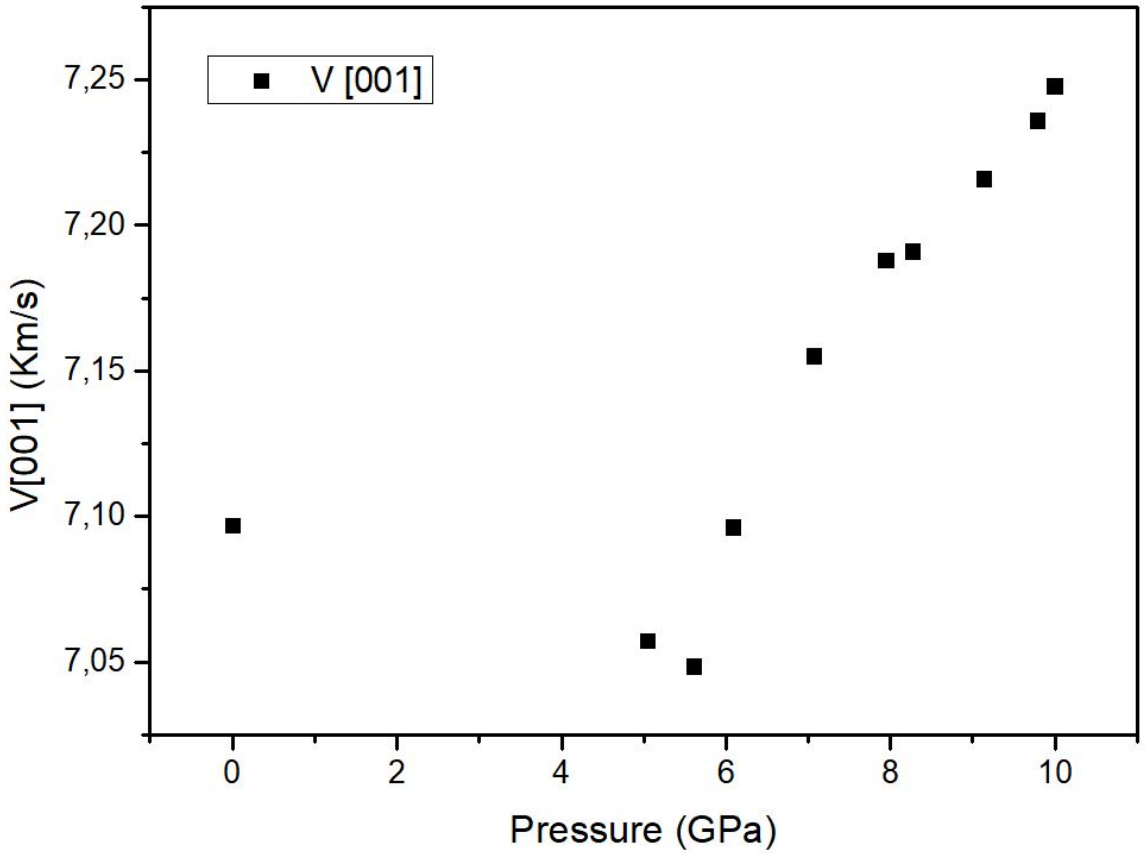

Figure 3.19: Sound velocities of Ru small sample (150 μm in diameter and about 50 μm thick) along direction [001] as a function of pressure.

3.4 Discussion on Ru measurements

3.4.1 Ru at ambient pressure

Ambient pressure measurements on Ru single crystals allowed to collect high quality data. The high-level of surface quality of the produced samples was very important to achieve this. A big Ru sample (2mm x 2mm and $\sim$ 50 μm thick) and a small one (150μm in diameter and $\sim$ 50 thick)- laser-cut out from the big sample- were studied. Laser cutting by femtosecond laser did not degrade crystalline quality and the reduced diameter, compatible with size constraints imposed by use in DAC, did not affect the quality of the results.
In hexagonal symmetry crystals, there are five independent components in the elastic

tensor C_{ij}, and only one direction of propagation is not sufficient to extract all of them. In the present study we considered a Ru single crystal oriented along direction [001] that allows us to extract four out of five independent elastic constants, namely C_{11}, C_{33}, C_{44} and C_{13}, missing C_{12}. The obtained values are in agreement with the values in literature as are the bulk and the shear moduli and compressional and shear velocities calculated from determined C_{ij} according to the Voigt-Reuss-Hill average. The ratio of compressional and shear sound velocities, V_P/V_S is:

$$\frac{V_P}{V_S} = 1.73$$

highlighting that compressional sound velocity propagate faster (with about a double velocity) than the shear sound velocity.
The transverse wave arrival was simulated by the direct program: it was generated by a previous laser pulse with respect to the laser pulse generating the longitudinal wave. Thus, the apparent arrival of the transverse wave before the longitudinal one in the temporal data finds an explanation.
Sample thickness values for both the big and the small samples were derived from temporal data analysis and from imaging data analysis (inversion program), and are summarized in Table 3.9. Both analysis highlighted a slightly difference in the value of thickness of the big and the small samples, revealing a non perfect parallelism of sample's faces. This probably arises from having measured the signal of the big sample in a spot different from the portion from which the small sample was cut out. However, the degree of non-parallelism is very small. The thickness values of the big sample and of the small sample each derived from both temporal data analysis and from imaging data analysis agree within the uncertainties.

	l (μm)
Big sample (temporal analysis)	48.84 $\pm$ 0.02
Big sample (imaging data)	49.2 $\pm$ 0.3
Small sample (temporal analysis)	48.01 $\pm$ 0.02
Small sample (imaging data)	47.9 $\pm$ 0.3

Table 3.9: Big sample and small sample thickness values extracted from temporal data and imaging data analysis.

This serves us to understand that temporal data and imaging data can be independently used for the thickness derivation. In high-quality data -derived from high quality samples surfaces-, the arrival times and the acoustic waves' shapes are clearly distinguishable, allowing to get the elastic constants with precision. Picosecond acoustics measurements can be extended to all the metals, that generally do not necessitate the surface coating.

3.4.2 Ru at high-pressure

High-pressure measurements on Ru single crystal oriented along direction [001] were performed up to 10 GPa. Due to the impossibility to load a noble gas as PTM, a 4:1 methanol-ethanol mixture was used because easy to use and because expected to insure the pressure hydrostaticity up to 10.5 GPa. However, quality of collected data is much poorer than results obtained on silicon single crystal compressed using neon as PTM under similar pressure conditions [40]. Temporal data acquired for Ru at each pressure show a noisy background with many oscillations that make difficult, even though not

impossible, to identify the arrival times. Although, the arrival times decrease with increasing pressure, consistently with volume compressional, the sound velocities, obtained assuming as sample thickness values estimated under the hypothesis of hydrostatic compression and making use of literature equation of state established by X-ray diffraction experiments conducted by [24], show an unexpected decrease from ambient to 5 GPa pressures. Longitudinal sound velocities are expected to increase with density according to the Birch's law [39]. This apparent decrease of the sound velocity could be explained by a path of the acoustic wave longer than the sample thickness. A possibility would be an internal reflection by a crack occurred within the sample when the PTM solidified at 4.5 GPa. A crack in the sample could lead to internal reflections that would be compatible with a longer path of the acoustic wave. Moreover, the noisy background in temporal data appear from 5 GPa, where also the peaks' shape changed. At ambient pressure measurement the signal peak shows a positive and then a negative parts while at high pressure measurements the signal peaks show a positive bell shape. All these observations suggest sample deterioration/alteration. Nonetheless, data have been analyzed. The here-used information in temporal data to derive sound velocity are the arrival times. Changes in peaks' shape and intensity are qualitatively interpreted, but served us only to detect the signal. The hypothesis of the crack within the sample is not sufficient to explain why the peaks' shape changed and why the t_3 is more intense than the t_1 at higher pressures values.
In next set of measurements on Ru single crystal a different PTM will be used, most probably Helium or Neon, which are expected to provide more hydrostatic conditions. Moreover, another Ru single crystal oriented along direction [010] will be investigated to extract the C_{12} elastic component.

Conclusions

This thesis work aimed at establishing an experimental protocol for the determination of the single-crystal elastic constants, C_{ij}, of materials at ambient pressure and at high pressure by picosecond acoustics. In this thesis we considered two test cases: magnesium oxide (MgO) and ruthenium (Ru). The first is an optically transparent insulator, while the second is an opaque metal. Furthermore, MgO is cubic, while Ru is hexagonal. Thus, a protocol working for both cases, assures a good versatility for future applications. Beside these practical aspects, MgO and Ru have been also chosen on the basic of their interest, more or less direct, for Earth and planetary science. In particular, MgO is an end-member mineral composing, planetary mantles and it forms a solid solution with FeO, constituting the second most abundant mineral of the Earth's lower mantle. Ru single crystal is chosen because of its analogy with Iron, Fe. Ru and Fe are isoelectronic, but the heavier Ru is stable in the hcp structure already at ambient conditions, while Fe, which is bcc at ambient conditions, stabilizes the hcp only at high pressures pertinent to the core of the Earth. Then, studying the hcp-Ru single crystal can provide information as well about the hcp-Fe, which, due to the bcc-to-hcp phase transition, is not available as single crystal. In particular, the ratio C_{33}/C_{11} of hcp-iron controlling the seismic anisotropy of the Earth's inner core, can be assessed by studying pressure effects on the C_{33}/C_{11} ratio of hcp-Ru at high pressure.
The following conclusions can be drawn from the work carried out during this thesis:

MgO

- The frequency of the Brillouin oscillations, $\nu = 246.5\ GHz$, was measured in the MgO/Al sample (nominal value of thickness $\sim 100\ \mu m$). From the frequency, the longitudinal sound velocity in direction [001], $V_{L[001]} = (9.06 \pm\ 0.07) km/s$, was derived. The so obtained value agrees within uncertainty with the value $V_{L[001]} = 9.11\ km/s$ calculated from the C_{11} reported in the literature [23].

- The elastic constants of MgO were extracted from measurements on the sample Al/MgO/Al ($\sim 100\ \mu m$ thick) at ambient pressure, obtaining C_{11}= (296.96 $\pm$ 0.19) GPa, C_{44}=(153.6 $\pm$ 0.1) GPa and C_{12}=(98.78 $\pm$ 0.11) GPa. These results agree within uncertainty with the data presented by Sinogeikin in [23]. The obtained compressional and shear waves' velocities, $V_P = (9.692 \pm 0.002)\ km/s$ and $V_S = (5.996 \pm 0.003)\ km/s$, are also compatible with the data in the literature. Finally, the longitudinal sound velocity in direction [001], derived using the determined elastic constant C_{11}, $V_{L[001]} = (9.10 \pm 0.05)\ km/s$, was compared with the same value calculated from the measurements on the Brillouin oscillations, resulting compatible.

  In conclusion, a protocol using picosecond acoustics on transparent sample was successively developed.

Ru

- The elastic properties of ruthenium (50 μm thick) oriented in the [001] direction have been investigated through picosecond acoustics. In crystals with hexagonal symmetry a single direction of propagation is not sufficient to derive all the elastic constants: in particular, by selecting the direction [001] only four out of five independent components can be derived, with the exception of the C_{12}. The obtained elastic constants are: $C_{11} = (564 \pm 6)\ GPa$, $C_{33} = (626 \pm 8)\ GPa$, $C_{44} = (182.2 \pm 0.5)\ GPa$ and $C_{13} = (175 \pm 7)\ GPa$. They are in agreement within uncertainty with the data present in the literature [29]. The bulk and shear moduli were derived assuming the C_{12} to be the same as the value provided by the literature. From these, the compressional and shear velocities were derived according the Voigt-Reuss-Hill average, obtaining: $V_P = (6.78 \pm 0.02)\ km/s$ and $V_S = (3.93 \pm 0.01)\ km/s$.

- The elastic constants extracted from measurements on big and small samples yield compatible results. This suggest that any significant alteration on the sample (crystallinity, defects, remelting) were induced by laser cutting. Thus, as shown for Ru, picosecond acoustic measurements can be performed on samples available in small quantities or with dimensions compatible with DACs.

- For the first time, high-pressure measurements (up to 10 GPa) were carried out on ruthenium single crystal through picosecond acoustics combined with DAC technology for high pressure generation. Due to impossibility in using the gas loading system at the time of the measurements, we resorted to a 4:1 liquid mixture of methanol-ethanol, as pressure transmitting medium, less hydrostatic than a noble gas. Although it was possible to measure an acoustic signal in both temporal and imaging modes and interferometry configuration, confirming the success of the picosecond acoustics in combination with the DAC, the acquired data showed inconsistencies with what expected. In fact, the experimental sound velocity, which should increase with pressure, are observed to apparently decrease, although marginally, from ambient pressure to 5 GPa and increase only upon further compression. This behavior is compatible with a longer path of the acoustic waves on the sample at 5 GPa with respect to ambient conditions, which however would contrast with the volume compression that occurs at increasing pressures. Chemical reactions between samples and PTM were not observed on the recovered sample, thus excluding chemical sample's alteration as a cause. A possible hypothesis may be the scattering of the acoustic wave by presence of an internal crack within the sample occurred upon compression between 0 GPa and 5 GPa. Probably the selected PTM produced a uni-axial pressure while solidifying at 4.5 GPa, which caused the sample to crack.

In the next set of measurements, MgO will be studied at high pressure and so it will be necessary to reduce its thickness from 100 μm to 40 μm to suit the constraints imposed by experimentation in DAC. Ruthenium will be investigated again in a new set of measurements using a sample oriented along the [010] direction which allows to extract also the C_{12}, in order to derive the complete elastic tensor at ambient pressure. For high-pressure measurements a noble gas, Neon or Argon, will be used as pressure transmitting medium.

The most general conclusion that can be drawn from this thesis work concerns the success of the picosecond acoustics measurements and the data analysis based on inversion program - which allows extracting the elastic constants from the sound velocities - in determining the elastic constants of materials. Picosecond acoustics confirms to be an

experimental technique of great interest and potentiality, thanks to its versatility in the choice of materials, and thanks to the possibility it offers to conduct laboratory-based experiments, which allow much more flexibility that synchrotron based techniques, in particular in term of reproducing experiments and performing studies with a systematic character. As we outlined in Chapter 1, all currently-used experimental techniques for studying elastic properties show limitations, which we can be overcome by picosecond acoustics.

While not directly part of this thesis work, an upgrade of the set-up to implement a laser heating system is currently ongoing. This will allow experiments to be conducted at combined high pressure and high temperature conditions, over a P-T range larger than what achieved so far [41]. Picosecond acoustics show all the potentialities to become at term a reference laboratory-based technique, able to measure the sound velocities of materials at extreme conditions. In particular, it will allow probing sound wave propagation at the actual conditions of pressure and temperature existing inside the planets, providing direct guidance to interpretation of seismological observations and allowing to built reliable composition and structural models inverted from observations.

Appendix A

Acoustic phonons

A.0.1 One-dimensional chain of ions: the simplest discussion about phonons

The mathematical treatment here presented is the one followed by [42]. Let's consider a one dimensional chain of ions of mass M sitting at equilibrium distances a connected by springs of constant $\mathcal{K}$ (see figure A.1). There are N ions and the total length of the chain is L= Na. Let us make the assumption that each ion interacts only with its nearest neighbors.

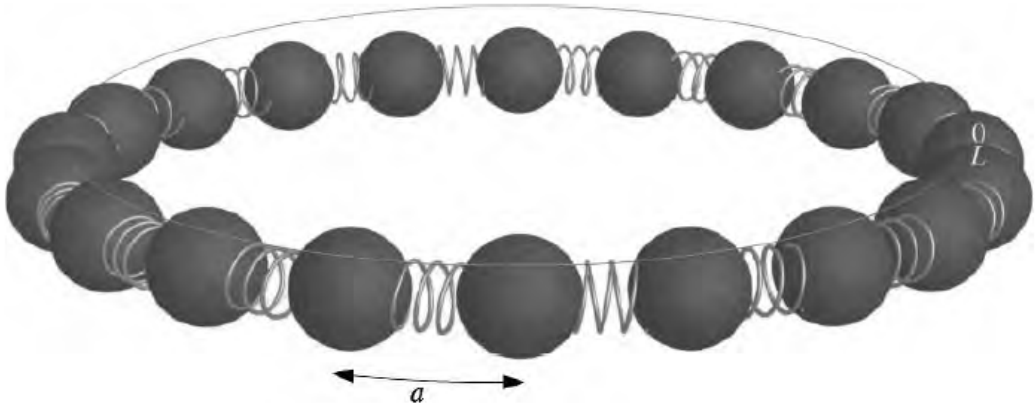

Figure A.1: One dimensional chain of N ions connected by springs: the simplest discussion of phonons[42].

Denoted by u_l the deviation of ion l $\in$ [0,.., N-1] from its equilibrium position, with periodic boundary condition implying that $u_N = u_0$ then

$$M\ddot{u}^l = \mathcal{K}\left(u^{l+1} - u^l\right) + \mathcal{K}\left(u^{l-1} - u^l\right) \tag{A.1}$$

A solution of this equation is given by plan waves:

$$u^l = \epsilon e^{ikla - i\omega t} \tag{A.2}$$

The periodic condition implies:

$$kNa = 2\pi n \Rightarrow k = 2\pi n/(Na), n \in [0 \dots N-1] \tag{A.3}$$

Substituting equation A.2 in equation A.1, we obtain:

$$\begin{aligned} -M\omega^2 \epsilon e^{ikla - i\omega t} &= \left[\mathcal{K}\left(e^{ika} - 1\right) + \mathcal{K}\left(e^{-ika} - 1\right)\right] \epsilon e^{ikla - i\omega t} \\ \Rightarrow -M\omega^2 = \mathcal{K}(2\cos(ika) - 2) &\Rightarrow \omega = 2\sqrt{\frac{\mathcal{K}}{M}} |\sin(\|a/2)| \end{aligned} \tag{A.4}$$

and simplifying with respect to ω:

$$\omega = 2\sqrt{\frac{\mathcal{K}}{M}}|sin(ka/2)| \tag{A.5}$$

A.0.2 One-dimensional chain with basis

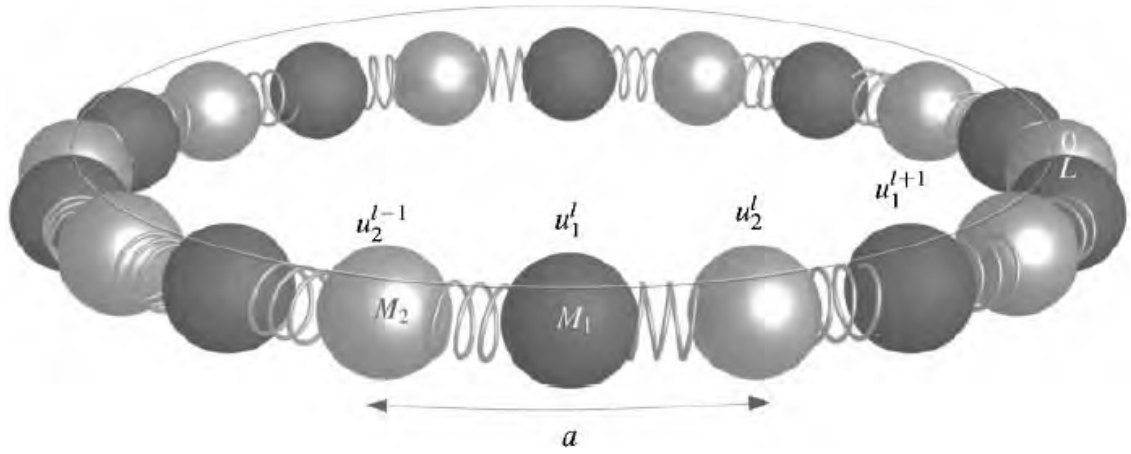

Figure A.2: One-dimensional chain of ions of two different species placed alternatively [42].

Next level of complexity is the case of one-dimensional chain of ions with basis.
Consider again a one-dimensional chain of ions, but this time with two different types of ions having mass M_1 and M_2. They are placed alternatively in the one-dimensional chain (see figure A.2).
Let us assume that each ion interacts just with its nearest neighbors. By performing similar reasoning as done in the precedent section, we impose:

$$\begin{aligned} M_1\ddot{u}_1' &= \mathcal{K}\left(u_2^l - 2u_1^l + u_2^{l-1}\right) \\ M_2\ddot{u}_2^l &= \mathcal{K}\left(u_1^{l+1} - 2u_2^l + u_1^l\right) \end{aligned} \tag{A.6}$$

By assuming a solution in the form:

$$u_j^l = \epsilon_j e^{ikla-\omega t} \tag{A.7}$$

and substituting it in A.6, we obtain:

$$\begin{aligned} \Rightarrow -\omega^2 M_1\epsilon_1 e^{ikla} &= \mathcal{K}\left(\epsilon_2 - 2\epsilon_1 + \epsilon_2 e^{-ika}\right)e^{ikla} \\ -\omega^2 M_2\epsilon_2 e^{ikla} &= \mathcal{K}\left(\epsilon_1 e^{ika} - 2\epsilon_2 + \epsilon_1\right)e^{ikla} \end{aligned} \tag{A.8}$$

That solved with respect to ω, becomes:

$$\Rightarrow \omega = \sqrt{\mathcal{K}}\sqrt{\frac{M_1 + M_2 \pm \sqrt{M_1^2 + 2M_1M_2\cos ka + M_2^2}}{M_1M_2}} \tag{A.9}$$

The two solutions of eq. A.9 correspond to two branches of phonon dispersion relation: optical branch and acoustic branch (see fig.A.3). The latter vanishes linearly near k=0 with a slope proportional to sound velocity.
For small k the two branches, the acoustic branch and the optical one (respectively the top equation and the bottom equation in the following equation) take the form:

$$\begin{aligned} \omega(k) &= \sqrt{\frac{\mathcal{K}}{2(M_1+M_2)}}ka, \quad \epsilon_1 = 1; \epsilon_2 = 1 + ika/2 \\ \omega(k) &= \sqrt{\frac{2\mathcal{K}(M_1+M_2)}{M_1M_2}}, \quad \epsilon_1 = M_2; \epsilon_2 = -M_1(1 + ika/2) \end{aligned} \tag{A.10}$$

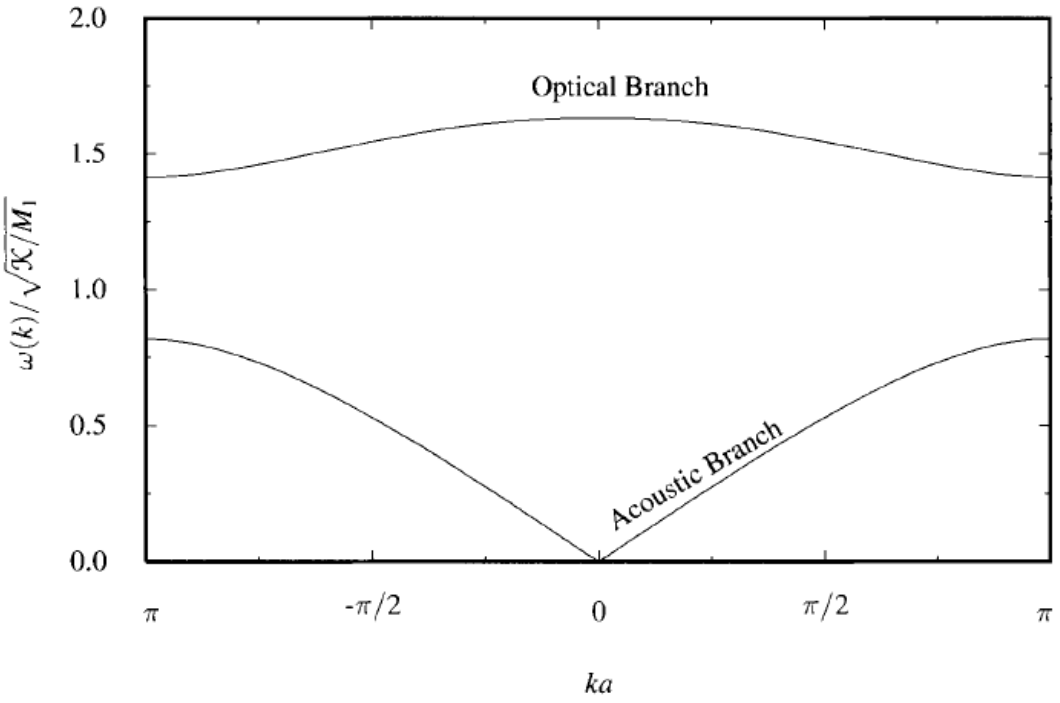

Figure A.3: Phonon dispersion relation for one dimensional chain composed by two types of ions with mass M_1 and M_2 positioned alternate in the chain. [42].

In conclusion, by interpreting the results expressed in A.10, for the acoustic mode, atoms within the unit cell move essentially in unison, while for the optical mode, atoms within the unit cell vibrate out of phase (represented in fig.A.4).

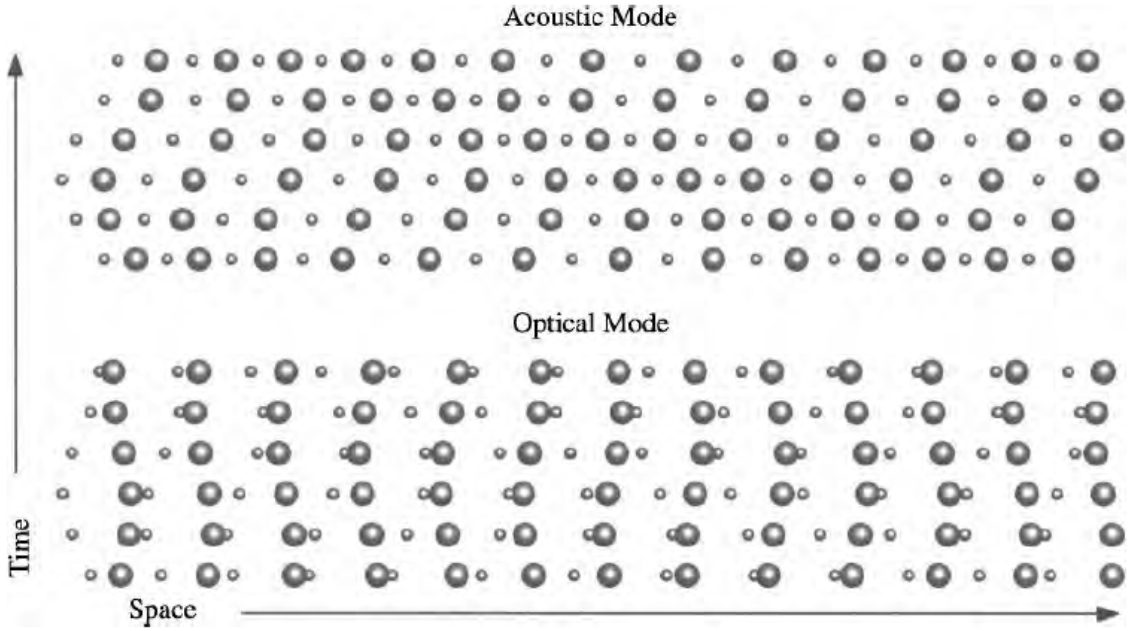

Figure A.4: Acoustic phonons vibrate in unison inside the unit cell while optical phonons vibrate out of phase [42].

Appendix B

Mathematical derivation of Christoffel equation

The mathematical treatment here presented has been taken from [8]. Assuming that a perturbation has been applied to a solid, so that it results to be locally in movement. Each displacement u_i of each point of the solid described by coordinates x_k is time-dependent, so we can write $u_i = u_i(x_k, t)$. By considering the fundamental equation of dynamics we can write:

$$\rho \frac{\partial^2 u_i}{\partial t^2} = \frac{\partial \sigma_{ij}}{\partial x_j} \tag{B.1}$$

By taking into account Hooke's law:

$$\rho \frac{\partial^2 u_i}{\partial t^2} = C_{ijkl} \frac{\partial^2 u_l}{\partial x_j \partial x_k} \tag{B.2}$$

This is a system of three second order differential equations in three dimensions. Eq. B.2 is in the same form as the d'Alembert waves' equation for propagating waves:

$$\rho \frac{\partial^2 u}{\partial t^2} = \frac{1}{\chi} \frac{\partial^2 u}{\partial x^2} \tag{B.3}$$

whose general solution is in the form:

$$u = F(t - x/V), \quad \text{with} \quad V^2 = 1/\rho\chi \tag{B.4}$$

Thus, similar conclusions can be deduced for eq. B.2, in fact we look for a solution with the form of a travelling plane wave propagating within the solid along a defined direction indicated by a unitary vector $\overrightarrow{n}$=(n_1, n_2, n_3) perpendicular to wave's plane which satisfies:

$$u_i = u_i^{\mathsf{T}} F\left(t - \frac{\overrightarrow{n}\,\overrightarrow{x}}{V}\right) = u_i^{\mathsf{T}} F\left(t - \frac{n_j x_j}{V}\right) \tag{B.5}$$

In order to determine the phase velocity V and the wave polarization u_i^{T}, that is the direction of particles displacement, we can substitute in eq. B.2 the result expressed in B.5. Substituting the second-order derivative of F, F'', and the first-order derivative F' in eq. B.2, we obtain:

$$\frac{\partial^2 u_i}{\partial t^2} = u_i^{\mathsf{T}} F'' \quad \text{and} \quad \frac{\partial u_l}{\partial x_j} = -u_l^{\mathsf{T}} \frac{n_j}{V} F' \tag{B.6}$$

from which:

$$\frac{\partial^2 u_l}{\partial x_j \partial x_k} = u_l^{\mathsf{T}} \frac{n_j n_k}{V^2} F'' \tag{B.7}$$

Thus,

$$\rho u_i^T F'' = C_{ijkl} n_j n_k u_l^{\mathsf{T}} \frac{F''}{V^2} \tag{B.8}$$

which, in the end, leads to:

$$\rho V^2 u_i^{\mathsf{T}} = C_{ijkl} n_j n_k u_l^{\mathsf{T}} \tag{B.9}$$

This last equation is called Christoffel equation and provides a relation between the phase velocity, V, of a wave with elastic constants of the material. We can introduce a tensor $\Gamma_{il} = C_{ijkl} n_j n_k$, the Christoffel tensor (second-order rank tensor), and rewrite eq. B.9 in terms of this new tensor, obtaining:

$$\Gamma_{il} u_l^{\mathsf{T}} = \rho V^2 u_i^{\mathsf{T}} \tag{B.10}$$

This equation shows that polarization vector $\vec{u}^{\mathsf{T}}$ is an eigenvector of Γ_{il} with eigenvalue $\gamma = \rho V^2$. So phase velocity, V, and polarization of plane waves propagating along a direction $\overrightarrow{n}$ within a crystal with stiffness tensor C_{ijkl}, are respectively eigenvalues and eigenvectors of Christoffel tensor. In general, for a given direction of propagation, phase velocities are roots of this secular problem:

$$\left| \Gamma_{il} - \rho V^2 \delta_{il} \right| = 0 \tag{B.11}$$

The theoretical treatment presented above is valid for plane waves but since any spherical wave can be seen as composition of plane waves (through Weyl integral) analogous solutions can be derived in the case of spherical waves [43].

Appendix C

Hexagonal closed-packed phase

Close-packed structures often occurs in practice because they are natural forms for monoatomic crystals, under the assumption of hard spheres atoms. Hexagonal close-packed (hcp) is the one which optimizes better the space. A visualization of how hcp is produced can be done starting from a plane of identical atoms that can be arranged in a hexagonal fashion. There are two ways of stacking such layers of spheres. Taking the first layer to have spheres centred at point A, the second layer has centre at points B, above the interstices of the first layer. For the third layer there are two choices: the centres can be above points C or A (see figure C.1). In the first case the centres have a sequence ABC in each period, giving the FCC face-centred cubic. The second case has layers with centres ABAB, giving the hexagonal close-packed (hcp) [8].

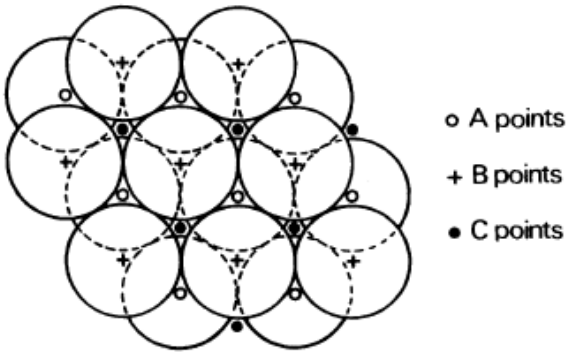

Figure C.1: Under the assumption of atoms as hard spheres: first layer of atoms placed in hexagonal fashion centred in A, the second layer of atoms can be placed in a way to have the centres of the spheres on the interstices (point B), to create hcp structure the third layersì should have the atoms centres at the first layer atoms' centres, i.e. point A.

Appendix D

Change in sample's reflectivity due to acoustic waves

The mathematical treatment reported below is the one proposed in [44]. An acoustic or thermal gradient induces at any point in the sample a gradient in the dielectric constant.

$$\epsilon(z,t) = \epsilon + \Delta\epsilon(z,t) = [n + \Delta n(z,t)]^2 \tag{D.1}$$

where $\Delta n(z,t) = \frac{\partial n}{\partial X} X(z,t)$. X represents the temperature or the strain, n is the complex refraction index of the medium and $\frac{\partial n}{\partial X}$ is a complex thermo-optical or acousto-optical constant. Solving the equation of the electromagnetic field E:

$$\frac{\partial^2 E}{\partial z^2} = [\epsilon + \Delta\epsilon(z,t)]\frac{\partial^2 E}{\partial t^2} \tag{D.2}$$

we obtain:

$$E_t = t_{01} \int d\Omega E_i(\Omega) e^{i(\Omega t - n k_0 z)} \tag{D.3}$$

where there is no gradient, Ω is the angular frequency of the electromagnetic field, k_0 the wave vector in vacuum and $t_{01} = \frac{2}{1+n}$ is the transmission coefficient of the air-sampple interface. Considering that the light frequency is much greater than the spectrum of $\Delta\epsilon(z,t)$ the equation for propagation can be solved for a Fourier component of the electromagnetic field, this allows to treat the perturbation induced by the gradient as quasi-static. At the beginning we can assume the thickness of the material as infinitesimal dz, with a refractive index n modified by an amount of Δn at a distance z from the surface.

$$\begin{pmatrix} a_0 \\ b_0 \end{pmatrix} = \frac{1}{t_{01}t_{12}t_{21}} \begin{pmatrix} 1 & r_{01} \\ r_{01} & 1 \end{pmatrix} \begin{pmatrix} e^{-ink_0 z} & 0 \\ 0 & e^{ink_0 z} \end{pmatrix} \begin{pmatrix} 1 & r_{12} \\ r_{12} & 1 \end{pmatrix} \begin{pmatrix} e^{-i(n+\Delta n)k_0 dz} & 0 \\ 0 & e^{i(n+\Delta n)k_0 dz} \end{pmatrix} \begin{pmatrix} 1 & r_{21} \\ r_{21} & 1 \end{pmatrix} \begin{pmatrix} a_s \\ 0 \end{pmatrix}$$

(D.4)

where

$$r_{01} = \frac{1}{1+n}, r_{21} = \frac{\Delta n}{2n + \Delta n}, \Delta n = \frac{\Delta\epsilon}{2n}$$

Then, by expanding in powers of Δn and dz, we can infer the r(z,t):

$$r(z,t) = \frac{b0}{a_0} = r_{01} + ik_0(1 - r_{01}^2)e^{2ik_0 nz}\Delta n(z,t)dz \tag{D.5}$$

and

$$\frac{\Delta r}{r} = \frac{r(z,t) - r_{01}}{r_{01}} = ik_0 \frac{1 - r_{01}^2}{r_{01}} e^{2ik_0 nz}\Delta n(z,t)dz \tag{D.6}$$

We have to integrate over the overall sample thickness in order to obtain the total contribution of the gradient to the change of reflectance:

$$\frac{\Delta r(t)}{r}|_{gradient} = ik_0 \frac{\partial n}{\partial X} \frac{4n}{1-n^2} \int_0^{+\infty} dz X(z,t) e^{2ik_0 nz} \tag{D.7}$$

Also the surface displacement, u_0 plays a role, affecting the imaginary part of $\frac{\Delta r}{r}$

$$\frac{\Delta r}{r}|_{geom} = 2ik_0 u_0(t)$$

Summing up, the total from acoustic and thermal effects is described by the equation below:

$$\frac{\Delta r(t)}{r} = \mathrm{i}k_0 \left\{ 2u_0(t) + \frac{4n}{1-n^2} \int_0^{+\infty} \mathrm{d}z \left[\frac{\partial n}{\partial T} \Delta T(z,t) + \frac{\partial n}{\partial \eta} \Delta \eta(z,t) \right] e^{2ik_0 nz} \right\} \tag{D.8}$$

It is possible to see that the change of reflectivity may be caused by different contributions: first due to the surface displacement caused by the acoustic wave's propagation. Second contribution corresponds to the temperature increase caused by pump. Third term is due by the influence that a deformation η can have on the optic properties of a material, described by its photo-elastic coupling coefficient $\frac{\partial n}{\partial z}$[31].

Bibliography

[1] Lajos Volgyesi and M Moser. "THE INNER STRUCTURE OF THE EARTH". In: *Periodica Polytechnica Chemical Engineering* 26 (Jan. 1982).

[2] Adam M Dziewonski and Don L Anderson. "Preliminary reference Earth model". In: *Physics of the earth and planetary interiors* 25.4 (1981), pp. 297–356.

[3] Yosio Nakamura, Gary V Latham, and H James Dorman. "Apollo lunar seismic experiment—Final summary". In: *Journal of Geophysical Research: Solid Earth* 87.S01 (1982), A117–A123.

[4] Domenico Giardini et al. "The seismicity of Mars". In: *Nature Geoscience* 13.3 (2020), pp. 205–212.

[5] Philippe Lognonné et al. "Constraints on the shallow elastic and anelastic structure of Mars from InSight seismic data". In: *Nature Geoscience* 13.3 (2020), pp. 213–220.

[6] Francis Birch. "Elasticity and constitution of the Earth's interior". In: *Journal of Geophysical Research* 57.2 (1952), pp. 227–286.

[7] Daniele Antonangeli et al. "Composition of the Earth's inner core from high-pressure sound velocity measurements in Fe–Ni–Si alloys". In: *Earth and Planetary Science Letters* 295.1-2 (2010), pp. 292–296.

[8] Eugène Dieulesaint and Daniel Royer. *Ondes élastiques dans les solides-Tome 1: Propagation libre et guidée*. 1996.

[9] Thomas S Duffy. "Single-crystal elastic properties of minerals and related materials with cubic symmetry". In: *American Mineralogist: Journal of Earth and Planetary Materials* 103.6 (2018), pp. 977–988.

[10] J Peter Watt, Geoffrey F Davies, and Richard J O'Connell. "The elastic properties of composite materials". In: *Reviews of Geophysics* 14.4 (1976), pp. 541–563.

[11] Daniele Antonangeli. "Elasticity and sound wave anisotropy of hcp-metals at high-pressure". 2005PA066001. PhD thesis. 2005, 134 p. URL: `http://www.theses.fr/2005PA066001`.

[12] Baosheng Li and Robert C Liebermann. "Study of the Earth's interior using measurements of sound velocities in minerals by ultrasonic interferometry". In: *Physics of the Earth and Planetary Interiors* 233 (2014), pp. 135–153.

[13] Sergio Speziale, Hauke Marquardt, and Thomas S Duffy. "Brillouin scattering and its application in geosciences". In: *Reviews in Mineralogy and Geochemistry* 78.1 (2014), pp. 543–603.

[14] Neil W Ashcroft, N David Mermin, et al. *Solid state physics [by] Neil W. Ashcroft [and] N. David Mermin*. 1976.

[15] S Klotz and M Braden. "Phonon dispersion of bcc iron to 10 GPa". In: *Physical review letters* 85.15 (2000), p. 3209.

[16] Daniele Antonangeli et al. “Phonon triggered rhombohedral lattice distortion in vanadium at high pressure”. In: *Scientific reports* 6.1 (2016), pp. 1–5.

[17] AI Chumakov and W Sturhahn. “Experimental aspects of inelastic nuclear resonance scattering”. In: *Hyperfine interactions* 123.1-4 (1999), pp. 781–808.

[18] Jung-Fu Lin et al. “Nuclear resonant inelastic X-ray scattering and synchrotron Mössbauer spectroscopy with laser-heated diamond anvil cells”. In: *Advances in High-Pressure Technology for Geophysical Applications*. Elsevier, 2005, pp. 397–411.

[19] Chang-Sheng Zha, Ho-kwang Mao, and Russell J Hemley. “Elasticity of MgO and a primary pressure scale to 55 GPa”. In: *Proceedings of the National Academy of Sciences* 97.25 (2000), pp. 13494–13499.

[20] BB Karki et al. “Structure and elasticity of MgO at high pressure”. In: *American Mineralogist* 82.1-2 (1997), pp. 51–60.

[21] Jeffrey G Smith et al. “Intrinsic conductivity in magnesium–oxygen battery discharge products: MgO and MgO2”. In: *Chemistry of Materials* 29.7 (2017), pp. 3152–3163.

[22] *MgO structure*. `http://chemwiki.ucidavis.edu/Wikitexts/Howards_University`. Accessed: 2020-12-06.

[23] Stanislav V Sinogeikin et al. “Compact high-temperature cell for Brillouin scattering measurements”. In: *Review of Scientific Instruments* 71.1 (2000), pp. 201–206.

[24] Simone Anzellini et al. “Thermal equation of state of ruthenium characterized by resistively heated diamond anvil cell”. In: *Scientific reports* 9.1 (2019), pp. 1–11.

[25] Simone Anzellini. “Phase diagram of iron under extreme conditions measured with time-resolved methods”. PhD thesis. Sorbonne Université, 2014.

[26] Daniele Antonangeli and Eiji Ohtani. “Sound velocity of hcp-Fe at high pressure: experimental constraints, extrapolations and comparison with seismic models”. In: *Progress in Earth and Planetary Science* 2.1 (2015), p. 3.

[27] Zhisheng Zhao et al. “Carbon coated face-centered cubic Ru–C nanoalloys”. In: *Nanoscale* 6.17 (2014), pp. 10370–10376.

[28] Dornelf. *Hexagonal close packed crystal structure*. July 2012. URL: `https://fr.wikipedia.org/wiki/Fichier:Hexagonal_close_packed.svg#filelinks`.

[29] Desmond Tromans. “Elastic anisotropy of hcp metal crystals and polycrystals”. In: *arpa press* 9.1 (2011), pp. 462–483.

[30] Thomas Dehoux. “Géenération et détection par couplage élasto-optique tridimensionnel de champs acoustiques picosecondes diffractés”. PhD thesis. Université Bordeaux 1, 2007.

[31] Thibaut Deletang. *Mesures de vitesse du son dans des minéraux opaques : vers des mesures en conditions du manteaux Martien*. 2019.

[32] Ho-Kwang Mao et al. “Solids, liquids, and gases under high pressure”. In: *Reviews of Modern Physics* 90.1 (2018), p. 015007.

[33] Agnes Dewaele, Paul Loubeyre, and Mohamed Mezouar. “Equations of state of six metals above 94 GPa”. In: *Physical Review B* 70.9 (2004), p. 094112.

[34] S Klotz et al. “Hydrostatic limits of 11 pressure transmitting media”. In: *Journal of Physics D: Applied Physics* 42.7 (2009), p. 075413.

[35] F Decremps et al. “Sound velocity of iron up to 152 GPa by picosecond acoustics in diamond anvil cell”. In: *Geophysical Research Letters* 41.5 (2014), pp. 1459–1464.

[36] F Decremps et al. “Equation of state, stability, anisotropy and nonlinear elasticity of diamond-cubic (ZB) silicon by phonon imaging at high pressure”. In: *Physical Review B* 82.10 (2010), p. 104119.

[37] Vitalyi E Gusev and Pascal Ruello. “Advances in applications of time-domain Brillouin scattering for nanoscale imaging”. In: *Applied Physics Reviews* 5.3 (2018), p. 031101.

[38] Thomas S Duffy and Thomas J Ahrens. “Sound velocities at high pressure and temperature and their geophysical implications”. In: *Journal of Geophysical Research: Solid Earth* 97.B4 (1992), pp. 4503–4520.

[39] Francis Birch. “The velocity of compressional waves in rocks to 10 kilobars: 1.” In: *Journal of Geophysical Research* 65.4 (1960), pp. 1083–1102.

[40] Eric Edmund et al. “Picosecond Acoustics Technique to Measure the Sound Velocities of Fe-Si Alloys and Si Single-Crystals at High Pressure”. In: *Minerals* 10.3 (2020), p. 214.

[41] Simon Ayrinhac et al. “High-pressure transformations in liquid rubidium”. In: *Physical Review Materials* 4.11 (2020), p. 113611.

[42] Michael P Marder. *Condensed matter physics*. John Wiley & Sons, 2010.

[43] Brokešová Johana. *Propagation of seismic waves- theoretical background*. University Lecture. 2015.

[44] Bernard Perrin. “Investigation of Short-Time Heat Transfer Effects by an Optical Pump–Probe Method”. In: *Microscale and nanoscale heat transfer*. Springer, 2007, pp. 333–359.